Ultrafast spectroscopy of 2D hybrid perovskites

Katia Abdel Baki

▶ **To cite this version:**

HAL Id: tel-01275473
https://tel.archives-ouvertes.fr/tel-01275473

THESE DE DOCTORAT

DE L'ECOLE NORMALE SUPERIEURE DE CACHAN

Présentée par

Katia ABDEL BAKI

Pour obtenir le grade de

DOCTEUR DE L'ECOLE NORMALE SUPERIEURE DE CACHAN

Domaine :

SCIENCES PHYSIQUES

Sujet de la thèse :

Spectroscopie Ultrarapide des 2D pérovskites hybrides

Thèse présentée et soutenue soutenue à Cachan le 05 Decembre 2014,

devant le jury composé de :

Jacky EVEN	Professeur des universités	Président du jury
Pierre GILLIOT	Directeur de recherche (CNRS)	Rapporteur
Catherine SCHWOB	Professeur des universités	Rapporteur
Joël LEYMARIE	Professeur des universités	Examinateur
Emmanuelle DELEPORTE	Professeur des universités	Directeur de thèse
Jean-Sébastien LAURET	Professeur des universités	Encadrant

Laboratoire Aimé Cotton

ENS Cachan/ CNRS/UMR9188

Rue du Belvédère, 91400 ORSAY CEDEX (France)

DOCTORAL THESIS

OF ECOLE NORMALE SUPERIEURE DE CACHAN

Defended by

Katia ABDEL BAKI

To obtain the title of

PhD of ECOLE NORMALE SUPERIEURE DE CACHAN

Domain:

PHYSICS

Thesis title:

Ultrafast Spectroscopy of 2D hybrid perovskites

Thesis defended at Cachan on 05 December 2014,

Jury :

Jacky EVEN	Professor (INSA de Rennes)	President of the jury
Pierre GILLIOT	Research director (Strasbourg)	Referee
Catherine SCHWOB	Professor (UPMC)	Referee
Joël LEYMARIE	Professor(Universite Clermont)	Member
Emmanuelle DELEPORTE	Professor (ENS Cachan)	Director
Jean-Sébastien LAURET	Professor (ENS Cachan)	Supervisor

Laboratoire Aimé Cotton

ENS Cachan/ CNRS/UMR9188

Rue du Belvédère, 91400 ORSAY CEDEX (France)

This thesis is dedicated to

The memory of my grandpa

The most compassionate mother in the world, my mother

My beloved father, brother and sisters

My angle, My soul mate, my love, نور عيوني , Hassan

Abstract

Organic-inorganic hybrid semiconductors based on metal halide units have attracted attention due to their potential applications in light-emitting optical devices and more recently in photovoltaic devices. The exciton binding energies and oscillator strengths are sufficiently large in these systems making the realization of microcavities in the strong coupling regime with high quality at room temperature possible. As a relatively new material, the perovskites still have many behaviors that are not well understood and a lot of research work is necessary. The research in this manuscript is divided into two parts: In the first part, we study the dynamics of excitons in a particular perovskite (PEPI) at room temperature using pump-probe spectroscopy for low and high excitation regime. At high excitation density, a process of Auger recombination of excitons comes into play. An ultrafast intraband relaxation has been observed. The second part of the manuscript is dedicated to the study the optical properties of high quality PEPI-based microcavity at room temperature using microphotoluminescence spectroscopy. A new perovskite material with better photostability has also been synthesized.

Résumé

Les pérovskites hybrides organiques-inorganiques ont attiré l'attention en raison de leurs applications potentielles dans des dispositifs optiques et plus récemment dans les dispositifs photovoltaïques. L'arrangement cristallin des pérovskites forme une structure en multi-puits quantiques dans laquelle les états excitoniques présentent une grande force d'oscillateur et une énergie de liaison importante, ce qui rend la réalisation de microcavités dans le régime de couplage fort avec une haute qualité possible à la température ambiante. Comme un matériau relativement nouveau, les pérovskites ont encore beaucoup de comportements qui ne sont pas bien compris et beaucoup de travail de recherche est nécessaire. La recherche dans ce manuscrit est divisé en deux parties: Dans la première partie, nous étudions la dynamique des excitons sur une pérovskite particulière (PEPI), à température ambiante par mesure pompe-sonde sous faible et fort régime d'excitation. Sous forte densité d'excitation, d'un processus de recombinaison Auger des excitons est présenter. Relaxation intrabande ultra-rapide a été observée. La deuxième partie du manuscrit est consacrée à l'étude des propriétés optiques à microcavité PEPI à haut qualité à température ambiante par spectroscopie microPL. Des

nouvelles pérovskites avec des propriétés optimisées (propriétés optiques d'émission, rugosité de surface et photostability) ont également été synthétisé.

<u>*Acknowledgment*</u>

"When we dream alone it is only a dream, but when many dream together it is the beginning of a new reality"

Friedensreich Hundertwasser

On the occasion of the completion of this thesis, it is my pleasure to express my sincere gratitude for all those whose support and encouragement made my research journey much easier.

I would like first to express my deepest respect to my thesis director Pr. Emmanuelle Deleporte to whom I owe my profound gratitude for giving me the opportunity to work within the team. It was really my pleasure to complete my PhD studies within such a team. Thank you for your continuous asking, your understanding, your sympathy and your precious help since the day I arrived to ENS-Cachan.

I would also like to take this opportunity to express my heartiest thanks and appreciation to Pr. Jean Sébastien Lauret, who has followed up my studies in its finest details. Thank you for your good humor, motivation, disponibility, constructive ideas, for all the explanations and the fruitful discussions.

I would like to express my gratitude to the jury of my thesis defense: to Jacky Even for chairing the jury, to Pierre Gilliot and Catherine Schwob for accepting to be my referees, to read and evaluate my manuscript and last but not least to Joël Leymarie for participating at my defense.

This thesis research was done in numerous collaborations. Consequently, I would like to express my gratitude to the collaborators and colleagues to whom I owe this wonderful experience. For their invaluable contribution I thank Jacqueline Bloch, Sophie Bouchoule Zheng Han and Hai-Son Nguyen from Laboratoire de Photonique et Nanostructures (LPN) in Marcoussis, France.

I would like to thank also Joseph Lautru from IDA for advices on technological aspects in clean room of institute d'Alembert.

TABLE OF CONTENTS

Introduction

The topic of light-matter interaction in semiconductors has long been the subject of a huge research effort because of both its importance in the fundamental understanding of these solids and the many applications that depend on it. On the former aspect we can cite the photoconductivity property, light emission capability and various electro-optic and nonlinear effects. On the latter aspect, we recall such large scale applications as light detectors, LEDs and laser diodes, photovoltaic generators, displays, etc.[1]

From the very beginning, it has been recognized that the fundamental optical properties of semiconductors are intimately linked to features originating in the symmetry and dimensionality of the electron system. In an optical transition, an electron from the valence band is promoted to the conduction band. Therefore, it leaves an electron vacancy in the valence band which can be described as a positive particle named a hole. The electron-hole pair in Coulombic interaction is called an exciton. Depending on their density and temperature, excitons can behave as a weakly interacting Bose gas. It has been understood by Moskalenko [2] and Blatt [3] that excitons remain in the gas phase at low densities and low temperature and are therefore good candidates for observation of Bose-Einstein condensation (BEC). The clearer signature of exciton Bose-Einstein condensation should be the emission of a coherent light by spontaneous recombination of condensed excitons [4]. In order to enhance the coupling between excitons and photons, photons can be confined in cavities, leading to the formation of polaritons, half-light half-matter quasi-particles existing when the light-matter strong coupling regime is reached. This field has been intensively studied due to the interest in coherent and stimulated effects in such systems which can lead to optical devices. In particular, the properties of polaritons to form a Bose-Einstein condensate may lead to the realization of low threshold polariton lasers.

From the point of view of materials, most studies of exciton-photon coupling in such strong coupling cavities focus on using InAs-GAAs emitters (semiconductor Quantum Dots and Quantum Wells) in high Q-factor planar microcavities at low temperatures [5, 6]. In order to raise the working temperature of these polariton-based devices up to room temperature, a lot of efforts has been put on alternative semiconductors presenting large exciton binding energies and oscillator strengths such as GaN [7, 8], ZnO [9], and organic materials [10-11].

Besides the inorganic semiconductors and the organic materials, an interesting class of materials is intensively studied: the hybrid materials, which are expected to combine the attractive features of organic materials and inorganic materials within a single molecular-scale composite, and can be synergistically exploited to overcome the limitations of organic and inorganic materials. In the past two decades, the organic-inorganic hybrid perovskites have arisen as a new functional material and have drawn great attention and research effort.

Due to the belief that organic-inorganic hybrid semiconductor inside microcavities could open the way to realize polariton lasers at room temperature, the team "NANOPHOT" of LAC/ ENS Cachan has performed a lot of studies and has successfully realized [12-22] :

1. strong coupling regime at room temperature in microcavities containing two-dimensional layered organic-inorganic perovskites, emitting in green, blue and near UV range
2. strong coupling regime at room temperature in hybrid vertical microcavities containing a layer of inorganic semiconductors such as GaN or ZnO and a perovskite layer
3. optical optimization of new functionalized organic-inorganic hybrid perovskites for applications in microcavities and photonics.

In order to go further, a better understanding of the electronic structure as well as the excitonic interactions in perovskite thin layers are necessary [23, 24]. The knowledge of the carrier dynamics is of particular importance since it governs excitonic non-linearities which are at the basis of operations in optoelectronic devices. One of these fundamental non-linearities is the absorption coefficient saturation of the excitonic transition in presence either of free carriers in the continuum or excitons. These important issues bring about the research subject of this thesis where we focus our attention on a particular group of perovskites: the two-dimensional (2D) layered lead halide perovskites.

Thus, this manuscript is developed in four chapters as follows:

In Chapter 1, we talk about the organic-inorganic hybrid materials and introduce the chemical composition and crystal structure of perovskites compounds. We present the preparation and deposition techniques of 2D layered perovskites. We also present the optical and structural characterizations of the two-dimensional perovskites which will be mainly studied in this manuscript. Moreover, we discuss the strong coupling regime observed in semiconductor microcavities containing these 2D-perovskites.

Chapter 2 presents the different experimental techniques used to characterize the optical properties of both perovskite thin films and microcavities containing them. Besides, we detail

a complete description of the fabrication of Standard perovskite based microcavities covered with a silver metallic mirror.

Chapter 3 presents the exciton dynamics in the $(C_6H_5\text{-}C_2H_4\text{-}NH_3)_2PbI_4$ layered perovskite by means of pump/probe spectroscopy performed at room temperature and at low carriers density where multiexcitonic effects are negligible. Both interband and intraband relaxations are investigated. The origin of the saturation of the absorption coefficient is demonstrated, and a theory reported for 2D excitons is presented. Finally, exciton-exciton interactions are probed through experiments as a function of the injected carriers density.

Finally, Chapter 4 is devoted to a new assembly technique making use of top-dielectric mirror migration in a liquid. It is based on the migration in liquid of the top dielectric mirror allowing a significant increase of the cavity mode quality factor. Both angle resolved reflectivity and microphotoluminescence measurements are performed to characterize the optical properties of this high quality perovskite based microcavity. Besides, zero-dimensional cavity polaritons have been demonstrated at room temperature. Finally, a new perovskite has been synthesized to improve the materials photostability.

Chapter1

1.   Hybrid Organic-Inorganic perovskite

Perovskite materials represent a very large family of compounds, which ramify to many groups. One of them is the Hybrid organic-inorganic perovskites which provide significant opportunities as multifunctional materials for many electronic and optoelectronic applications, such as organic-inorganic field-effect transistors [25], or nonlinear optical switches based on strong exciton-photon coupling in microcavity photonic architectures. Very recently, hybrid organic-inorganic perovskites have been suggested as a new class of low-cost material for high efficiency photovoltaic cells [26-28].

In the last years, an increasing number of studies were dedicated on hybrid organic-inorganic materials due to the possibility of combining the advantages of both materials. Organic compounds offer a number of useful properties including structural diversity, ease of processing and high luminescence quantum yield at room temperature. On the other side, inorganic materials have a distinct set of advantages, including good electrical mobility, band gap tunability (enabling the design of metals, semiconductors, and insulators), mechanical and thermal stability, and interesting magnetic or electric properties.

We are interested in a specific class of hybrid compounds: 2D layered organic-inorganic hybrid perovskites. In this chapter, we will show that they are an original kind of semiconductor for optoelectronics. First, we will talk about the general properties of some organic-inorganic hybrid materials, specifically focusing our attention on the hybrid perovskites semiconductors. Then, we will talk about the fabrication of perovskites samples, from the synthesis of chemical compounds to the formation of two dimensional layered thin films. Experimental methods used to characterize crystal structure, surface topography, and optical resonances will be presented.

1.1.   Perovskite Crystal Structure

Perovskite crystal is a relatively rare ionic crystal whose chemical formula is $CaTiO_3$. It was discovered in 1839 in the Ural mountains of Russia by Gustav Rose and is named after in the honor of a Russian mineralogist L.A. Pervoski (1792-1856).

Generally, the term "perovskite" includes crystals having the same structure as the perovskite and whose chemical formula is of the form AMX_3. The basic 3D perovskite structure AMX_3 is schematically depicted in **Figure 1.1**. It consists of corner-sharing MX_6

octahedra, where X is typically an anion: Cl^-, Br^-, or I^-. In order to satisfy the charge balancing requirements, the M cation is generally a divalent metal that can adopt an octahedral anion coordination, such as Ge^{2+}, Sn^{2+}, Pb^{2+}, Co^{2+}, Fe^{2+}, Cu^{2+}, Ni^{2+}, Mn^{2+}, Cr^{2+}, Pd^{2+}, Cd^{2+}, Ge^{2+}, Sn^{2+}, Pb^{2+}, Eu^{2+}, or Yb^{2+}. The A ions fill the large 12-fold coordinated holes between the octahedra.

The size of A ions influences a lot the perovskite structure. Here we define t as the tolerance factor which satisfies the relation:

$$\left(R_A + R_X\right) = t\sqrt{2}\left(R_M + R_X\right) \tag{1.1}$$

where R_A, R_M, and R_X are ionic radii of A, M, and X ions respectively. The values of R_A+R_X and R_M+R_X are supposed to be approximately the distance A-X and M-X respectively. For perfect 3D network, Perovskite has a cubic structure wherein the tolerance t is equal to 1.
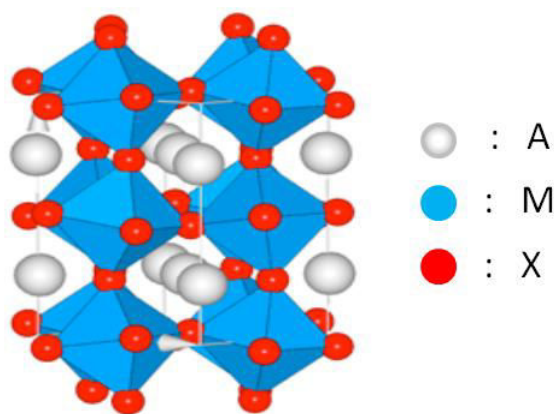
Figure 1.1 Basic AMX_3 perovskite structure

Besides the 3D network, the 2-dimensional network is a common structure for organic-inorganic hybrid perovskites. It happens when the organic group A is too large to fit into the space provided by the nearest-neighbors X within the inorganic sheet, causing the distortion of the cubic structure. The tolerance factor is much larger than 1 in this case and the organic group needs to be held away from the inorganic sheets by a spacer, such as an alkyl chain, in order to grow 2D perovskites layered structures.

The 2D layered perovskite compounds of general formula: $(R-NH_3)_2MX_4$, where R is an aliphatic or aromatic ammonium cation, M is a divalent metal that can adopt an octahedral coordination, and X is a halogen, are one of the typical self assembled materials. In $(R-NH_3)_2MX_4$ systems shown in **Figure1.2**, the perovskites consist of single layers of oriented inorganic sheets separated by bilayers of organic ammonium cations, where the organic groups R self-assemble via "π - π" interaction (when the organic group contains aromatic groups) or through Van der Waals force (when the organic group contains alkyl chains).
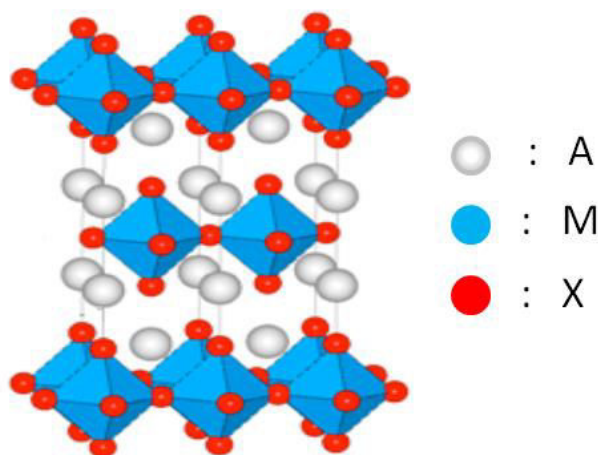
Figure1. 2 Sketch of 2D organic-inorganic perovskite $(R\text{-}NH_3)_2MX_4$.

1.2. Preparation of perovskite layers

In this section we will introduce the perovskite crystals performed in our laboratory in layered film form. Method of preparation and some factors that may influence surface quality of layered films will be discussed.

The synthesis of perovskites is a primary and important procedure among perovskites study. The fabrication of perovskites is relatively easy compared to that of other traditional semiconductors which needs huge equipments and strict environment conditions. The perovskites thin films are deposited using simple techniques such as spin coating, dip coating or evaporation. In our work, we have chosen the spin coating technique for all film depositions. The perovskites that we are interested in and that we synthesize are mainly in the form of $(R\text{-}NH_3)_2PbX_4$. The protocol developed in this manuscript concerns a particular perovskite, namely (bi-(phenethylammonium) tetraiodoplumbate, PEPI): $(C_6H_5C_2H_4NH_3)_2\ PbI_4$. Generally, the synthesis of a perovskite thin film occurs in three steps: synthesis of ammonium salts, preparation of perovskites solution and deposition on a substrate.

1.2.1. Synthesis of ammonium salt precursors

Generally, Ammonia salts can be synthesized by reacting different amines (monoamine $R\text{-}NH_2$ or diamine $H_2N\text{-}R\text{-}NH_2$) with halogen acid (HX).This reaction is described by **equation1.2**.

$$R\text{-}NH_2 + HX \rightarrow R\text{-}NH_2.HX \qquad (1.2)$$

7

It is a neutralization reaction where the salts are easy to generate with a yield rate of relatively high level (nearly 100%). We have synthesized different organic salts; however we present here the synthesis of "phenethylamine iodide salt" $C_6H_5C_2H_4$-NH_3I which is involved in the preparation of PEPI perovskite that is the main perovskite studied in this thesis. The halogen acid used is HI 57 wt% aqueous solution purchased from Sigma Aldrich Company. For the organic part, 2-phenylethanamine commercially available is used. This reaction is described by **equation1.3**

$$C_6H_5C_2H_4\text{-}NH_2 + HI \rightarrow C_6H_5C_2H_4\text{-}NH_3I \tag{1.3}$$

The reaction setup is shown in **Figure 1.3**. The setup is proposed by Pierre Audebert and mounted by Laurent Galmiche at PPSM[1], the chemistry laboratory at ENS Cachan.
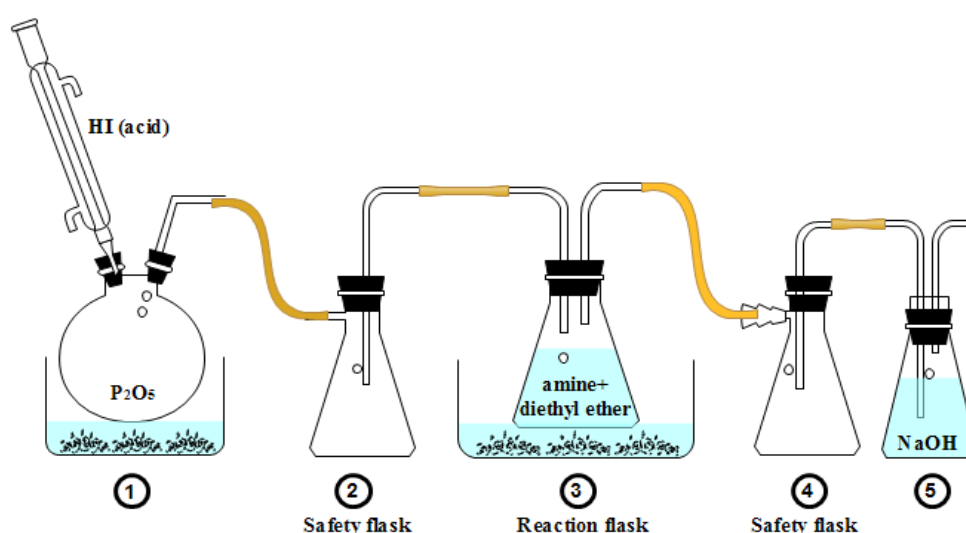
Figure 1.3 Reaction setup to produce the ammonium salts.

Gaseous HI is obtained in flask 1 by dropping excess concentrated HI acid gingerly on P_2O_5 powder, with the bottle placed in ice water path (for cooling) since the dehydration process of P_2O_5 to HI solution is exothermic and dangerous. Gaseous HI is then guided by pipes through the first safety flask to the reaction flask as soon as it is generated. In the reaction flask, precipitate of small white grains of $C_6H_5C_2H_4$-NH_3I salts are obtained as HI gas reacts with $C_6H_5C_2H_4$-NH_2 (phenylethyl amine) dissolved in diethyl ether. The reason to choose diethyl ether in the reaction flask comes from the fact that it is a very good solvent for amines on the one hand, and that the salts have very low solubility in it on the other hand. Therefore the

---

1 *Laboratory of Photophysics and Photochemistry Supramolecular and Macromolecular, ENS, Cachan.*

generated ammonium salts tend to precipitate out of solution while the reaction is in progress. Moreover, diethyl ether has the ability to separate the reactant from final salts which insures the purity of ammonium salts. Meanwhile, an ice-water bath under reaction flask will favor the precipitation process. After the reaction flask, unreacted HI gas is guided by pipes through secondly safety flask to a bottle containing NaOH aqueous solution. This bottle serves as gas-washing bottle to neutralize the unreacted HI gas.

However this gaseous acid method is relatively long and may cause the pipes to be eroded. So, we tried to synthesize ammonium salts by adding aqueous acid to amines in diethyl ether solution directly. Thus white grains of $C_6H_5C_2H_4-NH_3I$ salts are obtained as HI aqueous acid reacts with $C_6H_5C_2H_4-NH_2$ in diethyl ether. Then these salts are filtered and rinsed two times by diethyl ether and one time by n-pentane to remove the unreacted HI acid, $C_6H_5C_2H_4-NH_2$ as well as water traces. This method simplifies the fabrication procedure and enables us to fabricate larger quantities of ammonium salt by single reaction. However it may introduce some water to reaction solution which is unfavorable for the generation of perovskites. So, ammonium salts are placed under vacuum line for several hours to eliminate the residual solvents and then transferred in the desiccator for few days to remove the traces of water and to be completely dried.

The synthesis protocol that we followed in the preparation of phenylethylamine iodide salt includes the addition of hydroiodic acid solution (191.51 mmol, 14.4 ml) to phenylethylamine (101.13 mmol, 12.7 ml). The phenylethylamine iodide salt was obtained (21 g) at 83% yield.

1.2.2. Perovskite solution and its deposition on a substrate

After few days of drying in the desiccator, the salts are ready to be used. These dry ammonium salts are used to prepare perovskites solutions.

Each ammonia salt (organic) was mixed with PbI_2 in a stoichiometric ratio of 2:1, and then dissolved in dimethylformamide (DMF) solvent at a 1:10 mass ratio to form PEPI perovskite. This reaction is described by **equation 1.4**. Since 2-phenylethanamine is used as the organic group of PEPI perovskite, $\left(C_6H_5C_2H_4NH_3^+\right)_2$ $(C_6H_5C_2H_4NH_3^+)_2$ is noted as PhE hereafter for convenience. And thus, $(C_6H_5C_2H_4NH_3)_2PbI_4$ will be referred as PhE-PbI$_4$.

$$2 \ (C_6H_5C_2H_4-NH_3I) + PbI_2 \rightarrow (C_6H_5C_2H_4-NH_3)_2PbI_4 \qquad \textbf{(1.4)}$$
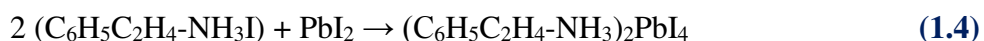
Our thin films samples are realized by spin coating, by which the perovskites form 2D-layered crystals by self-organization process. The effect of self organization can be optically

characterized. For instance, we see a sharp resonant peak at 517 nm in the optical absorption spectrum of a PEPI thin film, which doesn't exist for PEPI solution (**Figure 1.4**). This line is characteristic of the self-organization that took place during spin coating. More details about the origin of this peak will be discussed later in the manuscript.
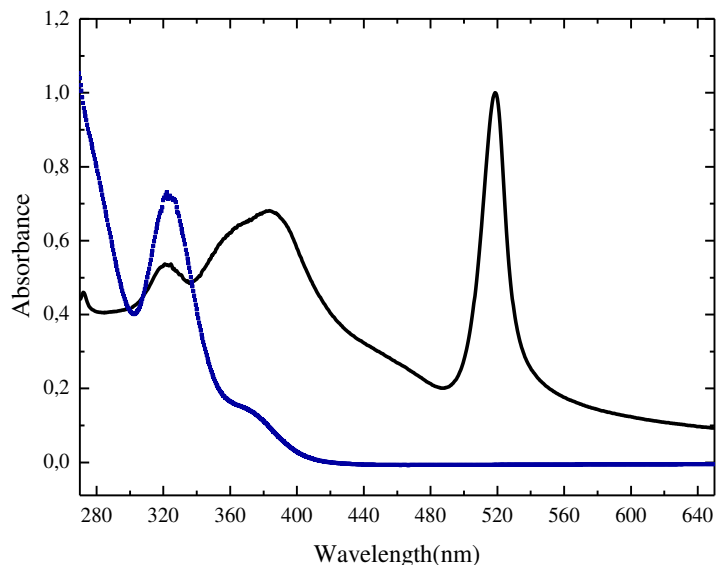
Figure 1.4 OA spectra of a 50 nm PEPI thin film (black line) and of a solution containing PEPI dissolved in DMF solvent (blue line).

Spin-coating is a very simple method, compared to the deposition techniques used for inorganic semiconductors such as MBE (Molecular Beam Epitaxy), MOCVD (Metal Organic Chemical Vapor Deposition) and PECVD (Plasma Enhanced Chemical Vapour Deposition). The technique of spin-coating applied for the deposition of perovskite is shown in **Figure 1.5**:

1. Place a quartz substrate on a spinner
2. Using a syringe, release few drops of the solution containing the constituents of the perovskite on the substrate
3. Start the spinner after entering some parameters: spin speed, spin acceleration and spin duration depending on the size of the sample and the desired thickness of perovskite. Actually, in order to realize a layer with the desired thickness, we modify the concentration of perovskites solution keeping the spin coating parameters fixed, such that less concentrated solutions give thinner layers.
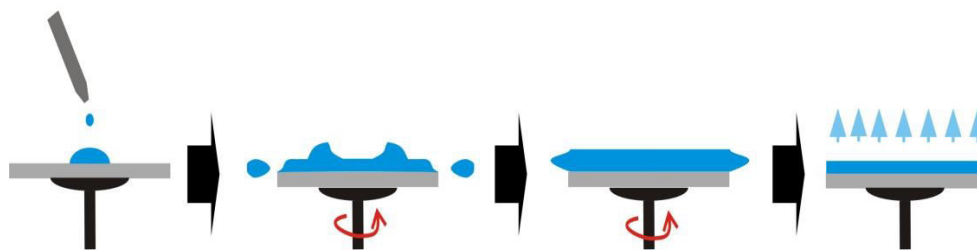
Figure 1.5 Schema of the spin coating process.

An important issue for preparing homogeneous perovskite films is the surface effect related to substrate. Prior to preparing perovskite films on quartz slides, we first cleaned the surface subsequently by acetone, ethanol and propanol in ultrasonic bath, where each step lasted for 15 min. After that, the quartz slides were immersed in 1mol L⁻¹ KOH in ethanol solution for 15 min for modifying the surface charge [29]. Then the slides were rinsed by distilled water and dried by nitrogen flow. The homogeneity of perovskite films prepared on KOH treated surface is better than on untreated surface.

After the spin-coating process, the samples are placed on a hot plate for annealing. The annealing conditions are very crucial for the formation of crystals. If the annealing temperature and time are too small, the films may present relatively weak optical absorption; on the contrary, the perovskites will be destroyed and decomposed if the annealing temperature is too high and the annealing time too long. The annealing parameters depend a lot on the perovskite composition and also on the solvent [21]. The parameters determined for preparing, on slide of quartz of 4 cm², 50 nm PEPI thin layers with PEPI 10% in DMF solution are: rotational speed of 1500 rpm during 30 second, and then heating the sample during about one minute at 95 ° C to evaporate the remaining solvent.

To prevent PEPI layer from degradation due to humidity and oxygen, we put the perovskites samples in He environment or we add a transparent polymer PMMA (Poly(methyl methacrylate)) layer on the top of perovskites layer. PMMA can be deposited by spin coating with the parameters: 1000 rpm (rotational speed) during 40 sec (time) and then heating it for twenty minute at 95°C.

The spin coating perovskite films are very reproducible, and are appropriate to make devices [3]. **Figure 1.6** shows the optical absorbance measurements on two PEPI layers where the time interval between their fabrications is around three months.
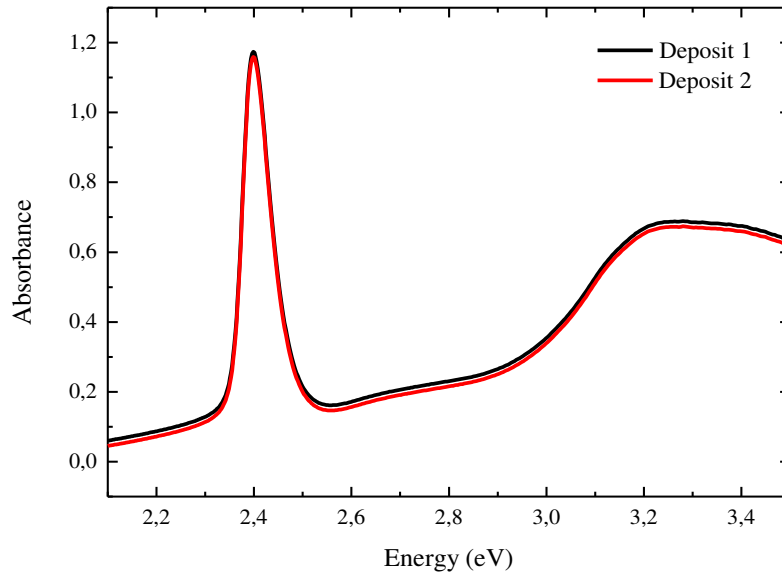
Figure 1.6 O.A of two PEPI layers fabricated at different times

1.3. Structural Characterizations

In this section, we introduce the characterization techniques that are frequently used in our studies of PEPI perovskite: structural characterizations such as the X-ray Diffraction and Atomic Force Microscopy.

1.3.1. X-ray diffraction

The properties of a material can often be linked back to the arrangement of atoms in its crystal structure. X-ray diffraction (XRD) is a non-destructive analytical technique which can yield the unique fingerprint of Bragg reflections associated with a crystal structure.

Crystal structure is considered as being built of planes of atoms, where each plane acts as a semi-transparent mirror. An X-ray beam impinging on a crystal at an angle θ will be scattered in all directions by the atoms of the crystal. In some directions, an increased intensity is observed due to the constructive interference of the scattered waves. The conditions for constructive interference are easily derived from the simple geometric picture for the scattering of an X-ray beam by planes of atoms in a crystal, shown in **Figure 1.7**. Constructive interference will be observed for X-rays that are reflected from the planes at a specular angle if the path length difference between X-rays scattered from different planes is an integer times the wavelength. This condition is summarized in Bragg's law:

$$2d\sin\theta = p\lambda \tag{1.5}$$

where λ is the wavelength of the X-ray, θ is the scattered angle, d is the inter-planar distance and p is an integer representing the order of the diffraction peak. An X-ray diffraction pattern is then obtained by scanning the sample over a range of θ angles.
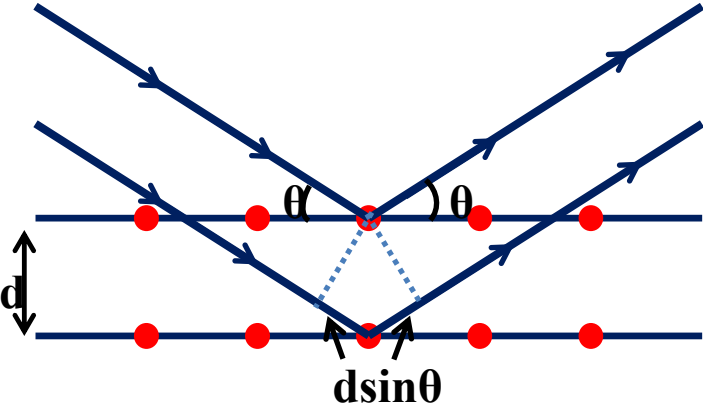
Figure 1.7 X-ray diffraction principle.

X-Ray Diffraction measurements on PEPI thin films were performed at LPN by Ludovic Largeau and Olivia Mauguin. The results of these measurements are part of a paper published in 2010 in Optics Express [24]. **Figure 1.8** presents XRD pattern measured on a spin-coated 50 nm thick PEPI film deposited on fused quartz substrate. Numerous diffraction orders from (0 0 2) to (0 0 24) are observed. The observation of numerous diffraction orders proves the high crystallinity of the thin layer and the very good periodicity of the stacking. A period of 1.64 nm is accurately estimated from the patterns of **Figure 1.8**. This value is very coherent with those given by literature [30, 31].
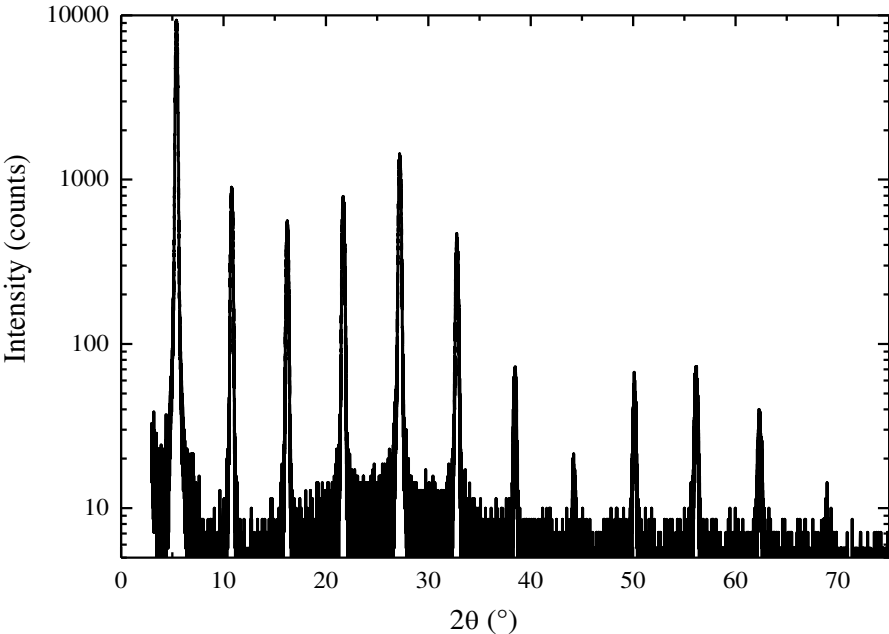
Figure 1.8 X-Ray Diffraction patterns of a spin-coated 50-nm-thick PEPI layer.

1.3.2. Atomic Force Microscopy

The Atomic Force Microscopy (AFM) is a frequently-used tool that we employ to characterize the surface topography of the 2D perovskite. It gives us direct information about the surface quality by providing a way to evaluate the surface roughness with quantified values. This is so important, for example, in the realization of microcavities containing perovskites where an active layer with large roughness reduces the quality factor of the cavity.

To determine the effect of the spin coating process on the surface topography of the perovskite thin films, the surface profiles of the $(R-NH_3)_2PbI_4$ perovskites were measured. The room-temperature AFM images of the various thin films were recorded on VEECO Explorer microscope of PPSM laboratory. Non-contact mode tip was used for all measurements. The scan area was typically 2*2 micrometers.

The average surface roughness (Δ) of the thin films was calculated from the AFM surface topographic data in a scanning area of 2 μm x 2 μm by the **equation 1.6**:

$$\Delta = \sqrt{\frac{1}{N} \sum_{i=1}^{N} (x_i - x_{ave})^2}$$

(1.6)

where N is the total number of pixels in each AFM image, x_i the height at the ith pixel, and x_{ave} is the average height for each AFM image. The factors that may influence the surface quality are various. For example it depends on the nature of the substrate. Moreover, the concentration of the 2D perovskite greatly affects the surface roughness. Concerning the concentration parameter, the decrease of solution concentration helps improving the surface quality. **Figure 1.9 (a)** and **(b)** show the topography of PEPI 10% and 1% thin films. These two samples are prepared by depositing a 10wt% and 1wt% PEPI solution by spin coating with the parameters: 200rmp, 2000rmps during 30sec and annealing at 95°C for 1 min, resulting in thickness of about 50 nm and 6 nm respectively. The values of average roughness of these samples calculated with **equation 1.6** are 10.5 and 1.27 nm for PEPI 10% and 1% respectively. The AFM images in **Figure 1.9 (a)** and **(b)** clearly show the effect of solution concentration on surface roughness.

(a) PEPI 10% thin film   **(b)** PEPI 1% thin film
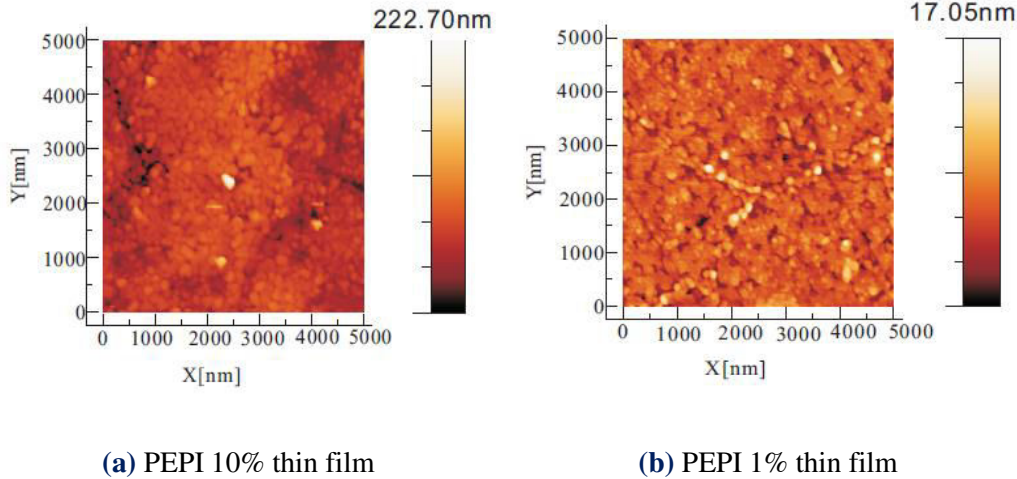
Figure 1.9 AFM images for PEPI thin films prepared from 10%, and 1% solutions, and deposited on quartz substrate, performed by Y.Wei at PPSM-ENS Cachan.

We have also synthesized new perovskite thin layers: p-fluorophenethylamine tetraiodoplumate perovskite, whose chemical formula is $(pFC_6H_5C_2H_4NH_3)_2PbI_4$ (abbreviated as 4FPEPI hereafter), included in a PMMA (PolyMethylMetAcrylate) matrix. **Figure 1.10** shows the topography of 4FPEPI doped 10% PMMA. This sample is prepared by depositing 4FPEPI doped 10% PMMA solution on quartz substrate. To prepare this solution, a transparent polymer PMMA and a stoichiometric amount of the ammonium salt and PbI_2 are dissolved into DMF. The concentration of PMMA in DMF is 10 wt% and the weight ratio of perovskite/PMMA is fixed at 1:5. With this solution, spin coating is performed at 2000 rpm, 2000 rpms, 40s; annealing condition is 150°C for 90 min. The solution where the concentration of PMMA in DMF is 10 wt%, gives a layer of thickness of about 350 nm. The average roughness Δ is found to be 0.86 nm. As a consequence, we can conclude that this method of deposition allows improving the roughness of the layer, so it may be interesting in the framework of the realization of the perovskite-based microcavities.
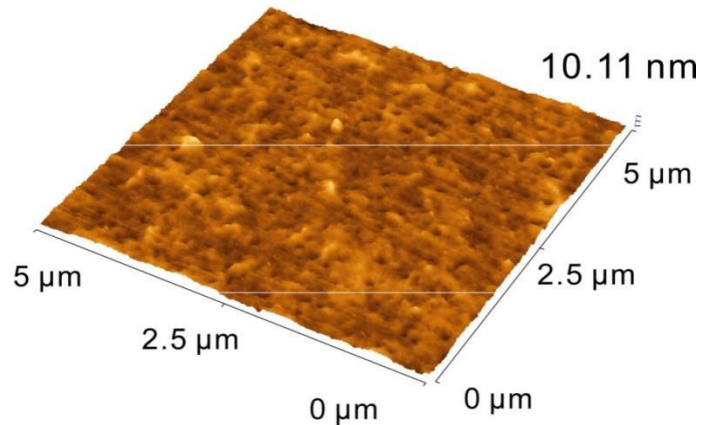
Figure 1.10 AFM image for a 4FPEPI doped 10% PMMA thin film deposited on a quartz substrate performed by Y.Wei at PPSM-ENS Cachan.

15

1.4. Electronic structure of 2D perovskites

The unique structural and chemical characteristics of the organic-inorganic perovskites provide for equally interesting and potentially useful physical properties. The electronic structure of 2D perovskites is schematically shown in **Figure 1.11**. It consists of alternating organic and inorganic layers of thickness about 1 and 0.6 nm respectively. The electronic structure of 2D layered organic-inorganic perovskites can be regarded as a self-organized multiple quantum well structure, consisting of organic layer that forms the barrier, and the inorganic layer being the well. Because the HOMO-LUMO (Highest Occupied Molecular Orbital and Lowest Unoccupied Molecular Orbital) energy gap of the inorganic layers (2-3 eV) is smaller than that of the organic layers (5-6 eV), the lowest exciton (exciton is an electron-hole pair bound by coulombic interaction) is confined in the inorganic layer. Moreover, the organic ammonium groups have a low relative dielectric constant of about 2.4 while the metal halide layers possess a high relative dielectric constant of about 6.1. By virtue of this high contrast in dielectric constant between the organic layers and the inorganic layers, the Coulomb interaction in the well layer is hardly screened by the presence of barrier layers. Namely, the interaction between an electron and a hole in an exciton is strengthened, which is referred to as "dielectric confinement" effect [41]. This quantum and dielectric confinement in 2D organic-inorganic perovskites results in large exciton binding energies of a few hundred of meV and huge oscillator strengths: the order of magnitude of the oscillator strength per quantum well in $(C_6H_5C_2H_4-NH_3)_2PbI_4$ is 4×10^{13} cm^{-3} [32], which is one order of magnitude higher than that of conventional inorganic semiconductor quantum wells [33]. Indeed, such layered structures have been demonstrated to show enhanced non-linear optical properties in microcavities [13].
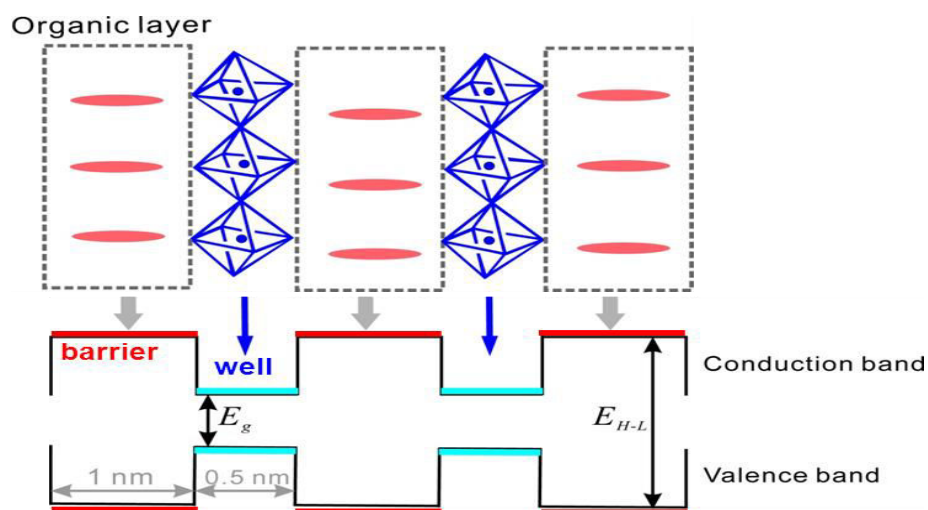
Figure 1.11 Schematic electronic structure of 2D layered organic-inorganic perovskites

Numerous self-assembled hybrid organic-inorganic perovskite systems with lead halide have been studied, but their electronic band structures are not known precisely. Density Functional Theory (DFT) calculations have been performed by J. Even et al on a prototype Single Crystal Hybrid Organic-Inorganic layered perovskite combined with symmetry analysis of the band edge Bloch states [34]. Density Functional Theory (DFT) is usually used to study the structural, electronic and vibrational properties of the system. **Figure 1.12** shows the band structure of monocrystalline 4FPEPI with and without spin orbit coupling (SOC). Note that no excitonic effect has been taken into consideration at this step of the calculation. It reveals a direct band gap character where the fundamental transitions with and without SOC are of 1.2 and 2 eV respectively. Moreover, the optical absorption near the band edge without SOC is modeled by three active Bloch states at Γ point: a non degenerate level for the valence-band maximum (VBM) and two nearly doubly degenerate levels for the conduction band minimum (CBM). This ordering of the band edge states is found reversed compared to tetrahedrally bonded conventional semiconductor structures. Interestingly, it has also been shown that the spin orbit coupling (SOC) induces a large splitting of the conduction bands (1.2 eV) [34], in comparison to the splitting of the valence bands of conventional semiconductor [33].
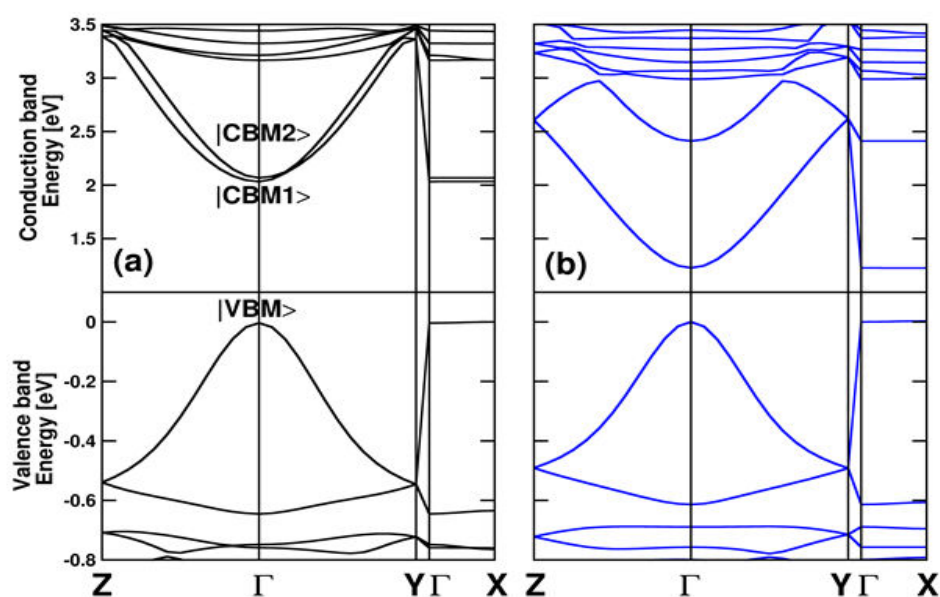
Figure 1.12 Electronic band structure of 4FPEPI (a) without and (b) with the spin-orbit coupling interaction calculated by the Density Functional Theory. The energy levels are referenced to the valence band maximum [34].

Recently, both 2D and 3D hybrid organic-inorganic perovskite crystal structures based on Density Functional Theory calculations and symmetry analysis have been investigated. The findings reveal the universal features of the electronic band structure for the class of lead-halide

17

hybrids $(R-NH_3)_nPbX_m$, where $(n,m) = (2,4)$ and $(1,3)$ respectively for 2D and 3D structures, providing a clear sight inside their electronic and optical properties [35].

1.5. Optical characterization of the perovskite thin films

In this section, we will introduce some frequently-used optical methods for the characterization of perovskites. Experimental principles and set-ups for absorption and photoluminescence spectroscopy will be presented.

1.5.1. Optical absorption spectrum at room temperature

The basic process for an optical transition in highly simplified energy diagram of two separated bands in a semiconductor is shown in **Figure 1.13**. The energy gap between the bands is called the band gap E_g. By absorbing a photon, an electron is promoted from the valence band at lower energy to conduction band at higher energy.
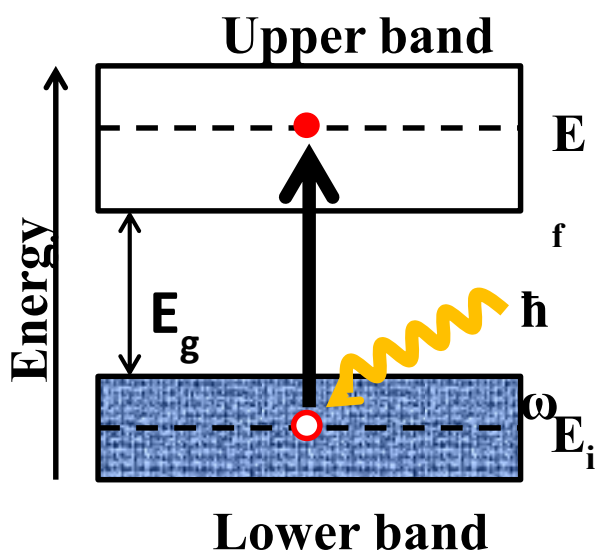
Figure 1.13 Interband optical absorption between an initial state of energy E_i in an occupied lower band and a final state at energy E_f in an empty upper band. The energy difference between the two bands is E_g.

Figure 1.14 shows the absorption spectrum of a spin-coated 50 nm thick PEPI film .We observe a sharp absorption peak at 2.40 eV which is attributed to the excitonic absorption of PEPI, the Full Width at Half Maximum (FWHM) of this peak is 73meV. The appearance of an intense excitonic absorption peak denotes that a layered perovskite structure was formed in the spin-coated film. In this figure, the number of quantum wells is of the order of 30 (thickness of the perovskite layer: 50 nm). When the film thickness decreases, the number of quantum wells decreases but the width of the excitonic peak does not vary. The inset of **Figure 1.14** shows the

normalized optical spectra of two PEPI films of different thicknesses. The contributions to the linewidth of the excitonic line are due to interactions with phonons, trapping of carriers on impurities and fluctuations in the thickness of the well as observed in GaAs "classical" quantum wells [36]. Due to the fact that the 2D-layered perovskite is self-assembled and to the fact that the width of the excitonic line doesn't depend on the number of wells, we think that the linewidth is mainly due to exciton-phonon interaction.
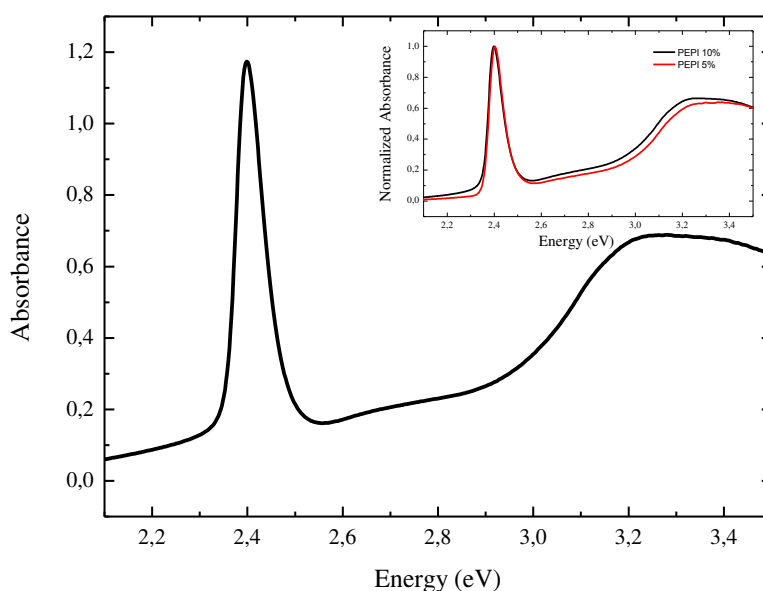
Figure 1.14 Absorption Spectrum of 50 nm PEPI on glass slide (black line). Inset: 50 nm thick PEPI (black line), 25 nm thock PEPI (red line).

1.5.2. Photoluminescence spectrum at room temperature

Photoluminescence (PL) is one of the most remarkable properties of 2D organic-inorganic perovskites. When a laser is sent on the sample, a non-equilibrium electron-hole pair due to the transfer of electrons from the valence into the conduction band is created, which tends to relax back by emission of phonons or photons. The process in which a significant portion of the created excitons recombine by emission of photons is known as photoluminescence (**Figure 1.15**). The study of PL peaks intensity as a function of illumination time allows evaluating the photo-stability of the perovskites.

Figure 1.16a shows PL spectrum of a layer of 50 nm PEPI deposited on quartz measured at room temperature. The PL intensity is normalized to 1. We can observe that the PL of PEPI is centered at 2.37eV (λ_{PL}=523 nm), and the Full Width at Half Maximum (FWHM) of the line is 62meV. The emission is bright green and can be seen by naked eyes as shown on the photo in **Figure16b**.
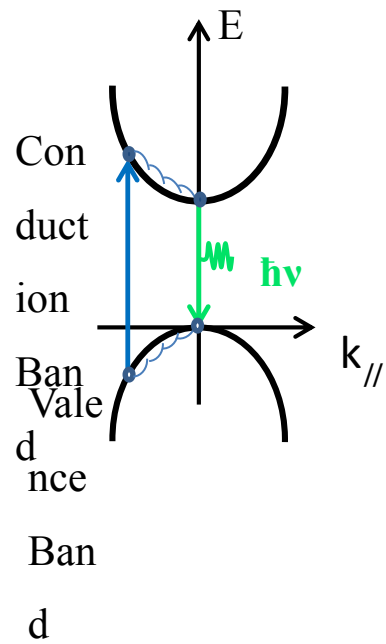
Figure1.15: Schematic band diagram for photoluminescence process
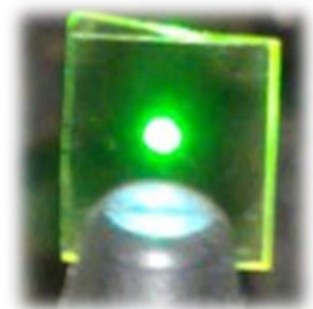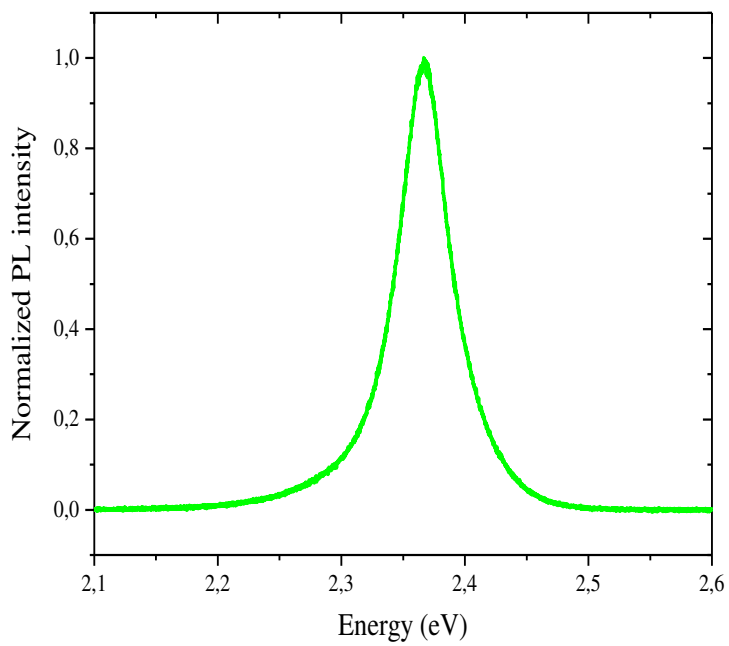
Figure1.16 Photoluminescence of 50 nm thin film of PEPI (the excitation wavelength is 405nm, from a diode laser)

Comparison between absorption and photoluminescence spectra

By comparing the O.A spectrum and the photoluminescence spectrum of the PEPI film, we notice an energy difference between the absorption and PL maxima defined as the Stokes shift, equal to 38 meV as shown in **Figure1.17**. Moreover, the widths of the two peaks are of the same order of magnitude: the linewidths of the optical density and photoluminescence spectra are 73 meV and 62 meV respectively.
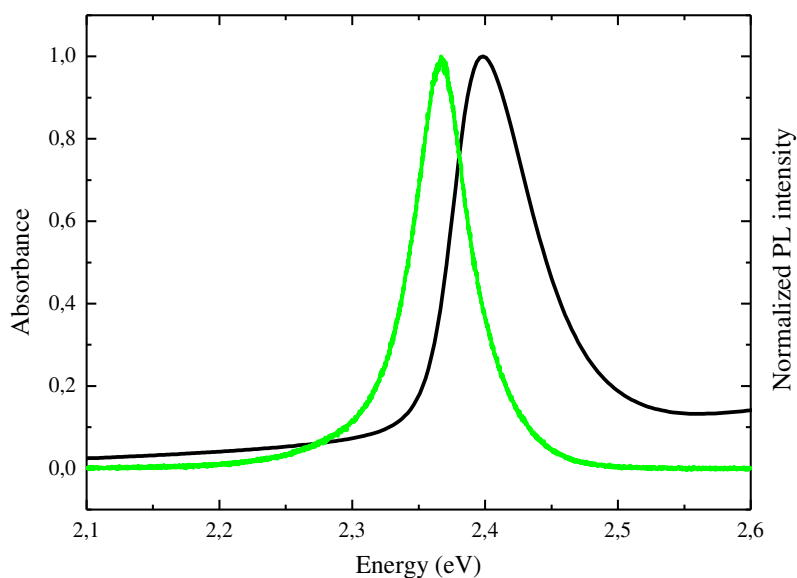
Figure 1.17 Normalized photoluminescence (green line) and absorption spectra

1.6.   Flexibility and applications of 2D Perovskites

Among all the unique features of 2D-layered perovskites, one of the most important is their strong flexibility. For the mostly used 2D layered $(R-NH_3)_2MX_4$ perovskites, the organic part is optically inert and the optical transition energy is mainly decided by the inorganic part. The width of the wells is mainly controlled by the M-X bond length, while the width of the barrier is controlled by the organic radical R. The depth of the well is controlled by M and X species, that is to say, the spectral position of the excitonic transitions can be tailored by substituting different metal cations or halides within the inorganic part. In particular, it is possible to have excitonic lines over a range of wavelengths covering the visible and near ultraviolet by changing X [12, 37-39], it covers also the infrared range by changing Pb to Sn [40]. Furthermore, the lengths of the R group can dramatically influence the molecular rigidity as well as the distance between inorganic sheets and then the self-assembly ability [18]. It can also influence the contrast of dielectric constant between organic and inorganic layers which will affect the exciton binding energy. Indeed, this flexibility lies in the great diversity of

molecules provided by chemistry. In collaboration with Pierre Audebert (PPSM-ENS Cachan), various perovskites have been developed by varying either the organic chain or halogen, depending on the property that we want to adjust in our studies. For example, we have increased the photoluminescence efficiency and the self-assembly properties of the 2D perovskites by changing the organic group [18]. In all our studies, the metal used was always the lead.

An example of flexibility of 2D perovskites is clearly shown in **Figure 1.18**, where the OA spectra of PhE-PbX$_4$ are presented for different X. The excitonic peaks of PhE-PbX$_4$ locate at 2.4 eV, 3.08 eV, and 3.64 eV for X = I, Br and Cl respectively. The excitonic absorption peak of PhE-PbI$_4$ (PEPI) is attributed to the electronic transition from Pb(6s)-I(5p) mixed states to Pb(6p) states [41]. Similarly the excitonic absorption peaks are due to transition from Pb(6s)-Br(4p) states to Pb(6p) state for PEPB [39] and from Pb(6s)-Cl(3p) states to Pb(6p) state for PEPC [39].
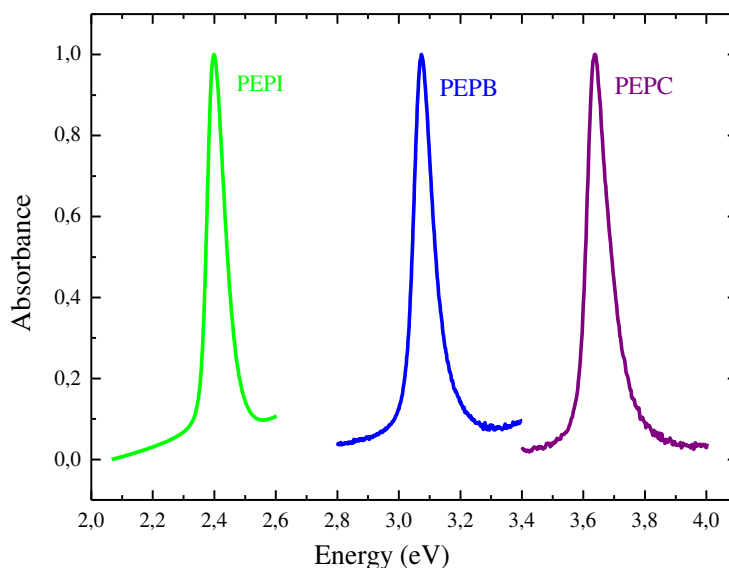
Figure 1.18 OA spectra of PEPI, PEPB and PEPC thin films at room temperature.

To adjust the energy of exciton more finely between PEPC and PEPB, mixed perovskites PEPBr$_{4-x}$Cl$_x$ are synthesized for different values of x (the same work can be also done with PEPI$_{4-x}$Br$_x$). **Figure 1.19a** shows that mixing two kinds of halogens into perovskite doesn't give two excitonic absorption peaks but one absorption peak whose position depends on the proportion of the two kinds of halogen. Moreover, **Figure 1.19b** shows that the excitonic absorption can be continuously tuned by tuning x between 0 and 4. This result provides information about exciton. Henceforth, the continuous dependence of exciton's energy with the

parameter x reveals that the exciton is delocalized enough in the plane layers to be influenced by the presence of both chlorine and bromine.
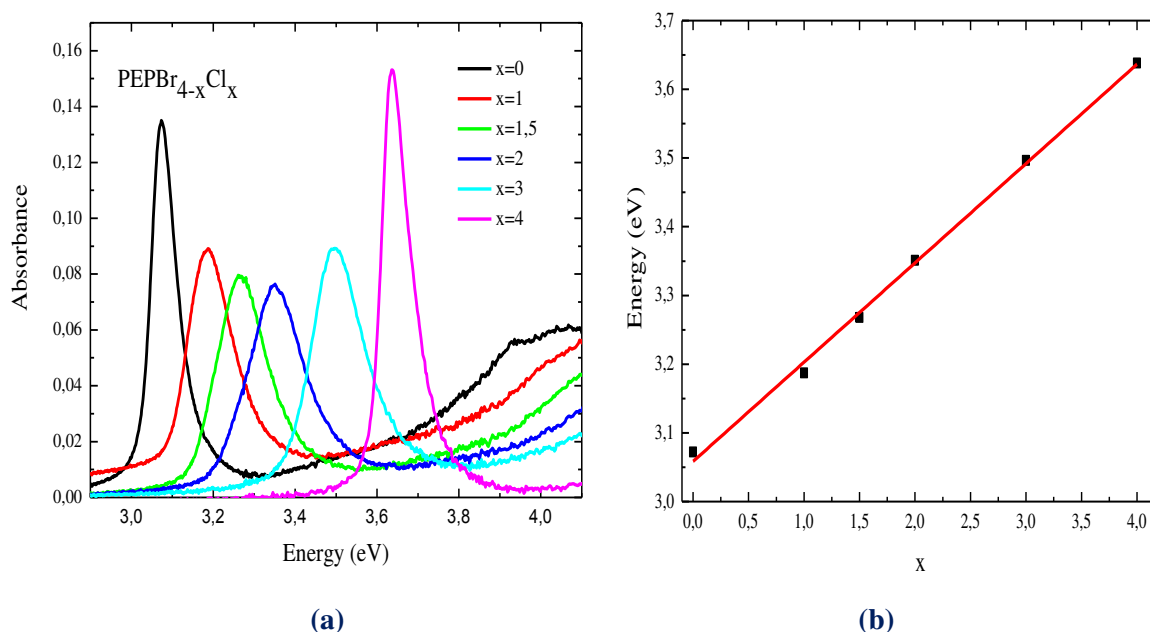
Figure 1.19 Absorption spectrum of the mixed perovskite PEPBr$_{4-x}$Cl$_x$ for x=0 (PEPB), x=1, x=1.5, x=2, x=3 and x=4(PEPC).

Potential Application

Interest in hybrid organic-inorganic perovskites is highlighted in numerous scientific publications. The interesting optical and electrical properties of organic-inorganic perovskites, along with the low cost processing, make them strong potential candidates to be applied to optoelectronic devices such as OILEDs and solar cells. Light emitting devices based on organic-inorganic perovskites have been considered. The layered perovskite compounds are promising for the application to electroluminescent (EL) devices because of very specific optical and electronic properties and flexibility of material design and processability: intense EL from PEPI layer was observed at liquid nitrogen temperature [3]. Further, solar cell is one of the most attractive optoelectronic devices, because of its promising potential to transfer renewable solar energy into electrical energy. The devices using QDs in a liquid-type electrolyte showed the best cell efficiencies, ranging from 3 to 6% [42-44]. For solid-state QD-sensitized solar cells (QDSCs), the device performances were generally poor; only devices made of Sb_2S_3 and PbS QDs attained cell efficiencies approaching around 7% [45, 46]. In contrast, nanocrystalline lead halide perovskites have emerged since 2009 as potential photosensitizers in liquid-type sensitized TiO_2 solar cells [26, 47]. In 2012, the efficiencies of the all-solid-state 3D perovskite solar cells were enhanced to 9.7 and 10.9% using anodes of TiO_2 and Al_2O_3 films, respectively

[27, 48]. In 2013, the performance of a TiO_2 solar cell sensitized with lead iodide perovskite ($CH_3NH_3PbI_3$) was optimized further to attain an overall power conversion efficiency of 15% [49]. Such a striking and rapid progress in the development of organic-inorganic hybrid photovoltaic devices (**Figure 1.20**) indicates the threshold of a new era for a commercialization of all-solid-state mesoscopic solar cells in the near future.
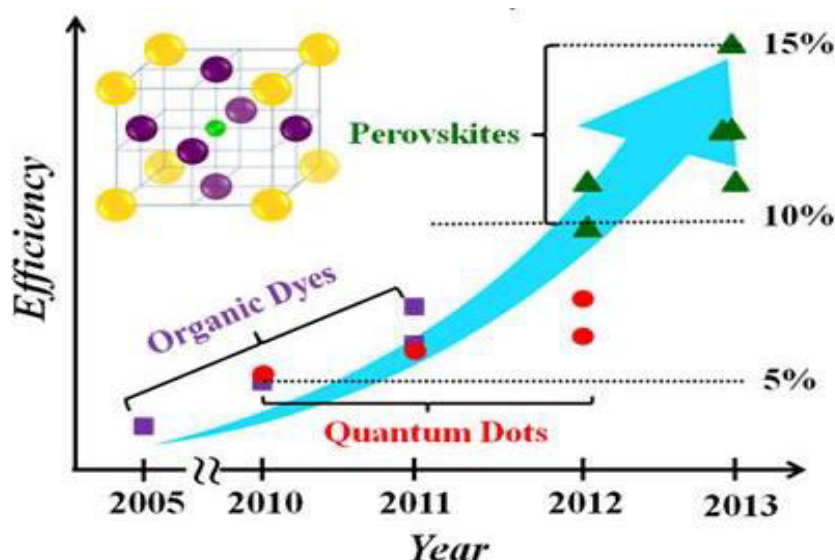
Figure 1.20 Efficiency progressing charts of all-solid-state DSSC, QDSC and perovskite –based SC developed from 2005 to 2013.

Many other applications can be envisioned for the hybrid organic-inorganic perovskites. For the last decade, strong exciton-photon coupling in vertical microcavities has been energetically studied with a view to control the properties of both photons and excitons. When exciton state is strongly coupled to photon states, quasi particles called cavity polaritons are produced. The major feature of the cavity polariton technology centers around large and unique optical nonlinearities which could lead to another class of optical devices such as low threshold polariton lasers. More details on study of light-matter interaction in semiconductor microcavities are presented in the next paragraph. From the point of view of materials, most studies of exciton-photon coupling in such strong coupling cavities focus on devices using inorganic emitters (semiconductor Quantum Dots (QDs) and Quantum Wells) in high Q-factor planar microcavities at low temperatures [5, 6]. However in order to raise the working temperature of these polariton-based devices up to room temperature, alternative semiconductors, presenting large exciton binding energies and oscillator strengths such as GaN [7, 8], ZnO [9], organic [11, 50] and hybrid organic-inorganic material should be employed.

The 2D layered organic-inorganic perovskites, for example $(C_6H_5C_2H_4NH_3)_2PbI_4$, have large exciton binding energies up to 220 meV, which is substantially larger than k_BT at room temperature ($\approx$25 meV). It enables the excitonic effects to be observed at room temperature and therefore it is a good choice as emission center in a microcavity. Recently, strong coupling regime with large Rabi splitting of 100-200 meV has been reported at room temperature in microcavities containing perovskites such as $(C_6H_5C_2H_4NH_3)_2PbI_4$ [14]. These materials can be used alone in a cavity, as well as be combined with another inorganic or organic exciton [16]. In particular, in hybrid cavities containing an inorganic semiconductor and an organic material, it is thought that it is possible to enhance the radiative rate of inorganic excitons and it is hoped that it will be possible to create an electrically driven organic-inorganic laser.

1.7.   Strong Coupling in Semiconductor Microcavities

Light-matter interaction in vertical microcavities, and more particularly the strong coupling regime, has been intensively studied since two decades. In order to increase the coupling between light and matter, it is favorable to increase the spatial overlap between the photonic modes and the matter excitations: the excitons. A typical structure of a semiconductor microcavity (**Figure1.21**) consists of an active medium, like quantum wells or quantum dots or perovskites in our case, sandwiched between two mirrors.

Figure 1.21 Typical structure of semiconductor microcavity.

The study of light-matter interaction is described in Figure 1.22. An exciton, represented by a two-level system ($|1>$, $|2>$), is placed in a cavity, where $|1>$ is the fundamental state of exciton and $|2>$ is the excited state of exciton. This two-level system is coupled to both free space with a coupling strength Ω_{ext} and to the cavity mode with a strength Ω_{mod}. Two types of regime may exist depending on the strengths of coupling Ω_{ext} and Ω_{mod}. If $\Omega_{ext} >> \Omega_{mod}$,

the coupling between the system and cavity mode is described as "weak": when a photon is emitted by the system {|1>; |2>} in the cavity, the probability that it escapes out of the cavity before being reabsorbed is close to 1. If the system is, at t=0, in state |2>, then the probability to find it again in this state at t>0 decreases exponentially with a characteristic time governed by Ω_{mod}, whose value can be obtained by applying Fermi's golden rule. By positioning the energy of the cavity mode more or less in resonance with the energy of transition of the two level systems, it is possible for example to modify the spontaneous emission rate, this effect is known as Purcell effect. When the coupling to the free space is very small compared to the coupling to cavity mode, that is to say when $\Omega_{ext} \ll \Omega_{mod}$, the cavity is in the strong coupling regime. In this case, the reabsorption is stronger and the system is in a dynamic process of absorbing and emitting energy, which is named Rabi oscillations.
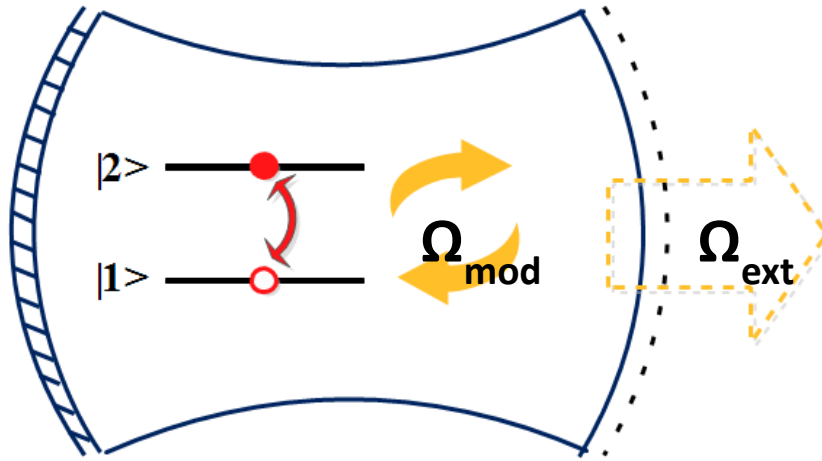
Figure 1.22 Schematic representation of a system consisting of a cavity, and a two-level system. Ω_{ext} and Ω_{mod} are coupling strengths between two-level system with free space and mode cavity respectively.

The strong coupling in microcavities can be treated within quantum mechanics or by a semi-classical model of two coupled oscillators [51]. We consider a microcavity where the two oscillators: photon mode and exciton mode, are in resonance. In a single quantum well structure, the in-plane translational invariance imposes that only excitons and photons of same in-plane wavevector $k_\parallel$ can be coupled. For a given $k_\parallel$, the Hamiltonian of the system is written in the basis of non-coupled states as:

$$H\left(k_\square\right) = \begin{pmatrix} E_{ph}\left(k_\square\right) & V \\ V & E_{ex}\left(k_\square\right) \end{pmatrix}$$

(1.7)

26

Where $E_{ph}(k_{\parallel})$ and $E_{ex}(k_{\parallel})$ are the energies of the photon and exciton modes as a function of $k_{\parallel}$ (dispersion curves). V is the coupling energy between photon and exciton modes. It is supposed to be real and independent from $k_{\parallel}$. The effective mass of excitons is very high compared to that of photons, thus the dispersion of excitons is neglected and we now write E_{ex} instead of $E_{ex}(k_{\parallel})$.

As a result of the coupling term V, the exciton and photon modes cannot be considered as independent eigenmodes of the system anymore. The Hamiltonian $H(k_{\parallel})$ can be diagonalized and the new eigenmodes are a linear and coherent superposition of exciton and photon modes, called "cavity polaritons". The new eigenvalues of $H(k_{\parallel})$ are then found to be:

$$E_{UP}\left(k_{\square}\right) = \frac{E_{ph}\left(k_{\square}\right)+E_{ex}}{2} + \sqrt{\left(\frac{E_{ph}\left(k_{\square}\right)-E_{ex}}{2}\right)^2 + V^2}$$

$$E_{LP}\left(k_{\square}\right) = \frac{E_{ph}\left(k_{\square}\right)+E_{ex}}{2} - \sqrt{\left(\frac{E_{ph}\left(k_{\square}\right)-E_{ex}}{2}\right)^2 + V^2}$$

(1.8)

Where $E_{UP}(k_{\parallel})$ and $E_{LP}(k_{\parallel})$ are the energies of the upper and lower polariton branches (UPB and LPB) respectively. The new photon-exciton mixed states are related to the non-coupled states as followed:

$$\left|E_{UP}\right\rangle = X_k\left|E_{ph}\right\rangle + P_k\left|E_{ex}\right\rangle \tag{1.9}$$

$$\left|E_{LP}\right\rangle = -P_k\left|E_{ph}\right\rangle + X_k\left|E_{ex}\right\rangle \tag{1.10}$$

with,

$$X_k = \sqrt{\frac{\sqrt{4V^2+\left(E_{ph}\left(k_{\square}\right)-E_{ex}\right)^2}+\left(E_{ph}\left(k_{\square}\right)-E_{ex}\right)}{2\sqrt{4V^2+\left(E_{ph}\left(k_{\square}\right)-E_{ex}\right)^2}}} \tag{1.11}$$

and,

$$P_k = \sqrt{\frac{\sqrt{4V^2+\left(E_{ph}\left(k_{\square}\right)-E_{ex}\right)^2}-\left(E_{ph}\left(k_{\square}\right)-E_{ex}\right)}{2\sqrt{4V^2+\left(E_{ph}\left(k_{\square}\right)-E_{ex}\right)^2}}} \tag{1.12}$$

The square modulus values of P_k and X_k: $|P_k|^2$ and $|X_k|^2$ are called Hopfield coefficients and satisfy $|P_k|^2+|X_k|^2 =1$. They correspond respectively to the photonic and excitonic fractions of polaritons.

Figure1.23 shows the dispersion curves of polaritons: the energy position of $\left|E_{LP}\right\rangle$ $\left|E_{LP}\right\rangle$

and $\left|E_{UP}\right\rangle$ $\left|E_{LP}\right\rangle$ $\left|E_{UP}\right\rangle$ states as a function of $k_{\parallel}$ at negative detuning. The detuning is the

energy difference between photon and exciton E_{ph}-E_{ex} at $k_{\parallel}=0$ .The dashed lines represent the

dispersions of uncoupled exciton and photon modes. The lifting of degeneracy caused by

exciton-photon coupling results in the anticrossing of the dispersion curves of upper and lower

polariton branches. At resonance, that is to say when the dispersion curves of both non-coupled

exciton and photon modes intersect, the energy separation reaches its minimum value, called

the Rabi splitting $\hbar\Omega_{rabi}$, which is equal to twice the coupling energy.

$$2V= \hbar\Omega_{rabi}. \tag{1.13}$$

For a negative detuning, the lower polariton branch presents a strong exciton character

at large $k_{\parallel}$, whereas the upper branch presents a strong photon character.
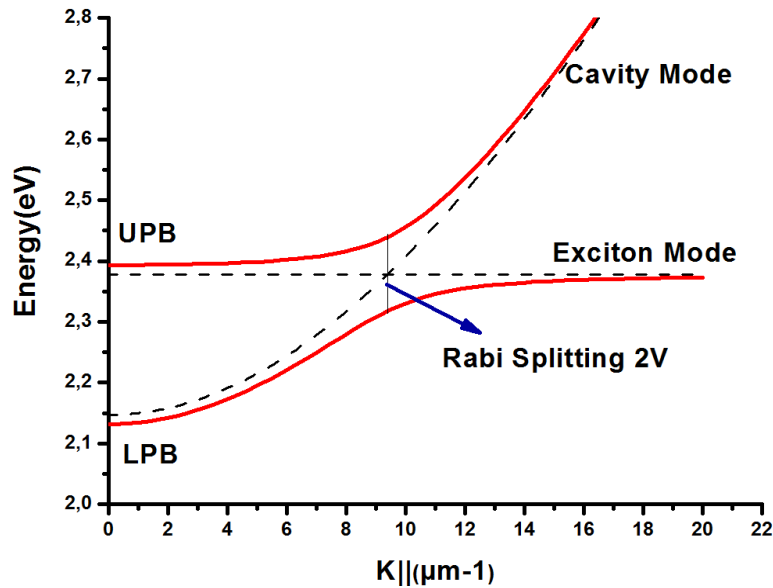
Figure 1.23 The cavity polariton dispersion curves: UPB, Upper polariton branch;
LPB, lower polariton branch. The dispersions of the uncoupled perovskite exciton
and photon modes are also shown by the dashed lines.

The first observation of the strong coupling regime was discovered by C. Weisbuch et

al. in Fabry-Perot cavities containing III-V inorganic semiconductor in 1992 [52]. Soon after,

strong coupling was also found in II-VI semiconductor [53], and later in nitrides [54]. In

molecular materials, the strong coupling has been demonstrated at room temperature with zinc

porphyrin [10], J-aggregates [55], sigma-conjugated polysilane [56], anthracene [57] and

perovskite molecules [32]. These meaningful works, especially the cavities operating at room temperature such as the cavities containing GaN, ZnO and perovskites, provide a good mean to study the coherent and stimulated optical effects which are expected in such confined systems at room temperature and which can lead to realization of new optoelectronic devices such as low threshold polariton lasers [58].

1.8.   Conclusion

2D Hybrid organic-inorganic perovskites have shown to have a self-organized multiple quantum well structure. They are obtained by simple spin-coating of solutions containing all components in the stoichiometric proportions, that is to say, M^{2+}, $4*X^-$ and $2*(R-NH_3)^+$. The thickness of the layer obtained is about a few tens of nanometers and can be adjusted using the concentration of the solutions and parameters of the spin-coating. The position, intensity and shape of the excitonic bands depend on the dimensionality and size of the inorganic network, as well as on the nature of M, X and R groups. When R contains an alkyl- or phenyl-group, the inorganic network of the system behaves as an artificial LD (Low Dimensional) system, in which the organic part plays the role of barrier [59, 60]. This chapter has presented the structural and optical characterization of the perovskites. In addition, the 2D-layered perovskites have shown a great flexibility in their optical properties: the spectral position of the excitonic transitions can be tailored by substituting different halides [39], and the photoluminescence efficiency can be tailored by changing the organic part R [18].

The strong coupling regime between the two-dimensional perovskite exciton and the confined photon modes in a Perot-Fabry microcavity has been explained. This could give the opportunity of using the perovskites in many applications as high-speed emitters, nonlinear optical switches, and polariton lasers.

Chapter2:

2.   Experimental setup and fabrication of microcavities

We have used different techniques in order to study the optical properties of perovskite thin films and of microcavities containing them. We have performed absorption spectroscopy, angle resolved reflectivity spectroscopy, angle-resolved photoluminescence spectroscopy, microphotoluminescence spectroscopy and time resolved pump-probe spectroscopy. Details on the different experimental setups will be presented in this chapter.

2.1.   Absorption

The optical absorbance (OA) spectra of perovskite thin films are measured using a Perkin-Elmer Lambda 950 UV/Vis spectrophotometer at room temperature, it detects the intensity of the light passing through a layer sample: I, and compares it to the intensity of the light before passing the sample: I_0. The optical absorbance OA is thus defined as:

$$OA\ (\lambda) = -\log_{10}(I/I_0) \hspace{3cm} \textbf{(2.1)}$$

The OA spectra are essential for the characterization of perovskite thin layers deposited by spin-coating. It is often the first measurement performed on perovskite thin layers after their preparation, because the analysis of the position and height of the excitonic peak allows verifying the self-organization of perovskite.

2.2.   Angle resolved reflectivity measurement

Angle resolved reflectivity measurement is frequently used as a tool to examine light-matter interaction regime inside the cavity. In fact, the analysis of the absorption spectra of a microcavity can determine whether the coupling is in the strong or weak regime. Generally, it is necessary to acquire both reflectivity R and transmission T spectra to deduce absorption via the relation 1=T+R+A. In the case of cavities, transmission coefficient is negligible compared to reflectivity, so direct access to absorption and thus to the study of strong coupling is provided by measuring R [61]. Moreover, the easiest solution to tune the cavity photon energy mode with respect to that of exciton (considered as dispersionless and so angle-independant) is to vary the angle of incidence on the cavity θ_{ext}:

$$E_{ph}\left(\theta_{ext}\right) = \frac{E_0}{\sqrt{1-\left(\dfrac{\sin\theta_{ext}}{n_{cav}}\right)^2}}$$
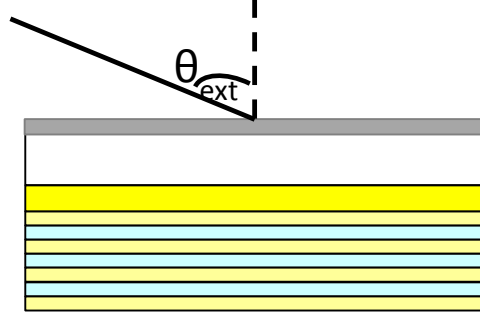
where E_0 is the photon mode at normal incidence ($\theta_{ext} = 0$) and n_{eff} is the effective refractive index of the entire cavity.

Figure 2.1 show schematically the experimental setup used to achieve angle-resolved reflectivity measurement. Xenon lamp is used as excitation source with broad white light emission from 280 nm to 780 nm. Its output light is filtered by SpectraPro-2150i monochromator (Princeton Instruments, Acton^{TM}) and then is collimated by a f = 50.2 mm focusing lens. The beam is mechanically chopped at about 720 Hz in order to overcome the low frequency noise. A part of the beam is reflected by a piece of glass in order to record $I_{r0}(\lambda)$ by PMT1 (PMT = Photomultiplier), while the other part is transmitted and is recorded as $I_{s0}(\lambda)$ by PMT2. Then, the cavity sample is fixed in the center of a rotating plate and the PMT2 is moved to the $2\theta_{ext}$ direction to collect the reflected beam from the cavity sample. In this configuration, the signal of the two PMTs are recorded as $I_{r1}(\lambda)$ and $I_{s1}(\lambda)$. The incident angle θ_{ext} is varied by rotating the plate, and positions of PMT2 are accordingly adjusted to collect the reflection signal. The reflectivity signal R is then given by:

$$R\left(\lambda\right) = \frac{I_{s1}}{I_{s0}}\frac{I_{r0}}{I_{r1}} \tag{2.2}$$

This two PMTs configuration allows to overcome the fluctuations of the incident Xenon lamp source.
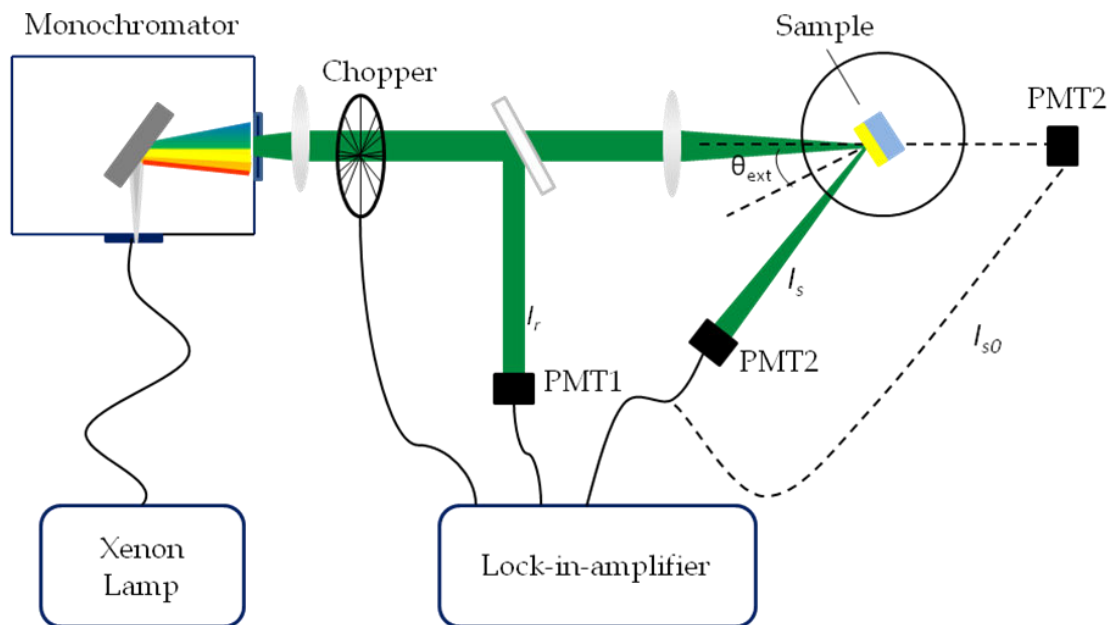
Figure 2.1 Angle-resolved reflectivity experimental setup.

2.3. Angle-resolved photoluminescence

Photoluminescence (PL) is one of the most remarkable properties of 2D layered perovskites. Most 2D layered perovskites mainly dissipate energy by efficient spontaneous emission after being promoted to an excited state by absorbing photons. Different light sources are used as excitation sources. In **Figure 2.2**, a 405 nm laser diode is sent under normal incidence to the sample. Photons are emitted from the sample in all directions in space as they are generated by spontaneous emission. A lens is placed such that it collects photons emitted in a solid angle based on the half-cone angle θ, centered at the optical axis. The photons are then collected by a SpectraPro 2500i spectrometer, coupled to a PIXIS:100B (Ropers Scientific) CCD camera.
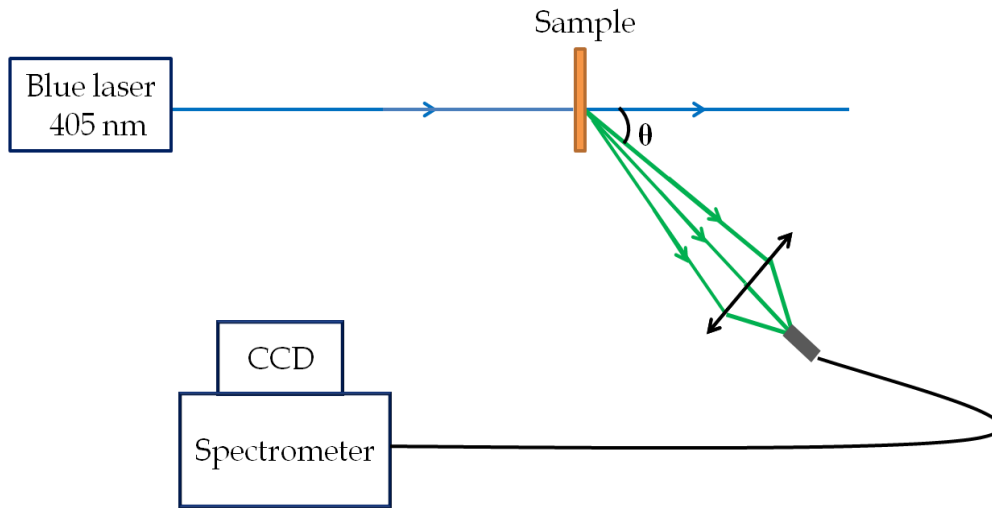
Figure 2.2 Experimental setup used to measure PL using blue laser at λ=405nm.

2.4. Micro-photoluminescence

The micro-PL system is an integrated system designed for micro-photoluminescence studies. Micro-photoluminescence (μPL) is a technique especially suited for characterization of very small structures. The principle behind the technique is the same as for conventional PL, but a microscope objective is placed between the excitation laser and the sample. The purpose of the objective is to focus the laser into a very small spot size to localize excitation to specific regions of the sample. In our setup, the laser is focused onto a 1.5 μm spot diameter [62]. This allows spatial resolution of the order of several micrometers, which is crucial for semiconductor samples containing multiple µm-scale structures [63].

2.4.1. Micro-photoluminescence in Confocal Geometry

A confocal setup has been developed to provide high efficiency of the laser injection combined with a versatile detection to measure the energy of light emitted by the sample in either real or momentum space.

Two kinds of lasers (**Figure 2.3**) have been used in this thesis:

- continuous wave (CW) lasers of wavelengths 405 nm and 473 nm
- a femtosecond (fs) laser of wavelength 405 nm or 440 nm. The two wavelengths are obtained from Ti-sapphire oscillator producing 120 fs pulses at 800 nm with 1 khz repetition rate followed by an optical parametric amplifier

In fact, a pulsed laser has the advantage to produce high peak power compared to a laser in a continuous intensity mode. This high peak power is a key parameter to inject a large number of carriers in a small amount of time and, therefore, to reach the non-linear regime in organic semiconductor structures. The low repetition rate of 1 kHz is favorable to limit the photobleaching of the perovskites.

After fixing the laser used at the beginning of the injection line, the laser beam, as photo-excitation source, reaches the sample surface through a microscope. The latter is constituted with objective lens having a numerical aperture (NA) =0.55, corresponding to a focused laser spot diameter of about 2 μm. The luminescence emitted by the sample is collected by the same objective lens and passes through an achromatic 50:50 beam splitter (BS). The beam splitter sends a part of the incident laser to the powermeter. The PL signal is directed through the entrance of SpectraPro 2500i spectrometer (Princeton Instrument Company) having a 1200 lines/mm grating blazed at 300 nm. Then, the PL signal is collected using a thermoelectrically cooled CCD camera (PIXIS 256, Princeton Instruments). The spectrometer and camera were controlled by proprietary software (WinSpec, Princeton Instruments).
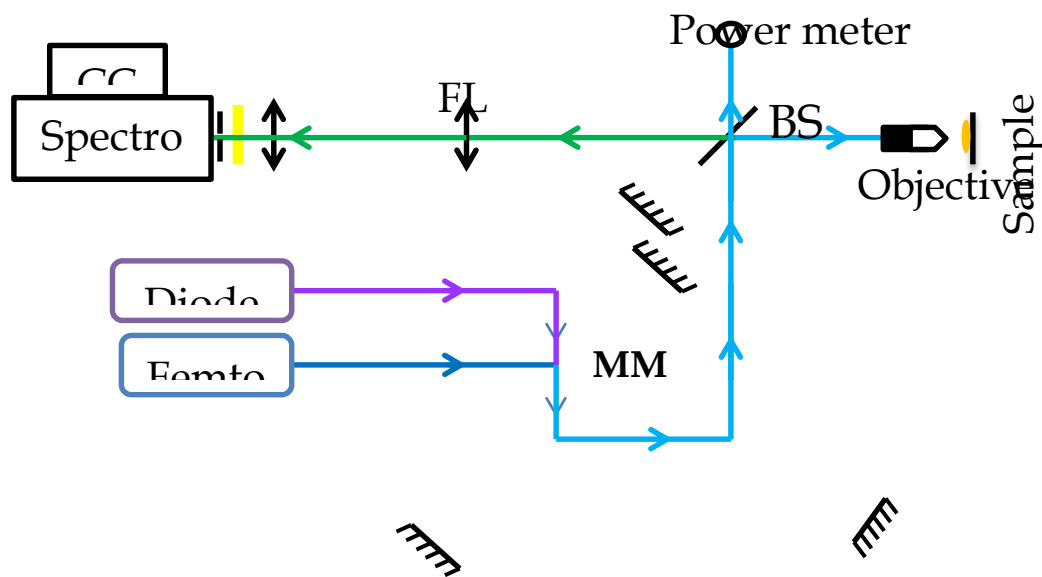
Figure 2.3 Micro-photoluminescence experimental setup.

A λ/2 blade along with a polarizer is placed in the path of the laser in order to change the power of the beam excitation. A powermeter is placed to measure the power of the incident beam directed to the sample and a yellow filter is placed at the entrance of spectrometer as shown in the **Figure 2.3**. The yellow filter is used to block reflections from laser light and allows only the sample's emitted light to pass.

Moreover, this experimental setup is designed to give an image of the surface of the sample on the detector in the real space configuration or of its Fourier plane in the reciprocal space configuration. It is possible to switch from real to Fourier space spectroscopy by adding a Fourier plane lens (FL) as shown in **Figure 2.3**. The FL is placed on a movable mount that moves forward when switching from real to Fourier space spectroscopy and backward when switching from Fourier to real space spectroscopy. Finally, this set-up allows to quickly measure the energy of light with either spatial or momentum resolution (see next paragraph).

2.4.2.   Microphotoluminescence experiment using Fourier Imaging

The basic principle of Fourier imaging is explained in **Figure 2.4**. Fourier space of a given object is situated at the focal length after the lens. In the configuration presented on **Figure 2.4**, where the real space and the Fourier space are situated, respectively, at a focal length before and after the lens, the light collected in the Fourier space is the exact Fourier transform of the light emitted from the real space. This statement is limited to the paraxial approximation which can be considered as valid up to 30°. As shown in **Figure 2.4**, Fourier space is a direct image of the light emission from the object. Indeed, a given angle of emission α corresponds only to one position in the Fourier space at f.tan(α) from the optical axis. Therefore, one can optically use the signal in this Fourier plane to measure the dispersion relations directly on a detector.

Figure 2.4 Principle of an angular resolved experiment using Fourier space imaging. α is the angle of emission of a photon.

Micro-photoluminescence measurements were performed on different kinds of samples: perovskite thin layers and perovskite based microcavities. Results of these measurements will be shown through the manuscript.
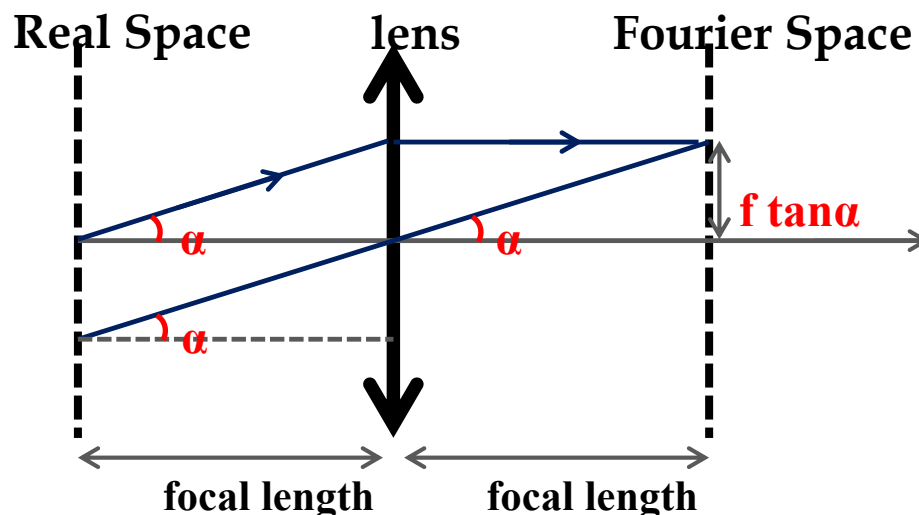
2.5. Dynamic study by pump-probe measurement

Pump-probe spectroscopy investigates the fast transient dynamics of optically excited carriers. More precisely, it measures the carrier population dynamics. By using a strong pump pulse and a weaker probe pulse, the transient changes in the optical properties induced by the pump are recorded as a function of time with a very high temporal resolution. Pump-probe spectroscopy is a well-established technique, which has been widely applied to semiconductors, highly correlated systems and other condensed matter samples.

In this section, we present the pump-probe experimental setup mounted at LAC – ENS Cachan which allows the time resolved optical characterization of perovskite thin films, and the preliminary studies necessary for acquiring temporal and spectral pump-probe measurements.

2.5.1. Time-resolved optical characterization

In the following, we will introduce the pump-probe experimental setup mounted at LAC – ENS Cachan which allows the time resolved optical characterization of perovskite thin films.

2.5.2. Principle of Measurement

With the advent of ultra short pulse laser in the late 1980s, it was possible to determine the dynamics of spectral variations by pump-probe measurement [64, 65]. This technique uses a short optical excitation pulse (the pump) to generate a nonequilibrium charge carrier distribution in the sample. A second weaker and synchronous optical pulse (the probe) is then used to interrogate the pump-induced changes of the optical properties of the sample. These changes (i.e. changes in absorption coefficient) are directly dependent upon the optically generated excess carrier density. The transmission of the probe through the sample is monitored and the density-dependent change in absorption coefficient provides the change in optical properties. By delaying the arrival time of the probe relative to the pump, the excess carriers have time to recombine and/or diffuse before being interrogated. Measuring the change in transmission of the probe at increased time delays allows an access to the time-resolved relaxation of the excited carriers back to equilibrium. A typical ultrafast pump-probe experiment is illustrated in **Figure 2.5**.
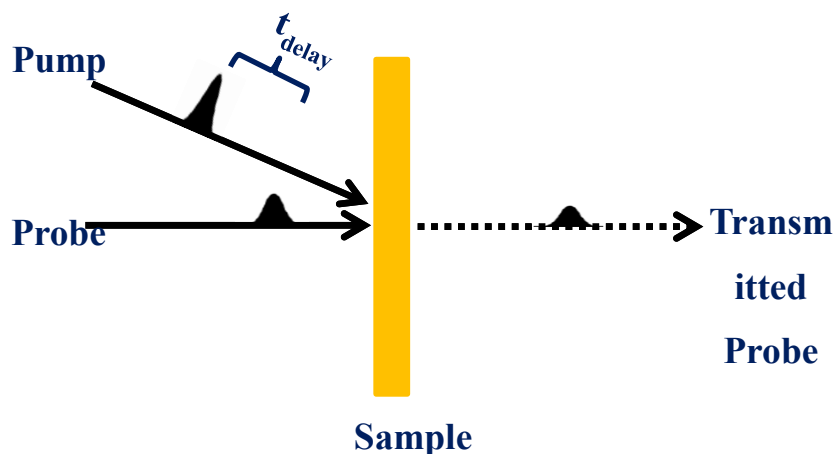
Figure 2.5: Illustration of typical ultrafast pump-probe experiment.

The pump-probe experimental setup implemented at LAC – ENS Cachan before this thesis and optimized during this thesis is presented in details in the following paragraph.

2.5.3. Pump-probe experimental setup

Figure 2.6 shows the schematic diagram of the synchronized, two color pump-probe fs system used during this thesis. Seed pulses of the laser system are generated by Hurricane laser system designed and made by Spectra Physics. The output of the laser system was set to work at 1 kHz repetition rate, providing pulses of duration between 80 and 120 fs. The output beam centered at about 800 nm is directed towards the input of an optical parametric amplifier OPA-800C designed and made also by Spectra Physics. The OPA divides the laser pulse into two beams: one is used as the pump beam and the other beam, much weaker, is used as the probe. The pump pulse corresponds to the fourth harmonic of the OPA and can be tuned from 2.81 eV (above the 2D continuum step) to 2.397 eV (exciton resonance). The probe consists of a spectrally broad pulse obtained by self-phase modulation in the sapphire crystal of the OPA. The pump beam was passed through a fixed optical path and then focused to the sample. Variable density is placed in the path of the pump beam to adjust the power of the excitation used. The probe beam was passed through an optical delay line, which is a reflective optics consisting of two perpendicular flat mirrors mounted on a computer-controlled motorized translational stage. With 0.1 μm accuracy, such a translation achieves a time resolution of 0.66 fs, which demonstrates that it is not the main limitation of the time resolution in a pump-probe setup. This optical delay line was designed and made by Newport. Following different optical paths, the pump and probe beams are then directed and focused on the same spatial area of the sample, with the help of an imaging system composed of a periscope and a webcam. After

transmission through the sample, the probe beam is directed through the entrance of SpectraPro 2150i Monochromator (Princeton Instrument Company/Acton) having a 300 lines/mm grating blazed at 500 nm. A photomultiplier (H9307-03, Hamamatsu) was placed at the output of the monochromator to collect the probe beam.

The value to extract from a transmission-based pump-probe measurement is the relative increase or decrease in transmission of the probe that occurs when excess carriers are present compared to when they are not. The method used here is referred to as time-resolved differential transmission (ΔT/T). This technique compares the transmission of the probe pulse in the absence of pump pulse (i.e. the equilibrium transmission) to the transmission of the probe pulse in the presence of pump pulse (i.e. the transmission when excess carriers are present) and is expressed as,

$$\Delta T / T = \frac{T_{on} - T_{off}}{T_{off}} \tag{2.3}$$

where T_{on} and T_{off} are the transmission of the probe through the sample in the presence and absence of pump pulse, respectively. ΔT/T is generally quite low, of the order of one percent or less, and so an optical chopper is placed in the path of the pump beam and modulates the pump pulse series at a frequency of about 117 Hz. The synchronized signal from the chopper and the output signal from the photomultiplier are transmitted to Lock-In Amplifier synchronous detection (SR830 DSP, Stanford Research Systems[TM]). The synchronous detection delivers a voltage image of the difference ΔT signal.

A computer associated with specially designed software under Labwindow, allows measuring the voltage from the synchronous detection. The optical chopper is mounted on a rail so that it can also be placed on the path of the probe beam in order to make the acquisition of the transmitted signal T of the probe in the absence of the pump. This allows forming ΔT/T, the only quantity that can be related to the populations of excitons and electron-hole pairs. As this computer controls the delay line and the monochromator, it allows recording ΔT/T as function of time and wavelength.

The pump and probe beams are generally polarized in the vertical plane of the experimental setup. The pump and the probe beams are made cross-polarized, thanks to a half-wave plate, in order to reject as much as possible the scattered pump signal. For that, a polarizer having a polarization direction parallel to the probe polarization is placed at the input of the monochromator.
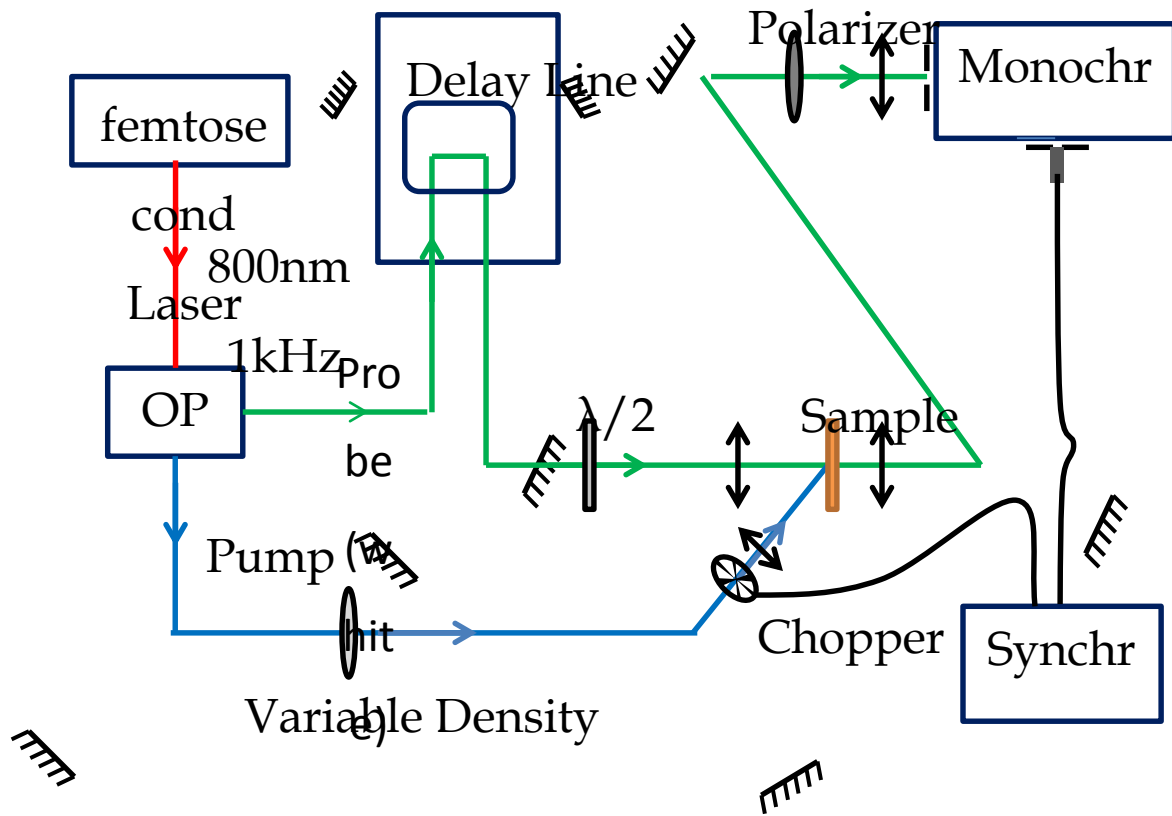
Figure 2.6 Schematic diagram of the synchronized two color pump-probe fs system.

Using pump-probe experimental setup, several measurements were performed for both perovskite thin films and microcavities. However, most of the work was concentrated on perovskite thin films.

2.5.4. Cross Correlation

The shape of pump-probe traces depends on the relaxation properties of excitons and electron-hole pairs of the studied sample on one hand and on the temporal envelopes of both pump and probe pulses on the other hand. More specifically, this shape is a result of time convolution between pump pulse, probe pulse and the impulse response of the material concerned. This relation can be described as:

$$S(t) = (CC \otimes R)(t) \tag{2.4}$$

where S (t) is the time trace signal resulting from pump-probe measurement, R (t) is the impulse response of the studied sample, and CC (t) corresponds to the pump-probe cross-correlation function, that is to say the convolution product between the temporal envelopes of

both pump and probe pulses. The cross correlation is closely related to the temporal resolution of pump-probe system since the characteristic times below the temporal extension cannot be resolved in the study of temporal traces.

Information about relaxation properties of excitons and electron-hole pairs are found only in the impulse response function R (t). To extract this information from the obtained time traces, it is then necessary to make an adjustment of the relaxation model (mono or bi-exponential) taking into account the pump-probe cross-correlation function CC (t). The temporal width of CC (t) is considered as a fitting parameter of these models since it may slightly vary depending on the laser pulse and OPA's setting.

To avoid interpretation errors during extracting the time characteristics of the temporal traces, it is necessary to have an approached value of this parameter. This is achieved by acquiring a temporal trace associated with pump-probe signal that presents a very short characteristic time in comparison to the temporal width of the cross correlation CC(t) which we try to determine. In this case, the impulse response of the physical phenomenon can be treated as a Dirac impulse, and then the time trace S (t) is identified with the cross-correlation CC (t). The physical phenomenon used here is the amplification of the probe pulse by stimulated Raman scattering.

The amplification of the probe pulse by stimulated Raman scattering is described in details in the references [66, 67]. It is generated if at least two photons, the pump and the probe photons, coincide in time and space inside the medium. Emission of a third photon can be stimulated provided that the energy of each of the incident photons differs by an amount E_v corresponding to the molecular oscillation energy specific of the medium. This amplification of the probe pulse in the temporal trace is signed by a positive pump-probe signal (that is to say in phase with the synchronizing signal of the optical chopper) which reproduces the temporal profile of the cross-correlation.

The evolution of the temporal width of the cross-correlation was conducted using the Raman scattering of water for which $E_v = 422$ meV. Therefore to obtain an amplification of the probe by stimulated Raman scattering, the pump must be placed at 2.4 ± 0.422 eV. Due to practical reasons related to the use of the OPA, we choose to place the pump at 2.822 eV which corresponds to 440 nm.

For the cross-correlation adjustment, the temporal envelopes of the two pulses are assumed to have Gaussian shape. This implies that the cross-correlation is also Gaussian. The adjustment of the Gaussian to the positive part of the experimental time trace led to the red

solid line in **Figure 2.7**. Despite the signal to noise ratio, the agreement between the Gaussian model and the cross-correlation obtained experimentally is quite satisfactory. The width at half maximum of the Gaussian fit is 112 fs. This value is taken, subsequently, as a fixed parameter to verify the appropriateness of the adjustment relaxation models.
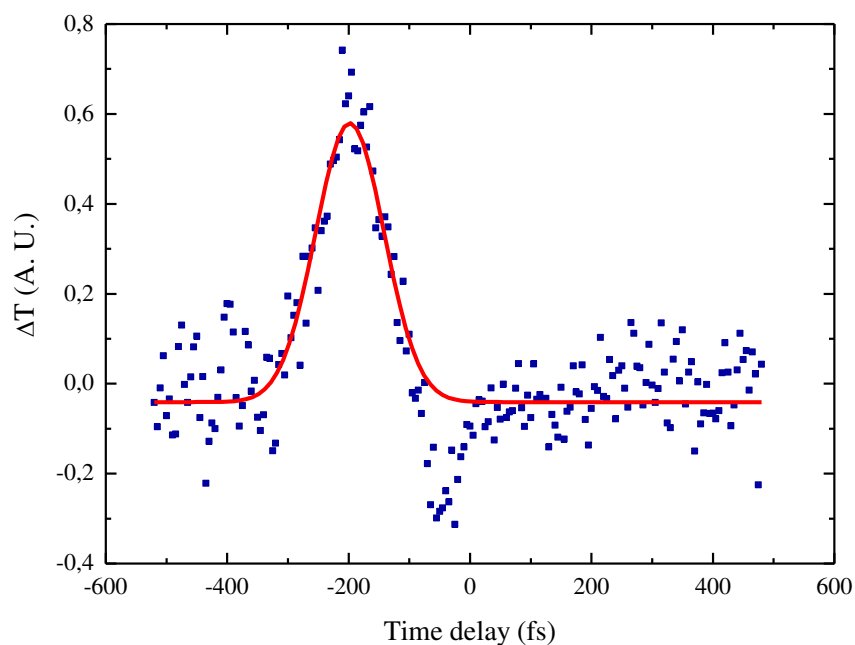
Figure 2.7 Time trace corresponding to the amplification of the probe pulse (517 nm) by stimulated Raman scattering in water: the monochromator is set at 517 nm and the wavelength of the pump is 440 nm.

Determination of the time resolution and the "zero time" dispersion

The position of the delay line corresponding to the superposition time between the pump and probe pulses is called "zero". Due to the dispersive nature of the materials used to design optical elements (lenses, filters, densities, etc...) traversed by the probe pulse, the "zero" depends on the probe wavelength λ_s selected by the monochromator. Indeed, the index of these materials vary depending on the wavelengths considered and then probe pulses having different wavelengths do not propagate at the same speed.

The software controlling the acquisition of the spectra $\Delta T/T$ should be able to compensate for this "zero" to maintain the pump-probe delay constant during the acquisition of a spectrum. To do this, we use the effect of cross-phase modulation in water, observed on the temporal trace of **Figure 2.7**, which unlike the stimulated Raman amplification, occurs whatever the energy difference between the pump and the probe is.

Cross-phase modulation (XPM) generated in the liquid phase using pump probe technique has been reported by several authors [68-71]. It is a non-linear process where a transient modification of the optical index of the sample occurs when pump pulse passes through it: Kerr effect. This modification of the refractive index affects the probe pulse, which is temporally and spatially superimposed with the pump pulse. It modifies the frequency distribution of the photons that constitute the probe pulse. A comprehensive and rigorous description of this phenomenon is given by Lorenc et al. [66]. **Figure 2.8** below shows an example of pump-probe time trace corresponding to an effect of cross-phase modulation occurring in water. This trace is consistent with the expected time signature [66].
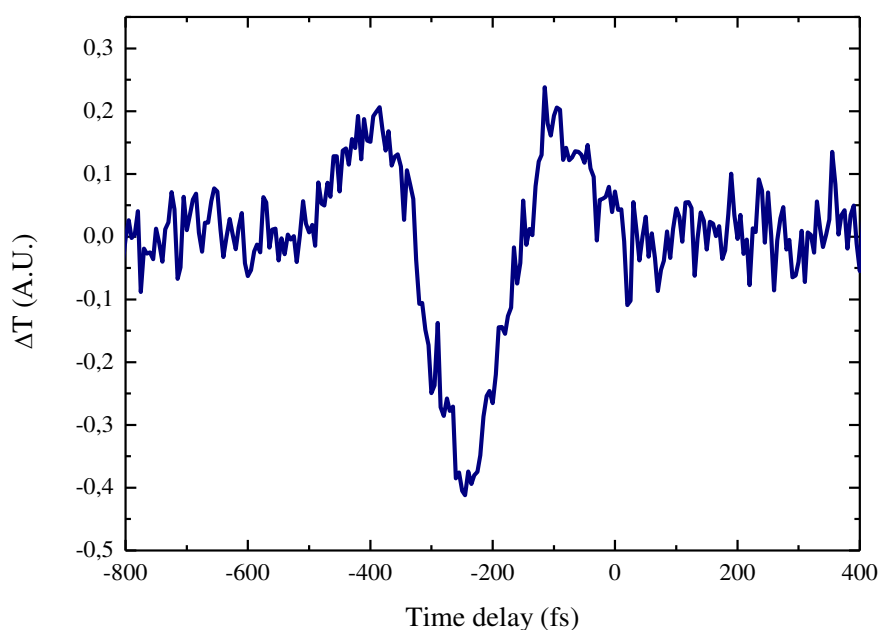
Figure 2.8 Pump-probe time trace measurement corresponding to cross phase modulation occurring in water. The pump wavelength is set at 440 nm, the probe wavelength is set at 505 nm.

Pump-probe time traces with the signature of the cross-phase modulation of water were recorded for different wavelengths λ_s covering a range from 460 to 600 nm. The pump wavelength λ_p remains set for this part at 440 nm. **Figure 2.9 a)** shows the traces obtained for λ_s between 501 and 519 nm. The temporal positions of the signature of the cross-phase modulation are plotted on the graph in **Figure 2.9 b)** (blue squares).

(a)   **(b)**
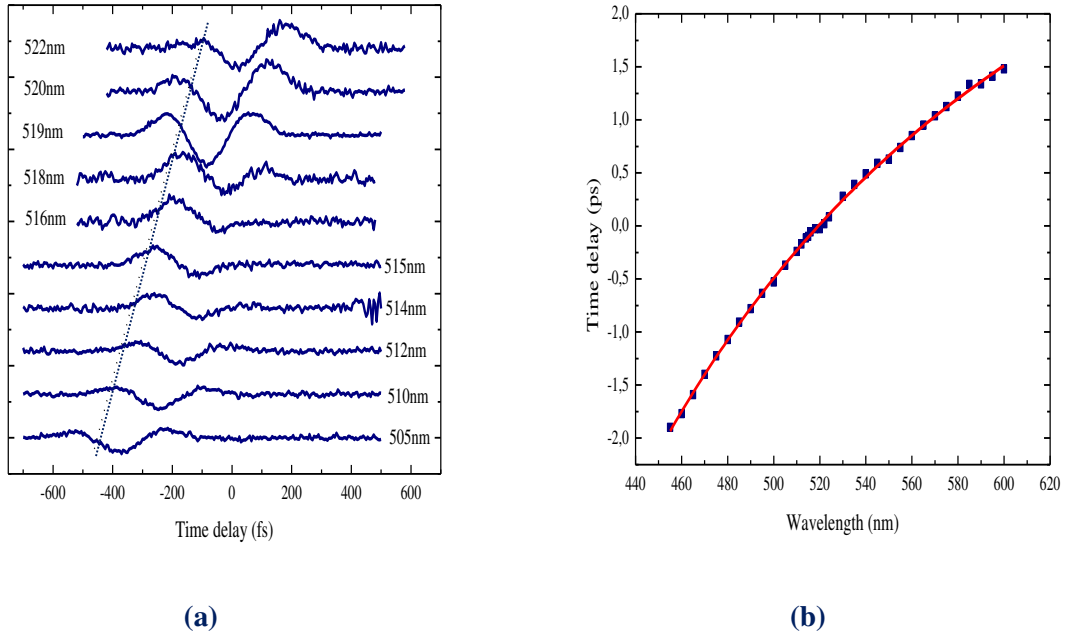
Figure 2.9 a) Pump-probe time traces showing the signature of the cross phase modulation occurring in water obtained for different values of λ_s. The pump wavelength λ_P is set at 440 nm. **b)** Temporal positions (blue squares) of the signature of cross phase modulation plotted as a function of λ_s. The red curve corresponds to the fit with the model described in the text.

Let Δt be the offset of "zero" generated by the passage from a reference wavelength $\lambda_{s,0}$ to another wavelength λ_s. Assuming that probe passes through different dispersive optical elements made with the same material, this offset is written as:

$$\Delta t = \frac{L}{c}\left(n\left(\lambda_{s,0}\right) - n\left(\lambda_s\right)\right) \tag{2.5}$$

with c, the speed of light, L the thickness of dispersive material, and $n(\lambda)$ its optical index at wavelength λ. Referring to Cauchy's law which gives a good approximation for the index variations of transparent materials in the visible range, we can write:

$$n\left(\lambda\right) \cong n_0 + \frac{A}{\lambda^2} + \frac{B}{\lambda^4} \tag{2.6}$$

with n_0, A and B, three constants dependent on the material considered. The offset Δt is then:

$$\Delta t = A'\left(\frac{1}{\lambda_{s,0}^2} - \frac{1}{\lambda_s^2}\right) + B'\left(\frac{1}{\lambda_{s,0}^4} - \frac{1}{\lambda_s^4}\right) \tag{2.7}$$

The constants A' and B' are taken as adjustment variables of the offset term measured via the cross-phase modulation of water as a function of λ_s. The red curve in **Figure 2.9 b)**

corresponds to the adjustment made with A'= 1.31799 x10^9 (fs.nm^2) and B'= 4.73669x10^{13}(fs.nm^4). The mathematical expression of the shift of "zero" thus obtained is programmed in the acquisition software of spectra ΔT/ T to allow its compensation via the displacement of the delay line.

2.6. Standard Microcavity

A.Bréhier and G.Lanty [13, 32] have developed during their thesis at LPQM - ENS Cachan the method of fabricating and optimizing a perovskite-based microcavity (Standard microcavity) working in strong coupling regime. It is composed of a PEPI thin film (50 nm) sandwiched between two mirrors, a dielectric Bragg mirror DBR (bottom mirror) and a silver mirror (top mirror) as illustrated in the **Figure 2.10**. The PMMA layer is a spacer layer, optically non active, necessary to tune the wavelength of the photon modes. In particular, we choose to work with λ/2-cavities in which only one photon mode is present. To observe the strong-coupling regime, we will tune the wavelength of the photon mode close to the wavelength of the perovskite exciton mode.
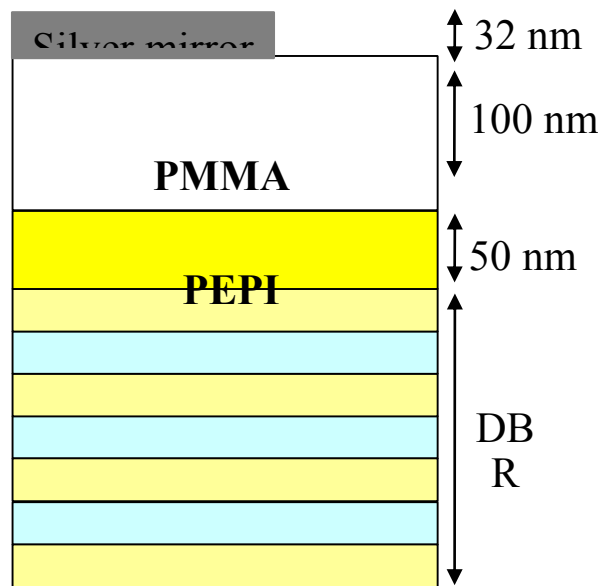

Figure 2.10 Standard Microcavity Structure.

In order to enter the physics of microcavities, I have learnt the technique of fabrication of standard microcavity. In the following, a complete description of each stage of fabrication of such microcavity will be presented.

2.6.1. Bottom Mirror: Dielectric Bragg mirror (DBR)

Bragg mirror (also called dielectric mirror, or Distributed Bragg Reflector DBR) is involved in the fabrication of standard microcavity. It is composed of multiple thin layers of two different materials, one with low refractive index n_L and another with high refractive index n_H. **Figure 2.11** shows schematically the structure of a Bragg mirror. At each interface between different materials, there is a partial reflection of the optical wave. A dielectric Bragg mirror is able to reflect an incident wave of wavelength λ_0 in vacuum if the widths of the layers meet the Bragg conditions: the optical path associated with each layer must be equal to $\lambda_0/4$ such that $n_H L_H = n_L L_L = \lambda_0/4$ with L_H (L_L) the length of the layer of index n_H (n_L).
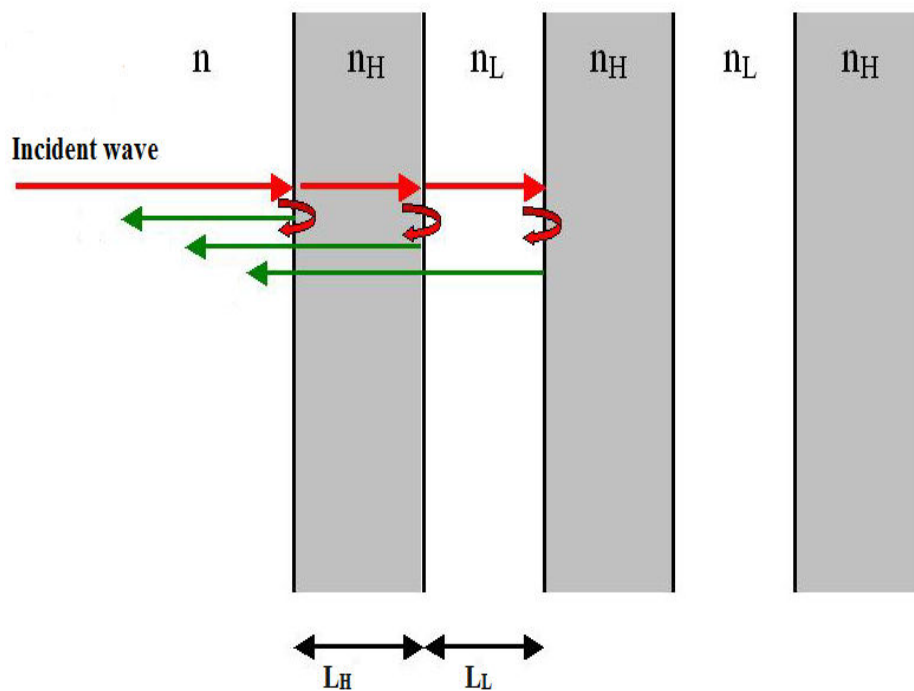
Figure 2.11 Dielectric mirror Structure

If the refractive index difference between the two dielectric materials is relatively small, a large number of pairs N are needed to achieve a high reflectivity. Dielectric mirror can provide high reflectivity over a region called the "stop-band", whose width $\Delta\lambda$ is approximately given by:

$$\Delta\lambda = \frac{2\lambda\left(n_H - n_L\right)}{\pi n_{eff}}$$

(2.8)

where n_{eff} is the effective refractive index of the dielectric mirror. The stop-band is the region in which the condition $n_H L_H = n_L L_L = \lambda_0/4$ is satisfied. It is clear that a small refractive

index contrast results in a narrow stop-band. Moreover, the width of the stop-band is independent of the number of layers, it depends only on the refractive index difference between the layers of the stack. The value of the reflectivity of the mirror is limited by the absorption in the dielectric materials.

The dielectric mirror used in the fabrication of perovskite based cavities is made by Layertec ^{TM} Company. They come in round pellet form of diameter 12.7 mm and thickness 1 mm thick. The structure of the dielectric Bragg mirror proposed by Layertec TM Company is shown in **Figure 2.12**. The Bragg mirror is deposited onto a fused silica substrate by Plasma Enhanced Chemical Vapor Deposition (PECVD). It is formed of 6.5 pairs of two different layers with $n_H = 2.36$ and $n_L = 1.46$. A 10 nm thick silica layer is deposited on the top of the mirror to ensure a good deposit of the self-organized perovskite.

(a)   (b)
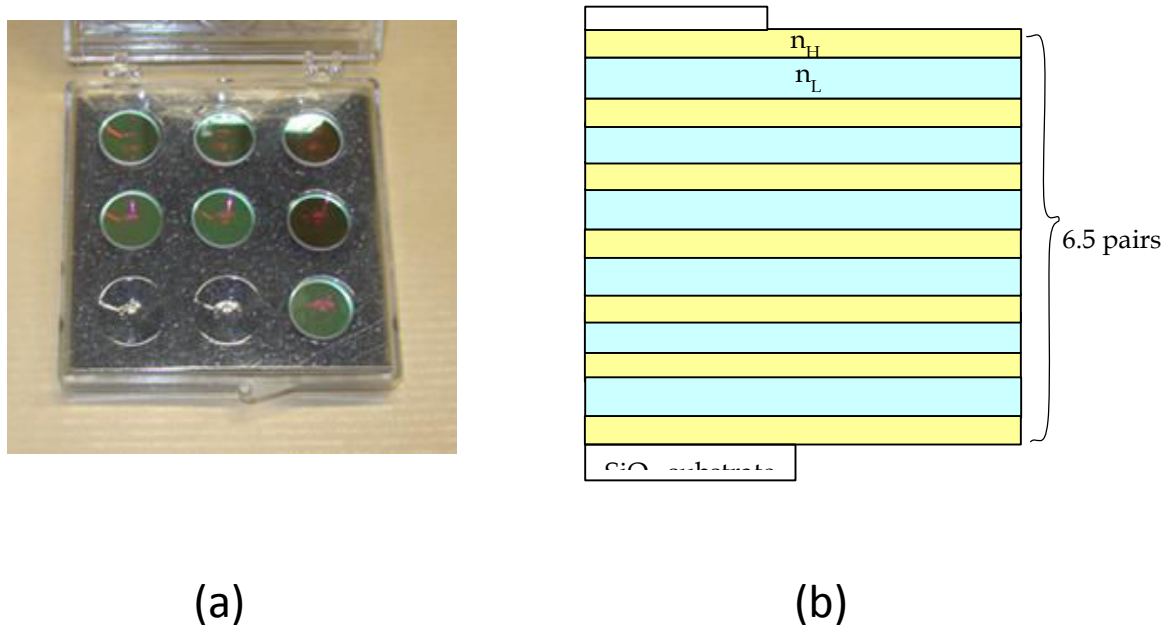
Figure 2.12 (a) Photograph of the dielectric mirrors in their box. **(b)** Structure of the Layertec^{TM} Society Bragg mirror used for the development of PEPI based cavities.

Figure 2.13 presents an example of the reflectivity spectrum of the dielectric Bragg mirrors prepared by Layertec^{TM} company. This spectrum was obtained using the experimental setup which measures the Reflectivity spectrum of the mirror at normal incidence. We can see that the stop band of the mirror at normal incidence is centered at 2.43 eV, having a maximal reflectivity of 98% and the stop band extends from 2.18 eV to 2.7 eV (that is to say from 460 nm to 570 nm). The two dips at 1.88 eV and 2.95 eV are the Bragg modes of this DBR mirror.
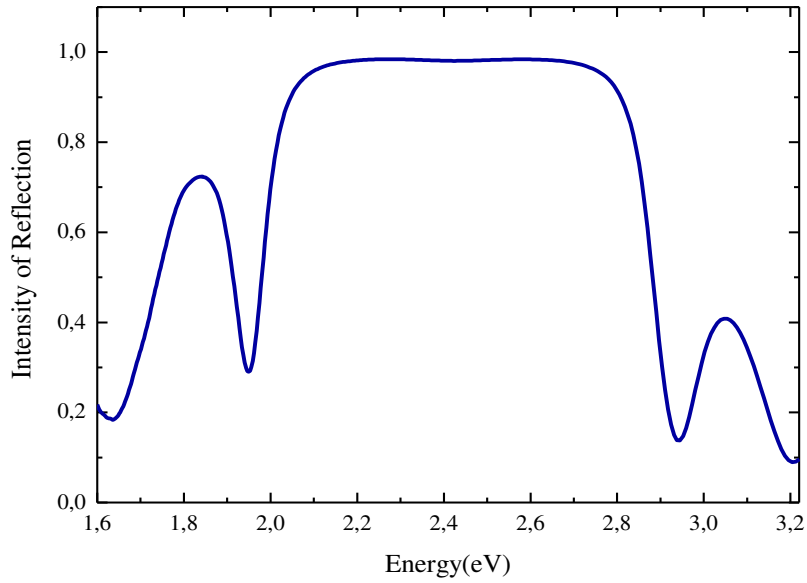
Figure 2.13 Reflectivity spectrum of the dielectric Bragg mirror at normal incidence.

The reflectivity spectra for the incident angles 0°, 20°, 30°, and 40° are exhibited in **Figure 2.14**. We note that the reflectivity spectrum shifts to higher energy as the angle of incidence increases.
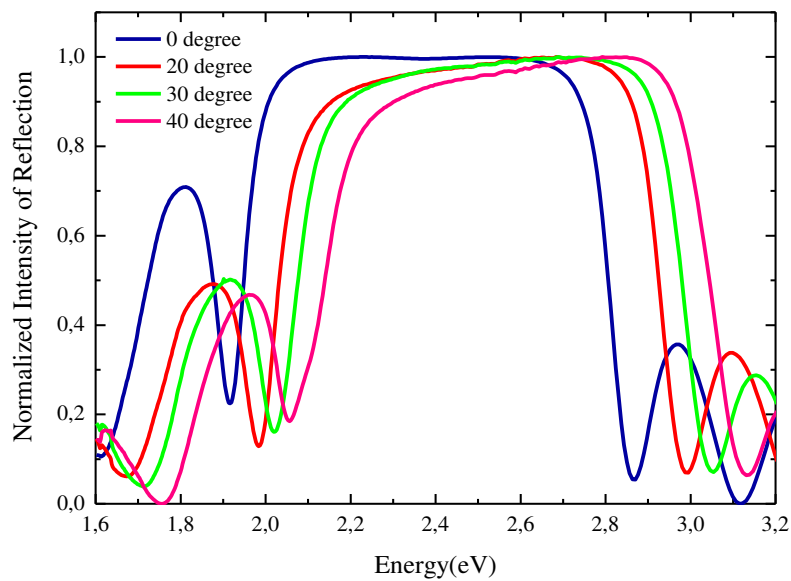
Figure 2.14 Reflectivity spectra of the dielectric Bragg mirror at the angles of incidence 0°, 20°, 30°, and 40°.

2.6.2. Top mirror: Metallic mirror

The top mirror of the Standard cavities is a metallic mirror deposited in the clean room of Institut d'Alembert at ENS-Cachan. It is deposited on the top of the spacer layer by

electrobeam evaporation. For mirrors used in the visible range (near the exciton energy of PEPI, at 2.4 eV), several metals can be used such as: aluminum, silver, gold and platinum. However silver mirror has been chosen as the top mirror used in the fabrication of standard microcavity since its reflectivity coefficient is very good (around 80%) for energies below 3 eV, which is well suited to the production of PEPI based microcavities [20]. In addition, the deposition of silver by evaporation does not raise any difficulties in contrast to that of aluminum and platinum [20]. A schematic diagram of the self evaporation frame is represented in **Figure 2.15**. First, the sample is placed in a high-vacuum chamber that also contains, in a crucible below the sample, the metal to be deposited (Silver metal in our case). An electric current is applied to the crucible which is heated to a certain temperature (by Joule effect) leading to the liquefaction of the metal and the release of metal atoms into the chamber along straight paths as shown in **Figure 2.15**. Some of these atoms are deposited on the sample up to a thickness controlled by a piezoelectric balance. The control of the thickness is very important because the transmission and reflection coefficients of the metallic mirrors depend sensitively on this thickness.
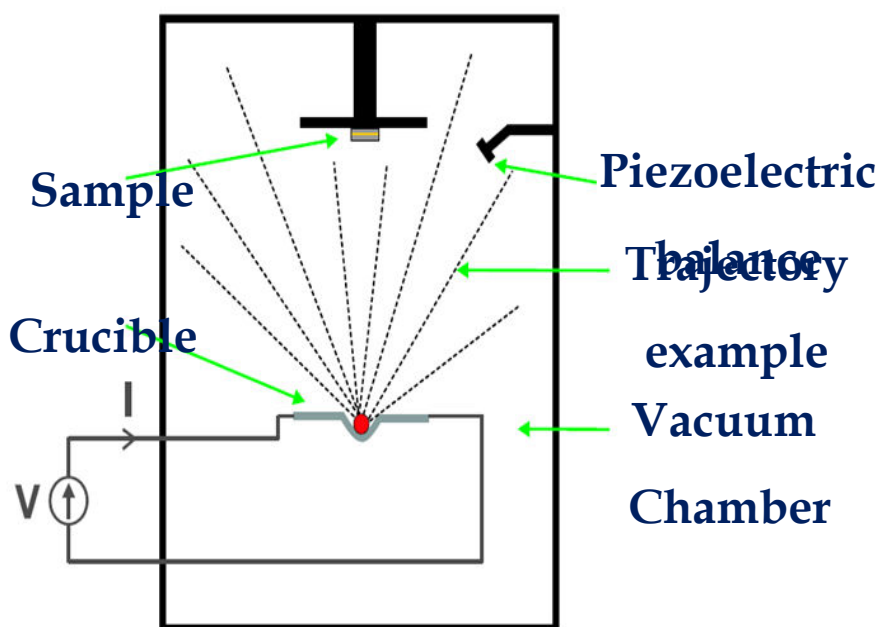
Figure 2.15 Schematic diagram of self evaporation frame.

2.6.3. Microcavity Preparation

In this thesis, we have embedded the perovskite molecule (PEPI) in a λ/2 Fabry-Pérot microcavity. The first step in the fabrication of microcavities is to clean the bottom dielectric mirror subsequently with three different solvents: acetone, ethanol and isopropanol in an ultrasonic bath, where each step lasts for 15 minutes. It is then immersed in a solution of 1 mole.L⁻

[1] KOH dissolved in ethanol for 15 minutes to modify the surface charge and thus to activate the silica surface for the self-organization of the perovskite layer. Then the dielectric mirror is rinsed by distilled water and dried by nitrogen flow. Note that the homogeneity of the PEPI film prepared on KOH treated surface is better than that prepared on untreated one.

In a second step, a 50 nm thin film of $(C_6H_5C_2H_4-NH_3)_2PbI_4$ (PEPI) perovskite is deposited on top of this dielectric mirror by spin coating a 10 wt% solution of $(C_6H_5C_2H_4-NH_3I)$ and PbI_2 dissolved in stoichiometric amounts in N,N-dimethylformamide (DMF). The parameters of the deposition by spin-coating are: a rotational speed of 3000 rpm^{-1} and a deposition time of 60 sec. The sample is then placed at 95 ° C for one minute to evaporate the remaining solvent and ensure the self organization.

Then in a third step, a 100 nm PMMA (polymethylmetacrylate) spacer layer is deposited on the perovskite layer by spin coating. A preparation of PMMA solution is needed: PMMA is dissolved in the toluene with a mass concentration of 4% of this solution. The parameters of the PMMA deposition are: a rotational speed of 2200 rpm^{-1} and a deposition time of 40 sec. The deposit by spin coating is then followed by annealing at 95 °C for 20 minutes. Note that besides the main role of the PMMA layer in adjusting the cavity photon mode, the PMMA layer plays an important role also in protecting the perovskite layer upon the deposition of the metallic mirror.

Finally, the microcavity is completed by a top metallic mirror which is produced by electron-beam evaporation of silver (thickness of 28 $\pm$ 5 nm) on the PMMA layer.

2.7. Conclusion

In this chapter, we have presented the different techniques: absorbance, angle–resolved reflectivity, angle-resolved photoluminescence, pump-probe experimental setup mounted at LAC-ENS Cachan and microphotoluminescence set-up of LPN, to study the optical properties of both perovskite thin films and microcavities containing them. The experimental setup used to perform µPL measurements was designed to give an image of the surface of the sample on the detector, in the real-space configuration, and of its Fourier plane, in the reciprocal space configuration. The pump-probe experimental setup has been explained in details, the width at half maximum of the cross-correlation pump and probe pulses have been estimated to be about 112 fs, the dispersion of "zero" with the wavelengths selected by the monochromator was also determined to allow its compensation when acquiring ΔT/T spectra. We then introduced a complete description of the fabrication of Standard PEPI based microcavities covered with a

silver metallic mirror. Some better cavities, presenting a higher quality factor, will be presented in chapter 4, for which the top mirror is a dielectric mirror.

Chapter3

3. Ultrafast carrier dynamics in hybrid organic-inorganic quantum wells

The work in the field of optoelectronic devices and in particular the photovoltaic ones highly recommend the knowledge of the carrier dynamics of the used materials. Dynamics should be closely monitored at operating temperature, which is normally the room temperature [72]. A lot of studies have been devoted to the optical studies of 2D perovskite , some about the excitonic structure [23, 24, 39, 73-76], or about the influence of the dielectric confinement [77-80]. For instance, the dielectric confinement effect on excitons has been demonstrated by varying the dielectric constant of the barrier material in PbI_4-based layered structures. It has been found that the dielectric confinement dominates the exciton binding energy, in contrast with conventional semiconductor quantum wells [80]: for example, the exciton binding energies in $(C_6H_{13}NH_3)_2PbI_4$ (named as C6-PbI$_4$) and $(C_6H_5C_2H_4NH_3)_2PbI_4$ (named PEPI) are 400 meV and 220 meV respectively.

On the other side, the excitonic non-linearities are not very well reported in the literature. Only some studies about the exciton relaxation and the existence of the excitonic molecule were reported in several papers. Fujita et al. [73] have estimated the half-life time of excitons in PEPI to be very short (5-10 ps) through time-resolved photoluminescence measurements performed at 10K. It has also been shown by Schimizu et al. [81] that the exciton absorption band in PEPI exhibits bleaching and blue shift which lasts for 10 ps when pump photon energy is set at the exciton resonance through a subpicosecond pump-probe spectroscopy performed at 5K. The excitonic molecule with a binding energy of 50 meV was observed in a PbI_4-based two-dimensional semiconductor structure by photoluminescence measurements performed at 2K by Ishihara et al. [78]. Once again, the large binding energy is due to the dielectric confinement effect, in contrast with conventional semiconductors where the binding energy of a biexciton is usually a few meV at most. Biexciton lasing has also been observed for the first time in C6-PbI$_4$ by Kondo et al [82]. Moreover, Kondo et al. [83] measured the third-order nonlinear susceptibility $\chi^{(3)}$ of the lead iodide based perovskite type material C6-PbI$_4$ by a transient four-wave mixing technique. A large modulus of $\chi^{(3)}$ of 1.6×10^{-6} esu was observed at the exciton resonance at 8K. This value of $\chi^{(3)}$ is larger than that of $(C_{10}H_{21}NH_3)_2PbI_4$ and of

one dimensional organic polymers, which was found to be equal to 10^{-9} esu by an optical third-harmonic generation measurement at room temperature [84]. A nondegenerate four-wave-mixing measurement was carried out for C6-PbI4 by Ishi et al. [85], to demonstrate biexcitonic contributions. The result was analyzed with a few-level model which includes biexcitons. Detuning dependence of the ac Stark shift in PEPI was studied using pump-probe spectroscopy by Schimizu et al., to show the contributions of the bound and unbound biexcitons [76]. It was also suggested that the giant oscillator strength model for the excitonic molecule may not be applicable due to the extremely strong light-exciton interaction [86].

Nevertheless, all these studies have been performed at low temperature and for high carrier densities where carrier-carrier interactions dominate the dynamics of the excitonic state, and to our knowledge, no information on the intraband relaxation is available in the literature. In this chapter, we report on the exciton dynamics in PEPI perovskites by means of pump/probe spectroscopy performed at room temperature and for both low and high carrier densities. The studied sample consists in a 50 nm film of $(C_6H_5C_2H_4NH_3)_2PbI_4$ perovskite (PEPI) deposited on a quartz substrate, corresponding to approximately 30 QW. It is obtained by spin coating a 10% wt solution of $C_6H_5C_2H_4-NH_3I$ and PbI_2 dissolved in stoichiometric amounts in N, N-dimethylformamide. The sample is then placed at 95 ° C for one minute. A 100 nm PMMA layer is then deposited by spin coating in order to protect the pervoskite. In fact, we have observed that the photostability of PEPI layers is greatly enhanced with this protection layer.

This section is divided into two parts: the first part will present the dynamics of excitons in PEPI layer under low excitation regime where multiexcitonic effects such as Auger effect are negligible, while the second part will study their dynamics under high excitation regime.

3.1. Protocol of measurement

The exciton dynamics is studied thanks to femtosecond pump/probe non-linear spectroscopy. The experimental setup has been described in details in **chapter 2**. The probe consists in a white light continuum which allows performing transient absorption spectroscopy. The energy of the probe pulse selected by the monochromator is fixed at 2.397 eV, which corresponds to the spectral position of the excitonic peak of PEPI (see **Figure 3.1**). On the other hand, the pump pulse can be tuned from 2.818 eV to 2.397 eV. The pump spectra are plotted as blue (2.818 eV) and green (2.397 eV) dash lines in **Figure 3.1**.

We have performed two sets of experiments in order to study the change of transmission and thus the change of absorption in PEPI quantum wells. In one set of experiments, the pump

pulse with energy in resonance with the excitonic band (2.397 eV) is used to generate primarily excitons. In the other set, the multi-quantum wells structure is excited above the 2D continuum [24] with pump energy at 2.818 eV.
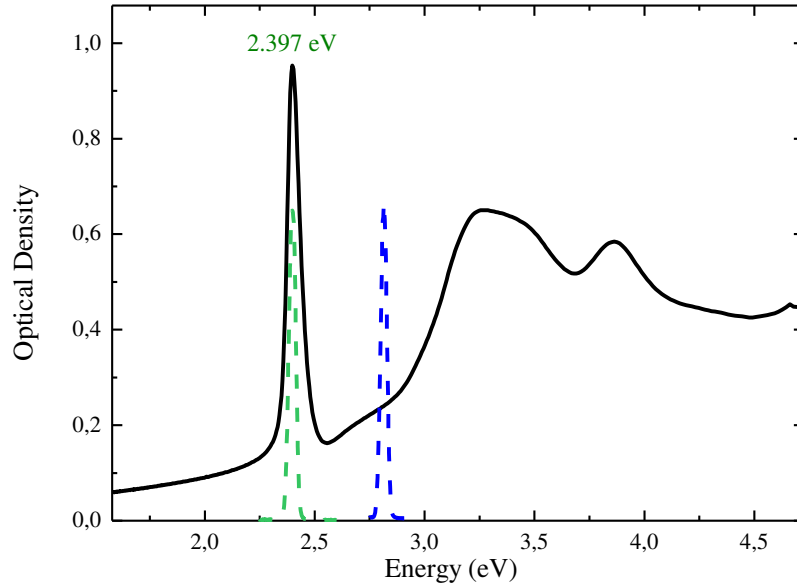
Figure 3.1 Optical density of a 50 nm PEPI layer. The spectrum of the pump is displayed in dash lines for a central energy of 2.397 eV (green) and 2.818 eV (blue).

One important parameter is the number of carriers per cm^2 injected in the multi-quantum wells structure. This quantity is defined as:

$$n = \frac{\text{power}}{1\text{kHz}.\hbar\omega.\text{S}}.(1-10^{-\text{O.D.}})$$

(3.1)

with S the surface of the spot in cm^2 at the surface of the sample, O.D. the optical density at the pump wavelength, and $\hbar\omega$ the energy of the photon.

In order to calculate the number of injected carriers for energies in resonance with the exciton (2.397 eV) and with the continuum (2.818 eV), the spot size of pump in these two configurations has been measured thanks to the knife edge method. It is based on recording the total power in the beam as a knife edge is translated through the beam using a calibrated translational stage. A powermeter is placed in the position of the sample in order to record the intensity of the Gaussian beam between $-\infty$ and the position of the knife. The signal can be fitted by a complementary error function:

$$S = A * \left(1 - \mathrm{erf}\left(\frac{\sqrt{2}x}{w} \right) \right)$$ **(3.2)**

and its derivative by a Gaussian. **Figure 3.2** shows the derivative of the intensity profiles recorded by the powermeter versus position for pump pulses at 2.397 eV (left) and 2.818 eV (right). The red line represents the Gaussian fit of the intensity profile where its FWHM is equal to the spot size. The spot sizes of the 2.397 eV pump pulse and the 2.818 eV pump pulse are measured to be 38 μm and 31μm respectively.

(a)   (b)
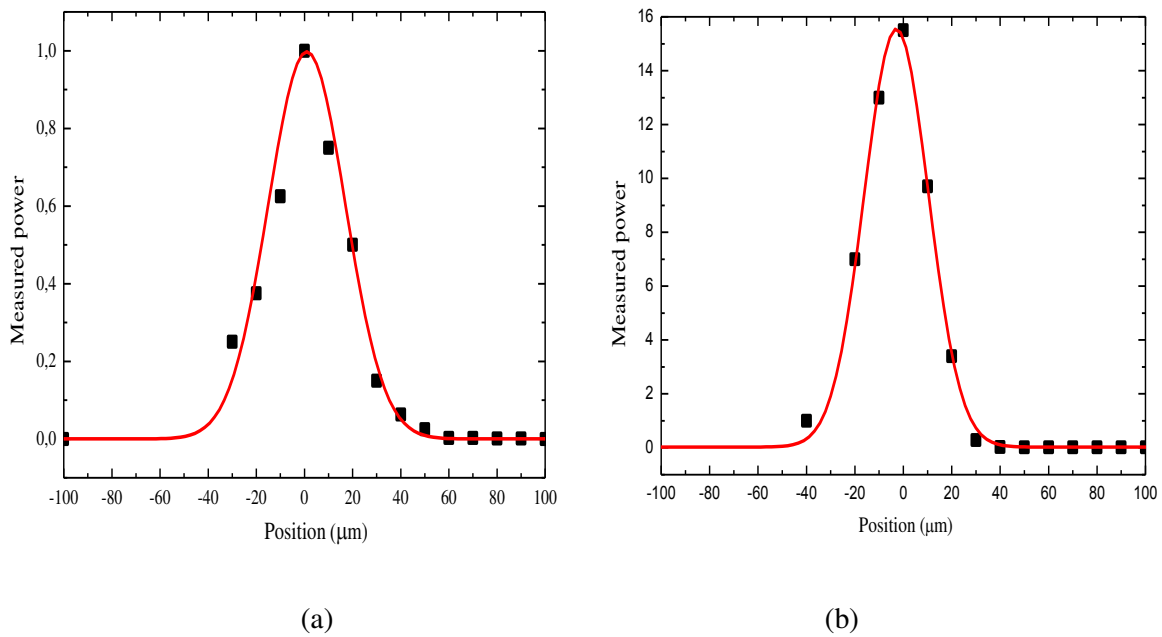
Figure 3.2 Plot of power output versus knife edge position for pump pulse of energies: (a) 2.397 eV and (b) 2.818 eV. Red line: Gaussian fit.

Figure 3.3 shows typical relative variation of transmission as function of the pump/probe delay for pump energies at 2.397 eV (left) and at 2.818 eV (right). In both configurations, a positive variation of the transmission is observed (photobleaching). The physics of this transient signal will be discussed in the next part of the chapter. Perovskite molecular quantum wells are hybrid organic-inorganic compounds. Their stability under illumination is better than common organic materials [21]. Nevertheless, when exposed to energetic pulses such as the ones provided by this optical parametric amplifier, the molecular structure of perovskites can be degraded. Therefore, in order to extract intrinsic physics from these pump/probe experiments, one has to pay attention to this problem. Moreover, the samples studied in this thesis consist in spincoated layers. The optical absorption spectrum is measured to be the same on different points of the same PEPI layer or on two different PEPI layers as the one shown in **Figure 1.6**.

This shows that the mean value of the layer thickness is well controlled at the millimeter scale of the spot size of optical absorption experiment [20]. Nevertheless, thickness of lateral fluctuations of 1-2 μm is well observed by the AFM images of PEPI thin films in **Figure 3.4** with a scanning area of 10*10 micrometers [13].
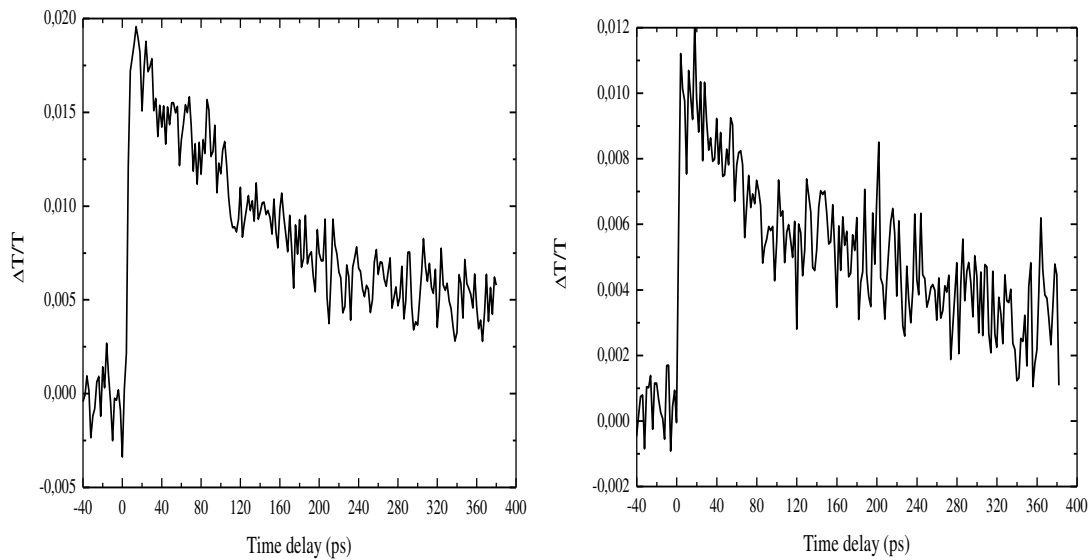
Figure 3.3 Relative variation of transmission in function of pump/probe time delay. Left side: Pump and probe at 2.397 eV, carrier density: 2.17×10^{13} cm^{-2}. Right side: Pump at 2.818 eV, probe at 2.397 eV, carrier density: 1.29×10^{13} cm^{-2}.
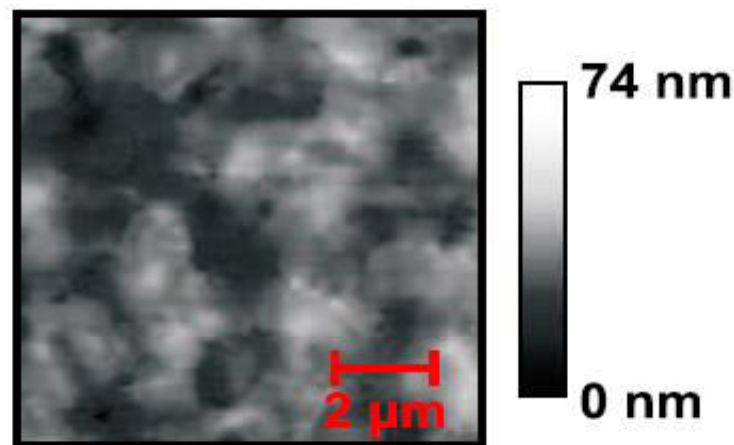
Figure 3.4 Typical AFM image for a PEPI thin film.

These fluctuations may induce some dispersion in the value of the optical density at the scale of the spot size (~30 μm) in the pump/probe experiments, and then in the evaluation of the carrier density. In order to address these questions, two methods have been used. First, statistics of the amplitude of the relative variation of transmission have been performed. **Figure**

3.5 reports statistical measurements over 50 point both for pump in resonance with the exciton and above the continuum. The mean value of the amplitude of $\Delta T/T$ normalized by the carrier density (n) at zero time delay is 8.7 x10^{-16} for pump at 2.397 eV and 9.8x10^{-16} for pump at 2.818 eV. The standard deviation is 7.4x10^{-17} for both cases, which leads approximately to a 8 % dispersion on the $\Delta T/T/n$ amplitudes from one point to another on the sample. Finally, the amplitude of the transient photobleaching of the exciton line is quite identical for a given carrier density whether the pump is tuned in the continuum or in resonance with the exciton.
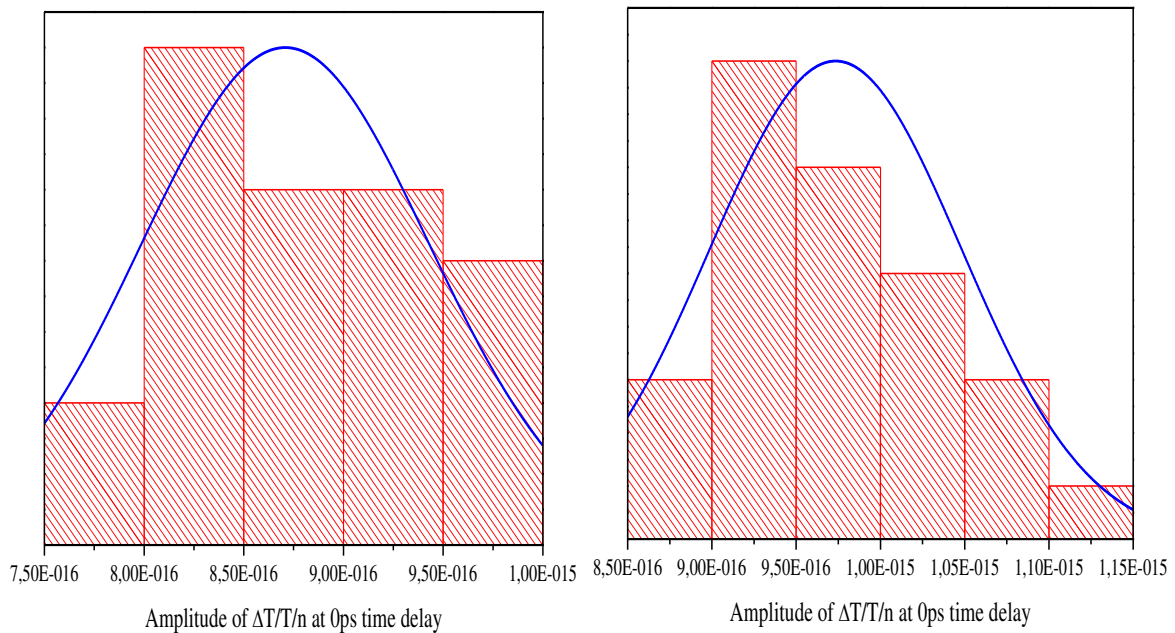
**Figure 3.5**: Statistics of the photobleaching amplitude normalized by carrier density (n), for pump at 2.397 eV, n= 2.17x10^{13} cm^{-2} (right) and pump at 2.818 eV, n= 1.29 x10^{13} cm^{-2} (left).

The second procedure was implemented to perform several acquisitions one after the other on the same point and to compare both the amplitudes and the dynamics. **Figure 3.6** shows a series of three scans acquired at the same point. Both the amplitudes and the dynamics are identical within the noise. It allows to state that no degradation of the materials is occurring during the acquisition time. In the end, it also allows to perform an averaging over the scans to improve the signal to noise ratio.

Finally, because experiments are performed at the limit of the signal to noise ratio in order to work at the lowest carrier density, the averaging procedure has been extended to acquisitions performed on different points on the samples. **Figure 3.7** displays normalized acquisitions which show the same dynamics within the uncertainty due to the low signal to noise ratio. The curve resulting from the averaging of the six scans is plotted, showing an improvement of the

signal to noise ratio of a factor ~ 3 - 4. In this manuscript, each time this procedure has been used, this will be mentioned in the text.
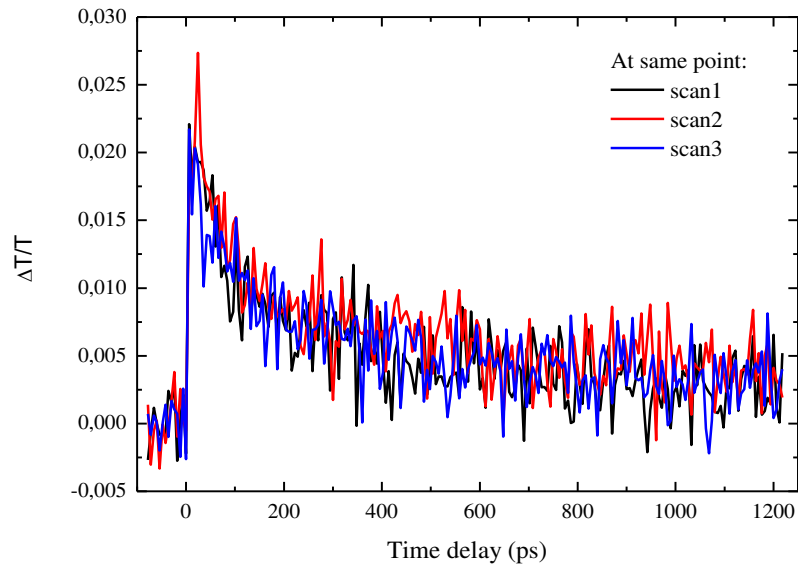
Figure 3.6: Series of three scans acquired at the same point in function of time delay between pump and probe pulses.
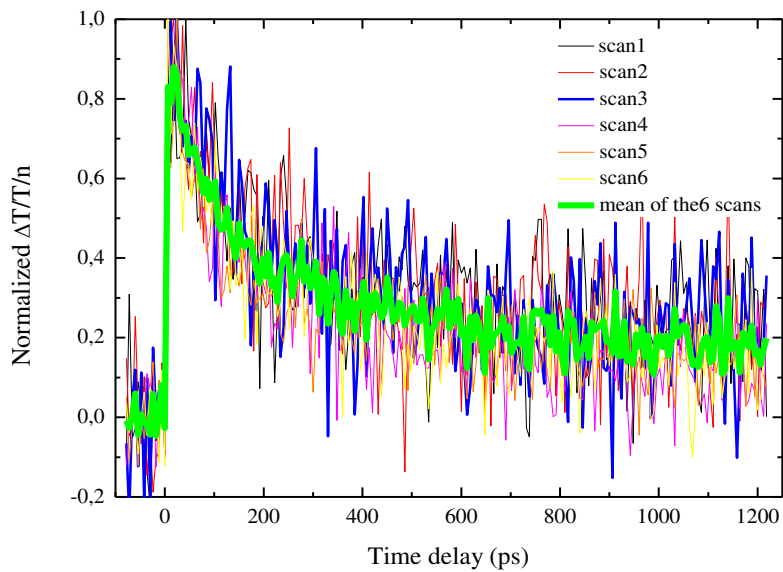
Figure 3.7: Normalized ΔT/T as function of time delay between pump and probe pulses measured over 6 points and its mean. Pump and probe at 2.397 eV, $n=2.17 \times 10^{13}$ cm^{-2}.

3.2. Dynamics of the excitonic state: low excitation regime

In this part, the dynamics of the excitonic state is investigated at room temperature in a degenerated configuration where both pump and probe pulses are tuned with the exciton line. The absorption of the pump pulse creates some excitons and the probe pulse monitors the

variation of transmission of the excitonic transition as function of the delay between pump and probe pulses. Because relative variation of reflectivity (ΔR/R) is negligible in comparison to the one of the transmission (ΔT/T)[2], the relative variation of transmission is related to a transient change in the absorption coefficient of the excitonic line. In this section, we report experiments performed at the lowest carrier density (2.17×10^{13} cm^{-2}) at the limit of our signal to noise ratio. The goal was to work at carrier densities for which multi-excitonic effects such as Auger assisted relaxation are negligible.

Figure 3.8: Relative variation of transmission normalized by the carrier density (n) in function of time delay between pump and probe pulses (mean over 6 acquisitions). Pump and probe at 2.397 eV, n=2.17×10^{13} cm^{-2}. The red curve is a bi-exponential fit.

Figure 3.8 displays the relative variation of transmission averaged over 6 points in function of time delay between pump and probe pulses for both pump and probe pulses tuned in resonance with the excitonic transition. It shows a positive variation of transmission of ~2.10^{-2} which corresponds to a transient decrease of the absorption coefficient. When pump/probe delay increases, ΔT/T decreases to reach a plateau at long time delay[3]. The red curve corresponds to a fit with a bi-exponential decay. The main contribution to the relaxation at short time delay is fitted with a lifetime τ_R ~ 110 ps. The long tail is not resolved in our experiment. The fit begins to converge for a recombination time higher than 5 ns. The interpretation of these observations is not straightforward, and the lack of information on the band structure of PEPI

---

[2] In practice, no signal has been obtained for ΔR/R.
[3] 1200 ps is the highest delay that can be reached on this experimental setup.

makes it even more difficult. Nevertheless, a first interpretation can be done. Thanks to PL and PLE (Photoluminescence Excitation) experiments in function of temperature, it has been previously stated that some excitons can be localized on defects of the structure at room temperature with activation energy of the order of few tenth of meV [24]. Then, the population of excitons should be composed both of free and localized excitons leading to a bi-exponential decay. Therefore, we interpret the 110 ps relaxation time as the one of "free" exciton whereas the long tail is attributed to the localized excitons.

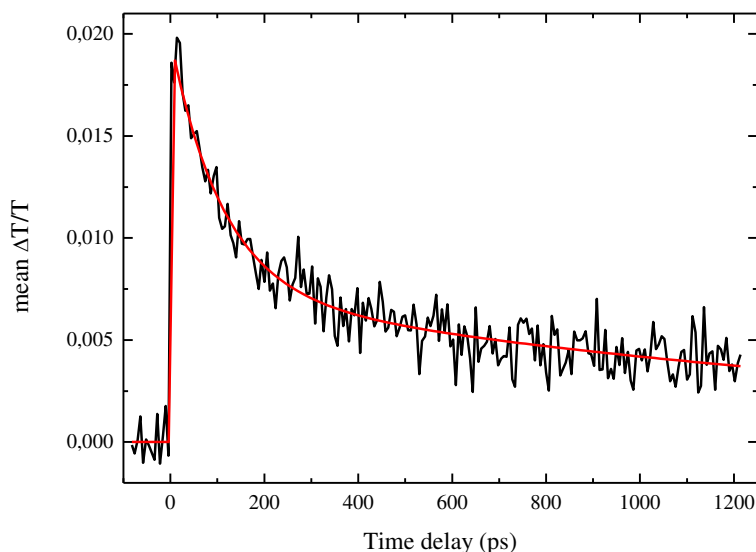**Figure 3.9** Relative variation of transmission normalized by the carrier density in function of time delay between pump and probe pulses in a log-log scale. Pump and probe at 2.397 eV, n=2.17x10^{13} cm^{-2}. The red curve is a fit with a stretched exponential.

In the light of the previous discussion, the problem could be addressed in another way. Perovskite films obtained by spin-coating can be viewed as disordered materials as shown by the AFM image in **Figure 3.4**. In these kind of materials, recombination of electron-hole pairs are often described with stretched exponentials:

$$I(t) = I_0 e^{-ct^\beta}$$ (3.3)

where I is, for instance, the PL intensity, c is a constant independent of time and β a parameter somehow related to the disorder. These relaxation behaviors have been observed in several disordered materials such as porous silicon [87], CdSe-ZnSe superlattice [87], AlInGaN alloys [88] etc… **Figure 3.9** shows the relative variation of transmission in function of the time delay

(black) and a fit with a stretched exponential (red). The data are quite well fitted with a stretched exponential model suggesting that disorder indeed plays an important role in the relaxation mechanisms. Nevertheless, the parameters (c ~ 1.54 ± 0.76 ps^{-1}; β ~0.15±0.04) display large error bars, and are difficult to interpret in terms of simple physical parameters. The physical origin of this behaviour in the relaxation mechanisms may have different origins. It can come from energetic disorder, meaning that excitons can move from localized states to delocalized states. It can also result from hopping of excitons between localized stated (topological disorder) [88]. To investigate this point, more experiments are needed. First, time resolved photoluminescence experiments will be performed in the next months. It will, for instance, tell us whereas all the spectral components of the PL spectrum have the same dynamics or not. Experiments in function of the temperature will also be performed. In fact, theory suggests that within the stretched exponential relaxation model, the variation of the β parameter with the temperature is related to the disorder physical mechanisms. Indeed, a variation of β with the temperature would be related to energetic disorder whereas a constant β would come from dispersive tunnelling mechanisms [88, 89]. Finally, one can also work on the fabrication of the perovskite films to vary the disorder of the structure. In this context, it would be interesting to perform experiments on films obtained by co-evaporation techniques that are known to lead to higher crystalline structure as it enhances for instance the mobility in 3D-perovskite based solar cells [90].

3.2.1. Intraband relaxation

The relative variation of transmission of the sample in function of time delay for a pump pulse tuned in the continuum (E_p = 2.818 eV; E_s = 2.397 eV), has been performed. Since the measurements were performed under similar conditions as the previous ones, in the limit of signal to noise ratio, the mean value of ΔT/T over 9 points is reported in **Figure 3.10**. As for the degenerated configuration, the signal can be fitted with a bi-exponential decay with τ_X ~ 100 ps and a long tail which is not resolved in this experiment. **Figure 3.11** shows the comparison of ΔT/T in function of the time delay for pump energies at 2.818 eV (red) and 2.397 eV (black). Within the measurements incertitude, the two curves are superimposed, showing that the recombination dynamics is the same regardless of the energy at which carriers are injected.
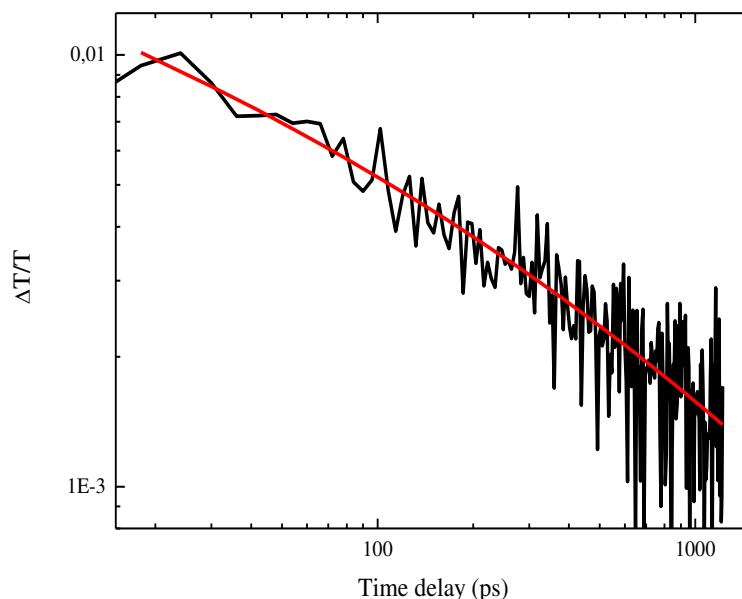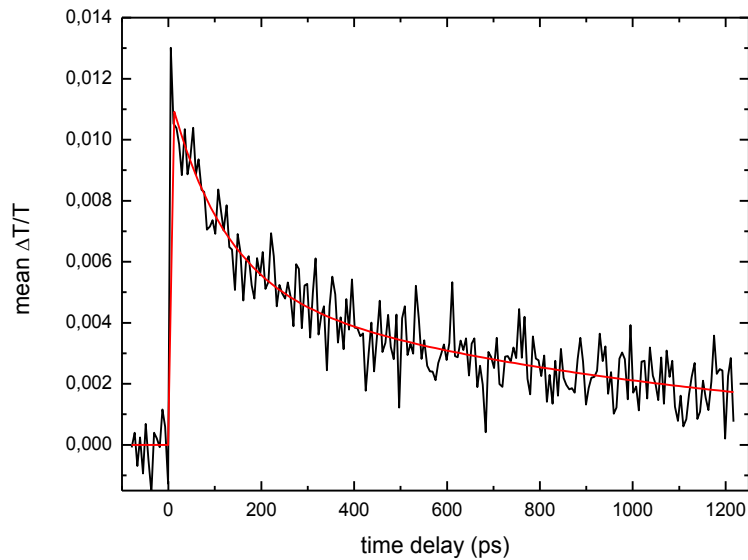
Figure 3.10 Mean relative variation of transmission over 9 points normalized by the carrier density (n) in function of time delay between pump and probe pulses. Pump at 2.818 eV and probe at 2.397eV, n=2.17x10^{13} cm^{-2}.
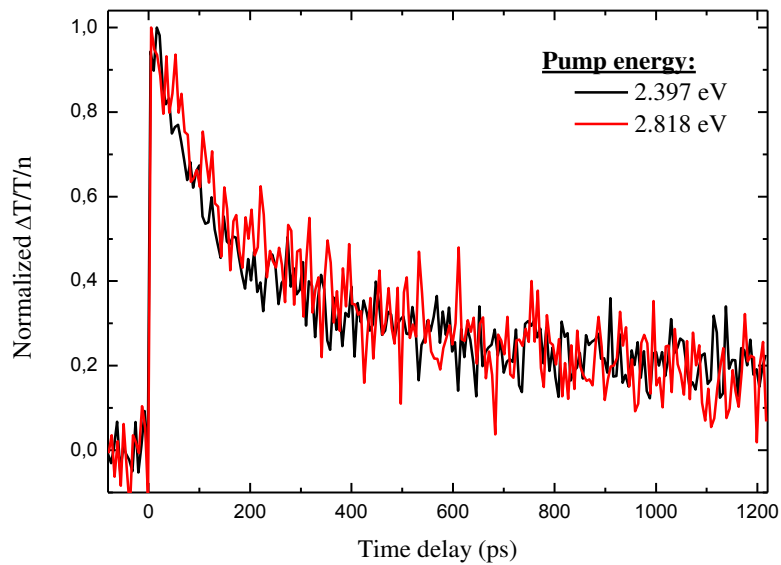
Figure 3.11: Comparison between normalized ΔT/T for pump energies at 2.397 eV (black) and 2.818 eV (red).

Figure 3.12 shows a zoom at short delays for different pump energies between 2.397 eV and 2.818 eV. One can notice that the different curves superimpose within the measurements uncertainties. This observation means that no sizeable rise time is observed. Therefore, one can conclude that the intraband relaxation down to the excitonic state is faster than the time

resolution of the experiment i.e. ~150fs. One can argue that this instantaneous signal could be due to a screening of the transition due to the presence of carriers in the continuum, without the presence of carriers on the exciton state. Nevertheless, excitonic population has to build up to lead to luminescence. Therefore, a relaxation of carriers from the continuum to the exciton state has to occur. The fact that transient bleaching curves superimposed on the different time scales (100 fs to 1000 ps) rules out the screening interpretation. Moreover, we have seen in **section 3.1**, that the amplitude of the transient bleaching normalized by the number of injected carriers is the same whether the pump pulse is in resonance with the exciton line or above the continuum. This observation means that approximately all the carriers injected in the continuum are recovered on the ground state within the pulse duration. This supports the interpretation of an ultrafast intraband relaxation.
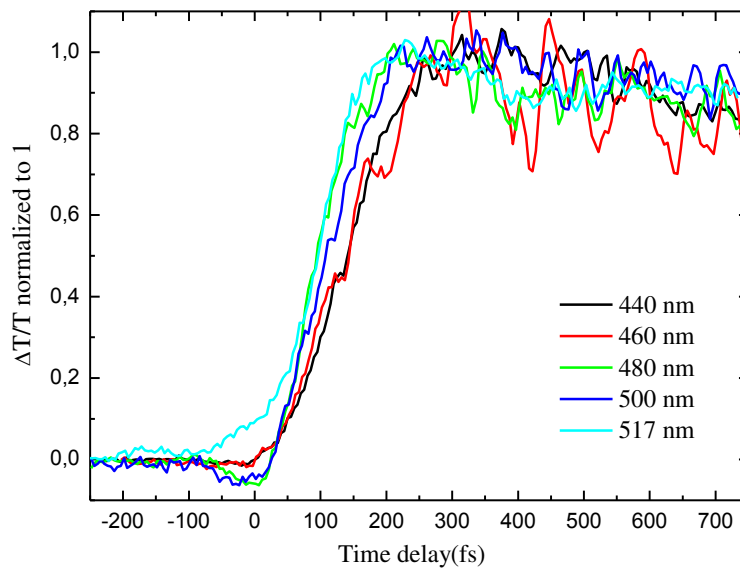
Figure 3.12: Normalized variation of transmission in function of the pump/probe time delay for different pump energies. Probe at 2.397 eV.

This value of hundred of femtoseconds has to be compared with the energy difference between the initial and final states i.e. around 421 meV (2.818 - 2.397 eV). In common semiconductors where excitons have small binding energies, the intraband relaxation is phonon assisted. In particular, a 130 fs relaxation time per emitted LO-phonon has been measured in CdZnTe quantum wells [91, 92]. In hybrid 3D perovskite, the phonon energies are in the range of 8 meV (vibration of inorganic cage) [109]. If we assume that the value of 2D perovskite phonon has the same order of magnitude than the 3D one, a phonon assisted relaxation would therefore lead to 7 ps intraband relaxation. One can argue that the strong phonon coupling occurring in these materials [24] should lead to a speed-up of the relaxation time per emitted

phonon. Even if this time was as fast as 10fs, it should lead to a sizeable rise time (600 fs) in the pump/probe signal. Therefore, common assisted phonon mechanism cannot alone account for this sub 150 fs intraband relaxation. Ultrafast intraband relaxation has also been reported in CdSe quantum dots [93, 94], in 3D perovskite [72] and organic semiconductors [95-97]. In CdSe, the relaxation of hot carriers depends on the size of the dot and can vary from picoseconds to few hundreds of femtoseconds. In 3D perovskite, a 0.4 ps hot hole cooling has been reported, whereas in organic semiconductors it can go down to around 100 fs. In order to account for these ultrafast relaxation times, two main mechanisms are invoked. The first mechanism that leads to ultrafast relaxation is related to non-adiabatic relaxation pathways. It is based on the breakdown of the Born-Oppenheimer approximation where vibrational motions and electronic states cannot be separated [94]. To test this hypothesis, experiments at low temperature are planned. The second mechanism consists in Auger mediated recombination. For instance, in CdSe quantum dots, a hot exciton cools down through the interaction with a hole in an Auger process. These processes have attracted much attention for few years since they can be at the origin of multiple exciton generation, mechanism of high interest for photovoltaic applications [97]. Therefore, the observation of such a process in 2D perovskite should bring attention on these materials.

3.2.2. Analysis of carrier dynamics

Let us now discuss the origin of the exciton line bleaching. Excitons are quasi-boson particles composed of two fermions: an electron and a hole. The presence of excitons in the system fills the conduction and valence band states from which they are formed. This is called Phase Space Filling (PSF) and leads to a reduction of the oscillator strength (f_X) of the transition due to the decrease of the density of states available to perform the optical transition. Moreover, Coulomb interaction between electrons and holes from different excitons can also lead to a renormalization of the exciton wave function. The renormalization can affect both the oscillator strength and the energy of the exciton transition $\hbar\omega_X$. Finally, the 2D dimensionality enhances the collision probability between excitons in comparison to the bulk case. These collisions can lead both to broadening of the transition linewidth (Γ_X) and to the opening of new Auger assisted relaxation channels (see section 3.5 for the latter).

In order to investigate which physical parameter (f_X, ω_X, Γ_X) is influenced by the presence of excitons in the quantum well structure, transient spectra have been performed. **Figure 3.13** displays the relative variations of transmission spectra as function of energy at

different pump/probe delays. The main feature is a positive variation of transmission (photobleaching) at the energy of the exciton line and a negative signal (induced absorption) on the wings.
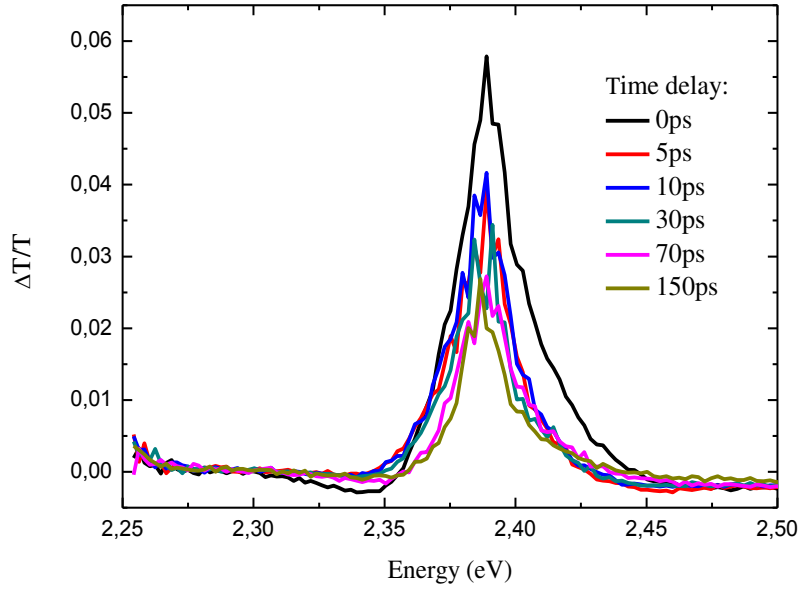
Figure 3.13 Spectra of relative variation of transmission for different pump/probe time delays. Pump at 2.818 eV; n= 1.29 x10^{13} cm^{-2}.

The exciton line of PEPI being non symmetric, the analysis of $\Delta T/T$ is not straightforward. In order to disentangle which physical parameter is influenced by the presence of excitons, data have been analyzed by the momenta method following the procedure proposed by Litvinenko at al. for GaAs/AlGaAs quantum wells [98]. In this analysis, the zeroth, first and second order moments correspond to the oscillator strength f_X, the energy of the exciton $\hbar\omega_X$ and the square of the linewidth Γ_X respectively.

Thus, the three quantities f_X, ω_X, Γ_X are calculated via the following equations:

$$f_x \propto \int \alpha(\hbar\omega)d\omega \tag{3.4}$$

$$\hbar\omega_x \propto \int \hbar\omega\alpha(\hbar\omega)d\omega / f_x \tag{3.5}$$

$$\Gamma_x^2 \propto \int (\hbar\omega - \hbar\omega_x)^2 \alpha(\hbar\omega)d\omega / f_x \tag{3.6}$$

where $\alpha(\hbar\omega)$ is the absorption coefficient at the energy $\hbar\omega$.
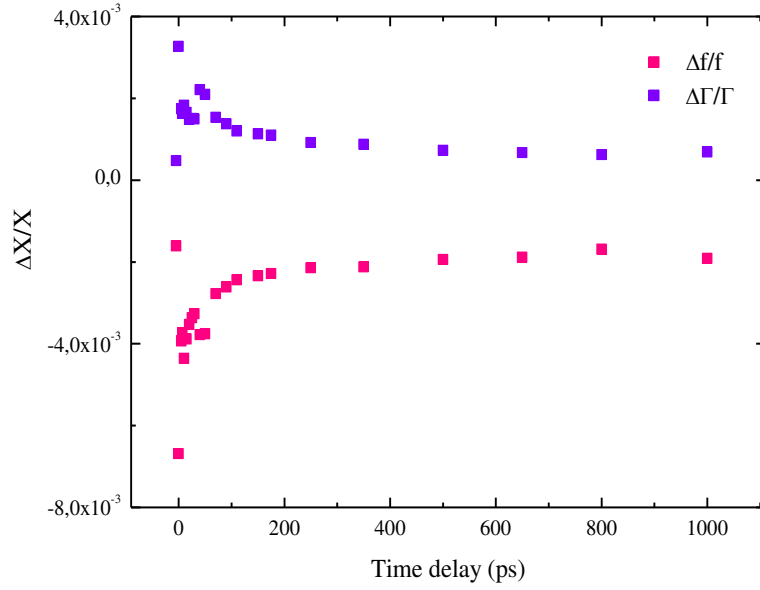
Figure 3.14 Results of moment analysis. f stands for the oscillator strength, Γ for the linewidth, Pump at 2.818 eV, probe at 2.397 eV.

We can observe from **Figure 3.14** that both f_X and Γ_X^2 are modified by the presence of excitons. On the contrary, ω_X is not modified or at least more than one order of magnitude smaller than f_X and Γ_X quantities. At zero delay, the reduction of oscillator strength $\Delta f / f$ is of the order of 7.10^{-3} and the broadening $\Delta\Gamma / \Gamma$ around 3.10^{-3}. The variation of these parameters is what is observed in common inorganic quantum wells [98]. In order to compare the amplitude of these effects in these two materials, we normalized the relative variation ($\Delta f / f$, $\Delta\Gamma / \Gamma$) by the quantity $\dfrac{n \times \pi a_0^2}{N_{QW}}$, where n is the carrier density, a_0 is the exciton Bohr radius and N_{QW} is the number of wells. This quantity is of the order of 5.10^{-3} for GaAs/AlGaAs, and 3.10^{-2} for PEPI[4]. Both $\Delta f / f$, and $\Delta\Gamma / \Gamma$ are two orders of magnitude smaller in PEPI than in GaAs/AlGaAs quantum wells [98].

To compare our experimental results with theoretical ones, we present here the model developed by Schmitt-Rink et al. [99] to study the excitonic non-linearities for two dimensional systems. In fact, this model gives analytical results for the contributions of $(f_X, \omega_X, \Gamma_X)$ to exciton bleaching. These three parameters are linked to the exciton line through its susceptibility, which is defined as:

---

[4] For PEPI the numerical values are: $a_0 \sim 1.5$ nm, $N_{QW} \sim 30$, $n \sim 10^{13}$ cm^{-2}. For AlGaAs the numerical values are: $a_0 \sim 5.9$ nm, $N_{QW} \sim 20$, $n \sim 10^{11}$ cm^{-2} [98]

$$\chi(\omega) \approx \frac{f_x}{\omega - \omega_x + i\Gamma_x} \tag{3.7}$$

As one or more of these 3 quantities (f_X, ω_X, Γ_X) is changed by optical excitation, the excitonic non-linearities arise. According to Miller et al. [100] and Knox et al. [101], no energy shift of the exciton peak is observed. This simply reflects the charge neutrality of the exciton. After neglecting the effect of the variation of exciton energy, the authors move to study the effect of the variation of the exciton oscillator strength.

The relative variation of the exciton oscillator strength is defined as:

$$\frac{\delta f_X}{f_X} = -\frac{n}{Ns} \tag{3.8}$$

where Ns is the exciton saturation density. The negative relative change of the oscillator strength, that is to say the reduction of the oscillator strength, can be explained in two processes:

- the blocking mechanism (Phase Space Filling) due to the Pauli exclusion principle
- the changes in the exciton orbital wavefunction due to the modification of the electron-hole interaction induced by the presence of other electron-hole pairs which includes both exchange effects and long-range Coulomb effects

In order to go further, the wavefunction of two-dimensional excitons is introduced. It is defined as:

$$U_X(r) = \left[\frac{2}{\pi}\right]^{1/2} \frac{2}{a_0} e^{-2r/a_0} \tag{3.9}$$

$$U_X(k) = \sqrt{2\pi} \frac{a_0}{\left[1 + (a_0 k / 2)^2\right]^{3/2}} \tag{3.10}$$

where a_0 is the usual 3D Bohr radius. According to [102, 103], the long range Coulomb effects on relative change of oscillator strength is very small at 2D and so Phase Space Filling and exchange effect are only taken into account in this study. The reduction of the exciton oscillator strength due to the Phase Space Filling contribution is defined as:

$$\left.\frac{\delta f_X}{f_X}\right|_{PSF} = -\sum_k \left[(f_e(k) + f_h(k)\right] \frac{U_X(k)}{U_X(r = 0)} \tag{3.11}$$

where $f_{e,h}(k)$ are the electron and hole distribution functions given by:

$$f_e(k) = f_h(k) = \frac{N}{2} \left| U_X(k) \right|^2 \tag{3.12}$$

One can thus obtain the following relation:

$$\left. \frac{1}{N_S} \right|_{PSF} = \frac{32}{7} \pi a_{2D}^2 \tag{3.13}$$

where a_{2D} is the Bohr radius of 2D exciton ($a_{2D} = a_0/4$).

By evaluating n and $1/N_{S(PSF)}$, the reduction of the oscillator strength for PEPI related to Phase Space Filling $\delta f_x / f_x$ is of the order of few 10^{-1} for a 2D Bohr radius of 1.5 nm and a carrier density of the order of 10^{13} cm^{-2}. This value is two orders of magnitude higher than our experimental findings as shown in **Figure 3.14**. This highlights the need of advanced calculations in order to describe the excitonic physics in these hybrid quantum wells.

Let us now consider the reduction of the oscillator strength due to the renormalization of the exciton orbital wavefunction. In the presence of other excitons, the bound state binding energy is weakened thus the probability of finding electron near the hole is reduced. This gives rise to another reduction of oscillator strength. The change of binding energy can lead to either change of exciton energy or continuum. In order to investigate these effects, the relative variation of transmission of the sample for a probe tuned to the continuum edge (blue side of the excitonic transition) was recorded as seen in **Figure 3.15**. We can see that the variation of transmission remains positive for probe tuned from 2.389 eV to 2.441 eV. Then, a negative variation of transmission is observed for the energy of the probe pulses tuned from 2.441 eV to the continuum. This negative signal is related to an induced absorption.
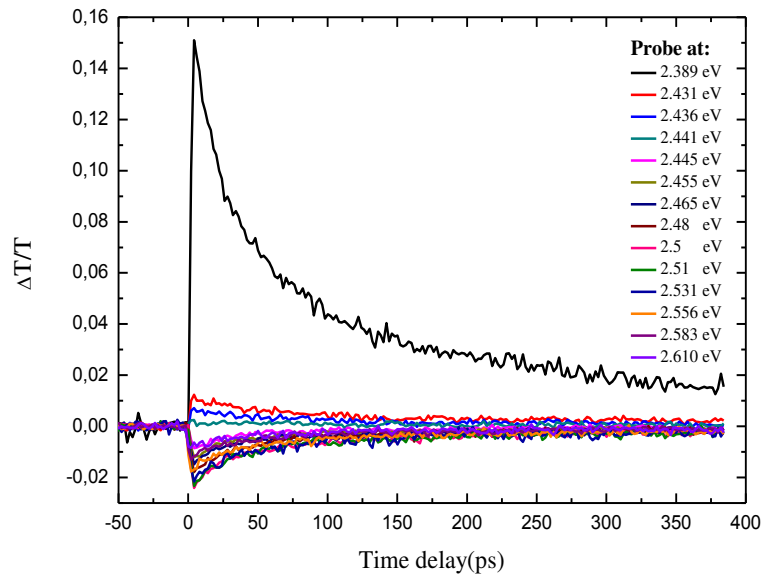
Figure 3.15 Relative variation of transmission in function of pump/probe time delay. Pump at 2.818eV and probe tuned from exciton energy to continuum edge.

Moreover, **Figure 3.17** shows the comparison between the dynamics of this negative variation of transmission and the one of the bleaching of the exciton line. Both dynamics are identical, meaning that the induced absorption observed at the continuum energy is due to the presence of excitons in the system. We interpret this induced absorption as a consequence of a transient red-shift of the continuum. **Figure 3.16** shows a scheme of red shift of continuum. This shift should be a consequence of the exciton wavefunction renormalization. In fact, the renormalization can be understood as a spread of the wavefunction in the real space that induces a decrease of the exciton binding energy. The exciton binding energy is defined as the difference between the exciton and continuum energies. Then a reduction of the binding energy can lead both to a blue shift of the exciton line and a red-shift of the continuum. Since the excitonic line does not show any shift (or at least a small blue shift), the red-shift of the continuum is a signature of the exciton wavefunction renormalization.
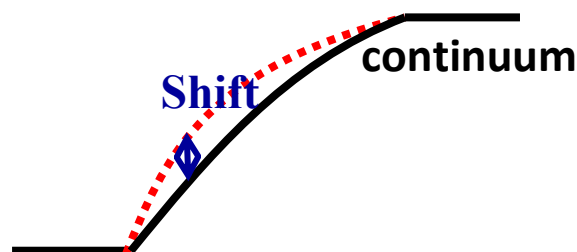

Figure 3.16 Scheme of red shift of continuum.
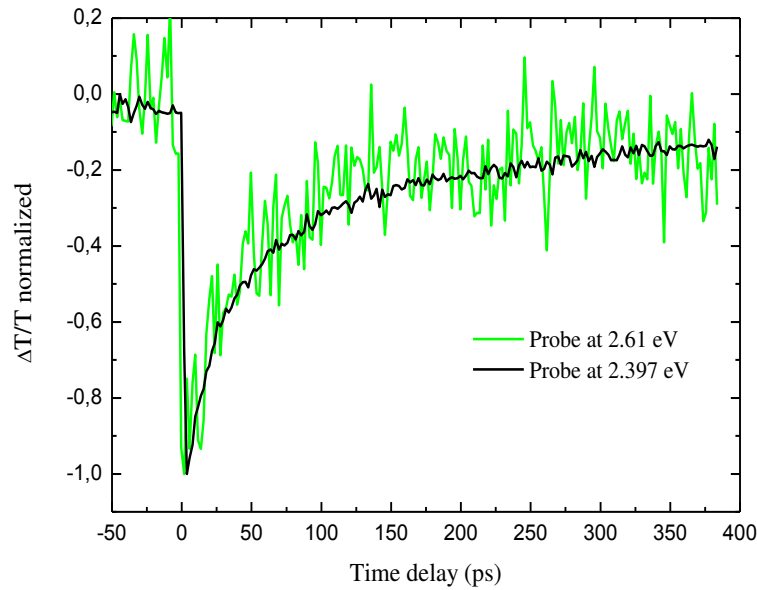
Figure 3.17 Relative variation of transmission in function of pump/probe time delay. Pump at 2.818eV; probe at 2.397 eV (black line) and at 2.61 eV (green line).

Therefore, the reduction of the oscillator strength in PEPI is related to both Phase Space Filling and renormalization effects. The latter can be viewed as screening effects. In PEPI, the dielectric confinement due to the difference in the dielectric constants of the organic and inorganic parts, have a strong influence on the excitonic properties of this material [80]. This mechanism is nothing more than screening effects. It is therefore not so surprising that screening effects such as wavefunction renormalization play an important role in the physics of these hybrid quantum wells.

Finally, let us now discuss briefly the transient broadening of the exciton line induced by excitons themselves. As in conventional inorganic quantum wells, this may come from collisions broadening. To test this, one should perform experiments in function of the injected carrier density. Unfortunately, increasing the carrier density leads to the appearance of a fast component at low delays that may be due to exciton-exciton annihilation[5]. On the other hand, decreasing the carrier density brings the data under our signal to noise ratio. Nevertheless, it is reasonable to attribute the transient broadening to collisions.

3.3.   Excitonic dynamic study as function of carrier density

The interactions between excitons have been widely discussed in recent years due to their key role in the operations of optoelectronic devices. For example, the process of Auger effects

---

[5] Some studies in high carriers density regime are presented in the next part of this chapter

becomes of increasing importance at high carrier density. This effect acts as a limiting factor on the performance of lasers for which it increases the lasing threshold. To study these processes in our quantum wells, we conducted time resolved pump-probe experiments as function of the pump fluence. The results of the normalized $\Delta T/T$ as function of time delay between pump and probe pulses for the pump energy in resonance with the continuum (2.818 eV) is presented in **Figure 3.18a** for different pump powers. For the data reported, an average pump power between 0.1μW and 6.4 μW was focused onto the sample surface, producing fluences of 13 μJ.cm^{-2} to 848 μJ.cm^{-2}. We can see that the relaxation dynamics is accelerated as the fluence increases. This general behavior is observed in semiconductor nanostructures (quantum wells, quantum dots) where Auger effects come into play [104, 105]. Moreover, at long time delay, one can observe that the contribution of the process with a recombination time higher than 5 ns (see section 3.2) is decreasing while increasing the pump fluence. In addition, a zoom at short time delays (up to 800 fs) for different fluences varying between 13 μJ.cm^{-2} to 848 μJ.cm^{-2} is presented in **Figure 3.18b**. We can see that the curves from different fluences superimpose within the measurements uncertainties. This shows that intraband relaxation does not vary with the fluence or is accelerated at a time scale below the resolution of the setup.

(a)   **(b)**
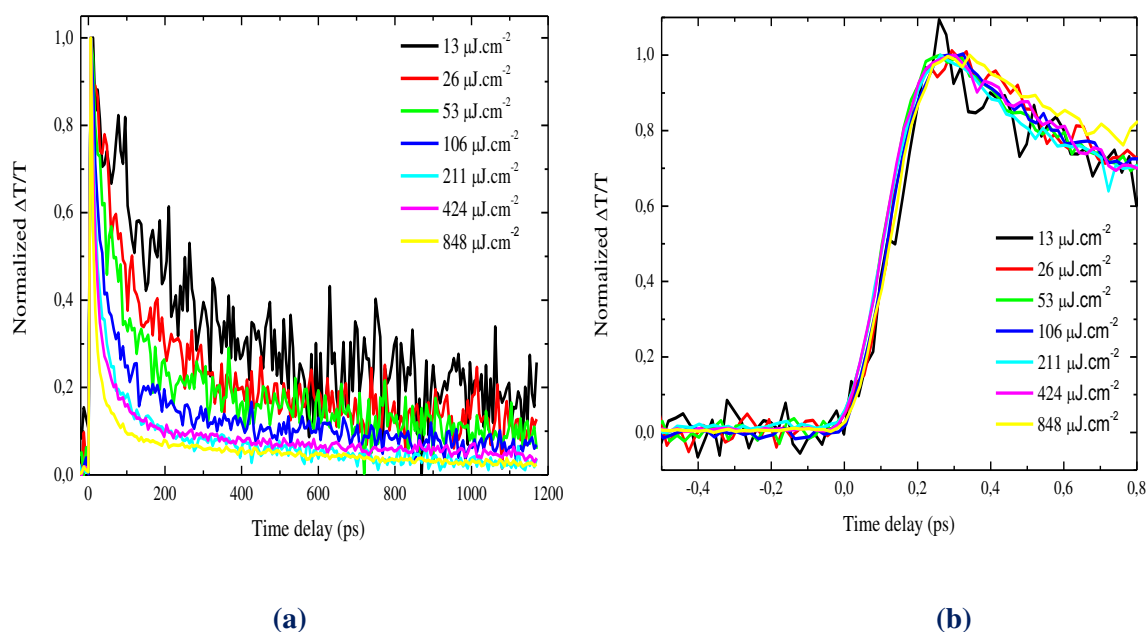
Figure 3.18 The normalized relative variation $\Delta T/T$ of sample in function of time delay between pump and probe. Pump at 2.281 eV. **a)** Fluence varies from 13 μJ.cm^{-2} to 848μJ.cm^{-2}. **b)** Zoom at a time delay up to 800 fs.

We first discuss the overall acceleration of the dynamics by increasing the fluence. Auger effect is a non radiative process that occurs when two excitons collide. It depends on the exciton diffusion constant and on the excitons size. In this process an exciton recombines via energy

transfer to an exciton that is excited to a higher energy state within or outside the quantum well without emitting a photon. This process is shown in **Figure 3.19.**
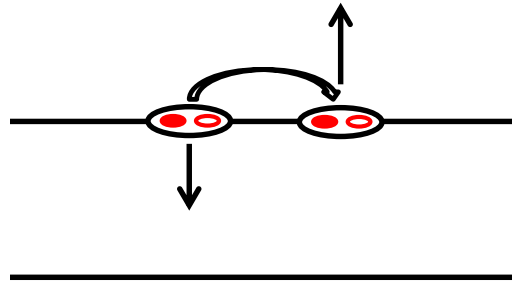
Figure 3.19 Auger recombination process.

The Auger effect can be included in the rate equation: $\dfrac{dN}{dt} = -\gamma.N - \gamma_{Auger}.N^2$

(3.14) which describes the recombination of exciton population $N = N(t)$, where γ_{Auger} is the Auger recombination (AR) constant. We have first numerically solved the equation and fit the curves in **Figure 3.18a**. The fit is shown in **Figure 3.20** for two different excitation densities.

(a)   **(b)**
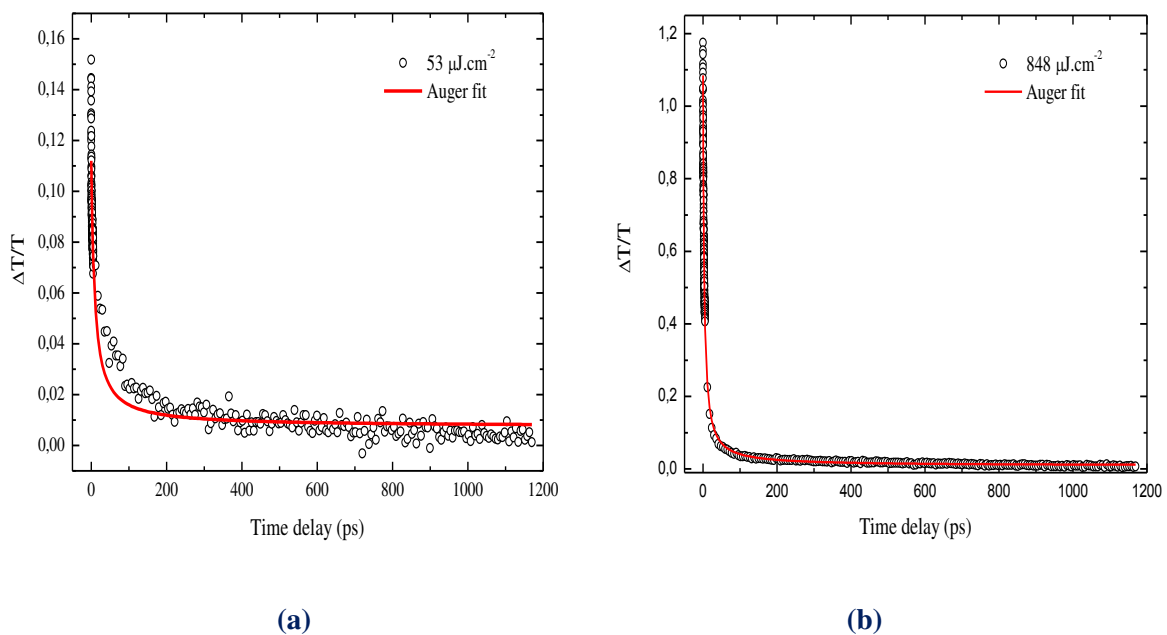
Figure3.20 The relative variation $\Delta T/T$ of sample in function of time delay between pump and probe. Pump at 2.281 eV. The red line is Auger fit. Fluence at **a)** 53 µJ.cm^{-2}, γ_{Auger}=0.0107 ps^{-1} **b)** 848 µJ.cm^{-2}, γ_{Auger}=0.0028 ps^{-1}.

We can see a discrepancy between the fit and the data for a fluence of 53 µJ.cm^{-2} (left side). This behavior is observed for all the fluences except the higher one. Indeed, it seems to fit better

at the highest fluence of 848 μJ.cm^{-2} (right side) where γ_{Auger} is found to be equal to 0.0028 ps^{-1}. More complex Auger effect resulting in N(N-1) or N^3 dependence in the rate equation have been tried without success.

Let us focus on the 848 μJ.cm^{-2} fluence case for which the model begins to fit the data. We can try to evaluate, with a very simple and naïve model, the mean distance between excitons. First, we consider excitons as "spheres" of 1.5 nm radius. Considering a hexagonal compact arrangement, it is possible to put ~5.10^{20} of these spheres in 1 cm^3 volume. The 848 μJ.cm^{-2} fluence corresponds to ~7.10^{14} excitons per cm^2. Considering that excitons are confined and uniformly distributed in the inorganic layers, it corresponds to ~4.10^{20} excitons per cm^3. This shows that the highest fluence used in these experiments leads to a situation where 80% of the available space is occupied (see **Figure 3.21**), and therefore that excitons are very close to each other. On the contrary, the lowest fluence leads to a ~1% occupation.
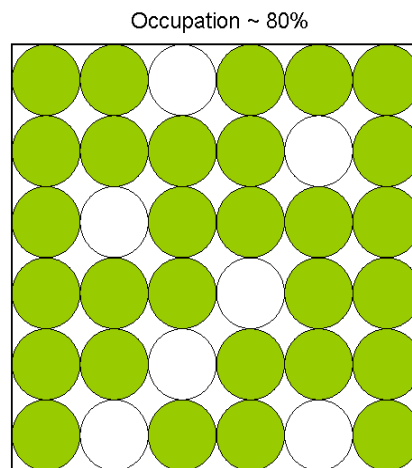
Occupation ~ 80%

Figure 3.21 Schematic representation of the 80% occupation rate of space by disks. Green disks shows occupied sites, blank one shows unoccupied sites.

The model described by the rate equation $\dfrac{dN}{dt} = -\gamma.N - \gamma_{Auger}.N^2$ considers a constant Auger rate which is characteristic of non-diffusing processes. For fully localized excitons, this process can occur when the mean distance between excitons is comparable to the exciton wavefunction extension. This is what seems to happen in the highest fluence situation, explaining the relatively good fitting. On the contrary, for low fluence, the mean distance between excitons is much bigger than the exciton wavefunction. Therefore, fully localized excitons should not interact. Nevertheless, an acceleration of the dynamics is observed even at low fluence. Therefore, the fact that the 'static' Auger rate equation does not fit the data at low

fluence shows that exciton diffusion has to be considered to explain our observations. More developments are needed to get a deeper understanding of these phenomena.

Figure 3.22a presents the variation of transmission $\Delta T/T$ as function of time delay between pump and probe pulses for fluences varying from 13 μJ.cm^{-2} to 848 μJ.cm^{-2}. We can see both the variation in the amplitude of $\Delta T/T$ and the dynamics as function of the fluence. In **Figure 3.22b** we plot the amplitude of $\Delta T/T$ as a function of the pump fluence at maximum signal (at 0 ps) and at a time delay of 50 ps. At 0 ps time delay, we see that the variation of transmission $\Delta T/T$ increases sublinearly as function of fluence. This result can be well fitted using the saturation law I/Is*1/(1+I/Is) with Is equals to 818 μJ.cm^{-2}. To understand the origin of this saturation, we may first suppose that the state at 2.818 eV is saturated by the injected carriers. However the lifetime of states at 2.818 eV is very short due to very fast intraband relaxation. Therefore it should be very difficult to saturate this transition. It is more likely that we saturate the excitonic transition from the exciton-exciton interactions. On the other hand, we see that the amplitude also saturates for longer delays (at 50 ps) as shown in **Figure 3.22b**, yet it seems to saturate faster than that at 0 ps with Is equals to 100 μJ.cm^{-2}.

(a)   **(b)**
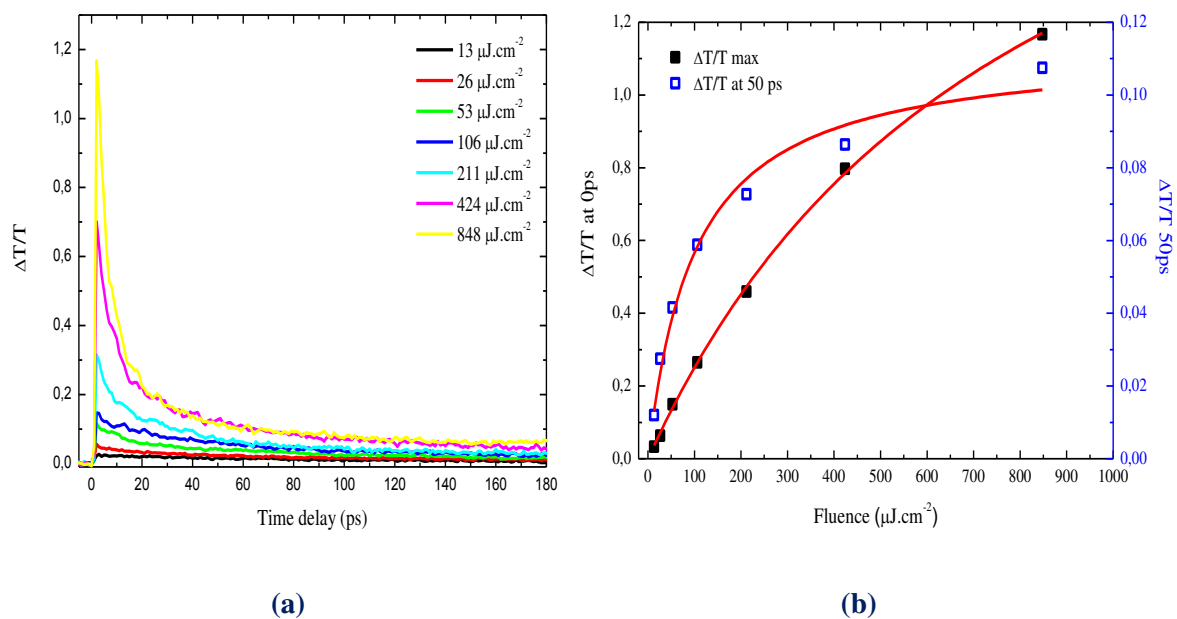
Figure 3.22 The relative variation $\Delta T/T$ of sample in function of time delay between pump and probe. Pump at 2.818 eV. **a)** Fluence varies from 13 μJ.cm^{-2} to 848 μJ.cm^{-2}. **b)** Plot of the amplitude of $\Delta T/T$ at both 0 ps and 50 ps time delay as function of the fluence. The red lines are the saturation curve fits with Is equals to 818 μJ.cm^{-2} and 100 μJ.cm^{-2} for $\Delta T/T$ at 0 ps and 50 ps respectively.

The origin of this saturation may come from a combination of two effects. First, the contributions at long time delay correspond to localized excitons. By saturating the number of exciton localization sites, their relative contribution to the pump/probe signal at the long time

delay will be less important. Moreover, similar behavior can be observed when Auger effect becomes significant. To illustrate this, we perform two different simulations. First, we plot the bi-exponential decay curves and we saturate the amplitude of the second exponential, in order to model the saturation of the localization sites. In **Figure 3.23a)**, we plot the normalized amplitude of the bi-exponential decay versus time delay. We see that the curves have almost same behavior as experimental ones. On the other hand we plot the variation ΔT as function of amplitude of injected carriers (modeled by the amplitude of the cross correlation used in the fit function of ΔT curves) for time delay at max signal (0 ps) and at 1000 ps. This result is fitted with the saturation law where Is is the saturation of the amplitude of second exponential in this case. We can see from **Figure 3.23b)** that the curve at 1000 ps saturates faster than that at 0 ps. In fact, we find that Is is equal to 34 (arb. units) for ΔT at 0 ps while equal to 10 (arb. units) for ΔT at 1000 ps.

(a)   **(b)**
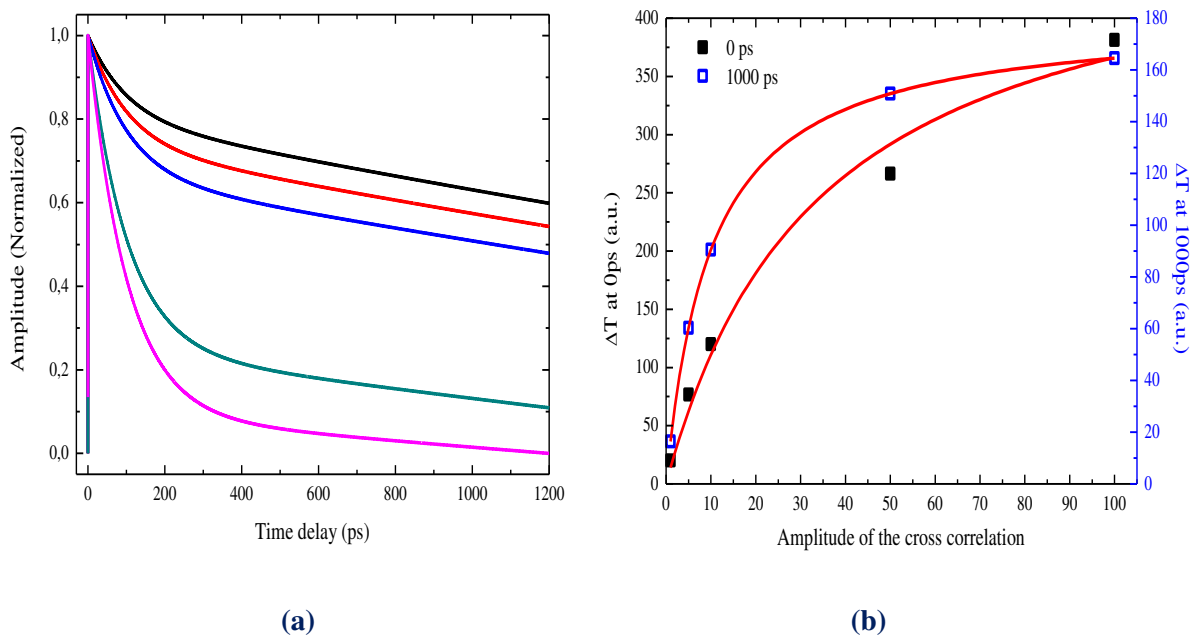
Figure3.23 a) The normalized simulated amplitude versus time delay **b)** Plot of the amplitude of $\Delta T/T$ at both 0 ps and 1000 ps time delay as function of the amplitude. The red line is the saturation curve fit.

Moreover, we have made simulations starting from the equation including γ_{Auger}. By changing the amplitude of initial conditions which must correspond to the change of exciton density, time traces are obtained in **Figure 3.24a).** We can see that same behavior of dynamics acceleration is obtained as experimental ones for time delay up to 400 ps. However at longer time delay, we can see that all curves superimposes, in contrast with experimental observations. In **Figure 3.24b)**, we plotted the amplitude of $\Delta T/T$ as a function of the initial number of excitons in these

simulations for both 0 ps and 1000 ps time delay. This result is fitted with saturation law. Again we observe that the saturation is faster at long time delay, where Is is equal to 557 for ΔT/T at 0 ps while equal to 8 for ΔT/T at 1000 ps.
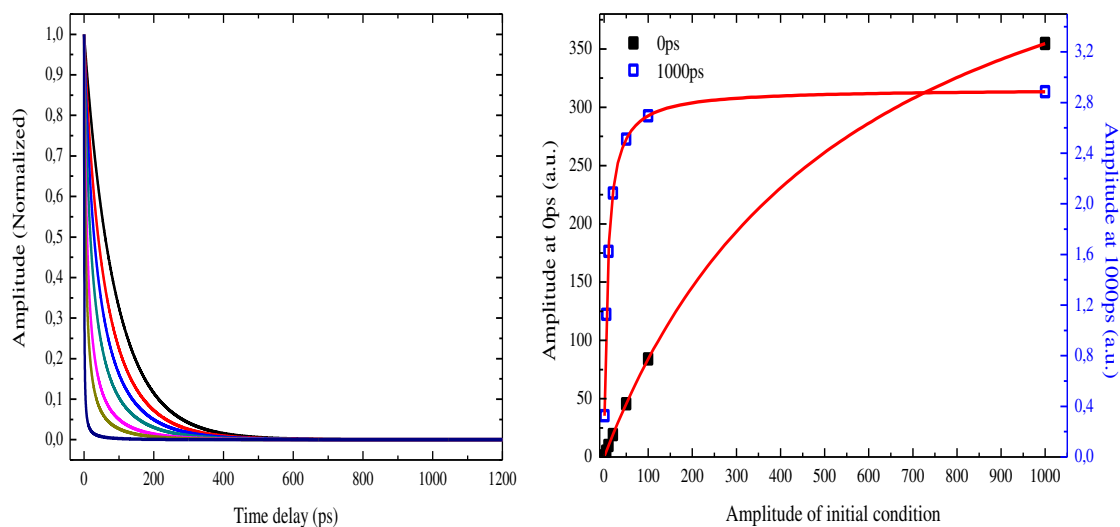
Figure3.24 a) Simulated time traces **b)** Plot of the amplitude of ΔT/T at both 0 ps and 1000 ps time delay as function of the fluence. The red line is the saturation curve fit.

To conclude, we must certainly consider both effects to explain the whole dynamics. It may also explain, in addition to diffusion phenomena, why we cannot fit the curves at low fluences with a model that does not take into account the presence of the localization sites.

3.4.   Conclusion

In conclusion, we have reported time resolved measurements performed on PEPI perovskites at room temperature for both the pump energy in resonance with that of exciton (2.397 eV) and above the 2D continuum (2.818 eV). Experiments are performed at the limit of the signal to noise ratio in order to work at the lowest carrier density. The amplitude of the transient bleaching of the exciton line normalized by the number of injected carriers is quite identical in both cases. A bi-exponential decay has been extracted from the measurements with short decay of 110 ps and a long decay tail > 5 ns, one order of magnitude higher than previous report at low temperature and high exciton densities. We interpret the lifetime of the short time decay as the one of "free exciton", whereas the long tail is attributed to localized excitons. Moreover, an ultrafast intraband relaxation has been observed.

On the other hand, the relative variation of transmission spectra in function of energy at different pump-probe delay has been analyzed using the momenta method. It has been found that the reduction of oscillator strength $\Delta f / f$ and the broadening $\Delta \Gamma / \Gamma$ are around 7.10^{-3} and 3.10^{-3} respectively, one order of magnitude smaller than in GaAs/AlGaAs quantum wells. Calculations of the contribution of both Phase Space Filling and exchange effects on the reduction of the oscillator strength are introduced. It gives a value for the reduction of the oscillator strength two orders of magnitude higher than the experimental ones. In addition, it has been demonstrated that the renormalization of the exciton wavefunction, which is interpreted as red-shift of the continuum, plays an important role in the understanding of the carrier dynamics in 2D perovskites. We have also attributed the transient broadening to collisions.

Finally, we have studied the exciton dynamics as function of injected carrier density. It has been shown that relaxation dynamics is accelerated as fluence increases. It is interpreted as the consequence of exciton-exciton annihilation assisted relaxation which can be an important step toward the use of these materials for photovoltaic applications. Moreover intraband relaxation does not vary with fluence.

Chapter 4

4. High-Q planar microcavities

Polaritons-quasiparticles are the eigenmodes in a semiconductor cavity where excitons are coupled to photons in the case of the strong coupling regime. Over the last 20 years, polaritons have emerged as an important research topic for both fundamental and applied physics. On the former aspect, it provides a new insight for studying the physics of out of equilibrium Bose-Einstein condensate. On the latter aspect, we see the development of a new generation of optical devices based on condensation of polaritons and propagation of these polariton condensates in engineered confined microstructures [110]. From the point of view of materials, most studies of polaritons use inorganic InAs/GaAs based emitters (semiconductor Quantum Dots and Quantum Wells) in high Q-factor planar microcavities at low temperatures. However in order to raise the working temperature of these polariton-based devices up to room temperature, a big effort has been done to work on alternative semiconductors presenting large exciton binding energies and oscillator strengths, such as GaN [7, 8], ZnO [9], organic [10, 11] and hybrid organic-inorganic materials [13-22].

In the last few years, vertical microcavities containing hybrid organic-inorganic perovskite thin layer, working in the strong coupling regime at room temperature, have been realized. In this chapter we will first present the optical properties of these microcavities, named as standard microcavities, containing the layered perovskite semiconductor: $(C_6H_5C_2H_4NH_3)_2PbI_4$ (PEPI) described in details in chapter 2. Two difficulties are present in such microcavities. Firstly, the improvement of the quality factor by monolithic deposition of a dielectric mirror directly on the perovskite layer, is difficult. Secondly, to reach non linear thresholds, high excitation densities are needed. Unfortunately, perovskite materials exhibit photobleaching that prevents to reach these thresholds. In this chapter, we will first present a new assembly technique making use of top-dielectric mirror migration in liquid. Then, microphotoluminescence experiments both in cw and pulsed regime will be described. Finally,

to improve the material photostability, a new perovskite: p-fluorophenethylamine tetraiodoplumate, whose chemical formula is $(pFC_6H_5C_2H_4NH_3)_2PbI_4$ (abbreviated as 4FPEPI) has been synthesized and included in a polymer matrix of PMMA at different concentrations. Photobleaching studies of this new material will be presented at the end of this chapter.

4.1.   Standard PEPI-based microcavity

A standard microcavity is composed of a 50 nm PEPI layer deposited on Layertec dielectric mirror by spin coating. A 100 nm phase layer of PMMA is then deposited by spincoating on the PEPI layer. Finally, the microcavity is closed with a top metallic mirror. Details on protocol of fabrication are presented in chapter 2. Although strong coupling regime at room temperature has been previously demonstrated in such cavities by G. Lanty, it was necessary to learn fabrication and characterization techniques of microcavities as a first step in my work in the domain of microcavities. In this section, we will present the optical properties: angle resolved reflectivity and photoluminescence measurements of standard PEPI-based microcavities.

4.1.1. Angle resolved reflectivity measurement

This section presents the study of reflectivity, performed by using the experimental setup already described in paragraph 2.2 of chapter 2 for PEPI microcavity (standard one). As described in Chapter 2, the unbalanced structure of this microcavity (bottom mirror is much more reflective than top mirror) allows to consider the reflectivity spectra as a direct image of absorption spectra, which is the only physical data that allows to unambiguous distinguish between strong and weak coupling.

Figure 4.1 presents the reflectivity spectra of the studied microcavity for different incident angles. Each spectrum shows the presence of two dips. When the incident angle increases, the low energy dip shifts towards high energy dip which stays unchanged in a first step. Upon approaching the lower vicinity of exciton energy, the position of low energy dip stabilizes and the energy shift is transmitted to high energy dip, which is the characteristic of an anticrossing.

For the microcavity studied, it appears for small angles of incidence that the low energy dip is stronger than that of the high energy one. When the angle of incidence increases, this finding is reversed since the intensity of low energy dip decreases as it approaches the exciton energy of PEPI, while at the same time the intensity of the high energy dip increases. Thus, transfer of intensity occurs between low and high energy dips.

The anticrossing and transfer in intensity observed between the two dips are two signatures of the strong coupling regime in microcavities, which was described in paragraph 1.7 of chapter 1. Indeed, the anticrossing comes from raising degeneracy caused by the coupling between excitons of PEPI and photons of cavity modes while the transfer of intensity corresponds to changes in photonic and excitonic parts of the two cavity polaritons.

The energy positions of the two polaritons are plotted (red and black squares) as function of $k_{//}$ as shown in **Figure 4.1**. The relationship between the angle of incidence and the wavevector in the layers plane of polaritons is given by:

$$k_{\square} = \frac{E}{c\hbar} \sin \theta$$
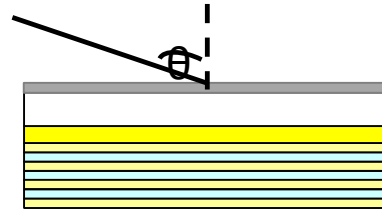
where E is the energy of the cavity polariton considered, $\hbar$ is the reduced Planck constant and c is the speed of light. Moreover, these experimental data are fitted by a two-level model in which the dispersion of the cavity mode is of the form:

$$E_{ph}\left(k_{\square}\right) = \sqrt{\left(E_0\right)^2 + \left(\frac{c\hbar k_{\square}}{n_{eff}}\right)^2} \tag{4.1}$$

with E_0 the energy of cavity mode at $k_{\parallel}$=0 and n_{eff} is the effective index taking into account the optical indices of the different layers of materials experienced by electric field. E_0, n_{eff}, coupling energy V and exciton energy E_{ex} are taken as fitting parameters of the two level model previously presented in chapter 1. The dispersion curves of the two polaritons obtained with this two level model are plotted in red solid line and the dispersion curves of the uncoupled exciton and cavity modes are plotted in black dash line in **Figure 4.1**.

For our studied microcavity, we get the following fitting parameters: n_{eff} = 1.81, E_{ex} = 2.378 eV, E_0 = 2.15eV, and V=60 meV. Coupling energy obtained corresponds to a Rabi splitting of about 120 meV. Note also that the obtained value of E_{ex} is closed to 2.398 eV, the energy position of the excitonic peak obtained from OA spectrum of PEPI. We conclude that the strong coupling regime occurs in this microcavity and that the two dips result from the lower and upper polaritons.
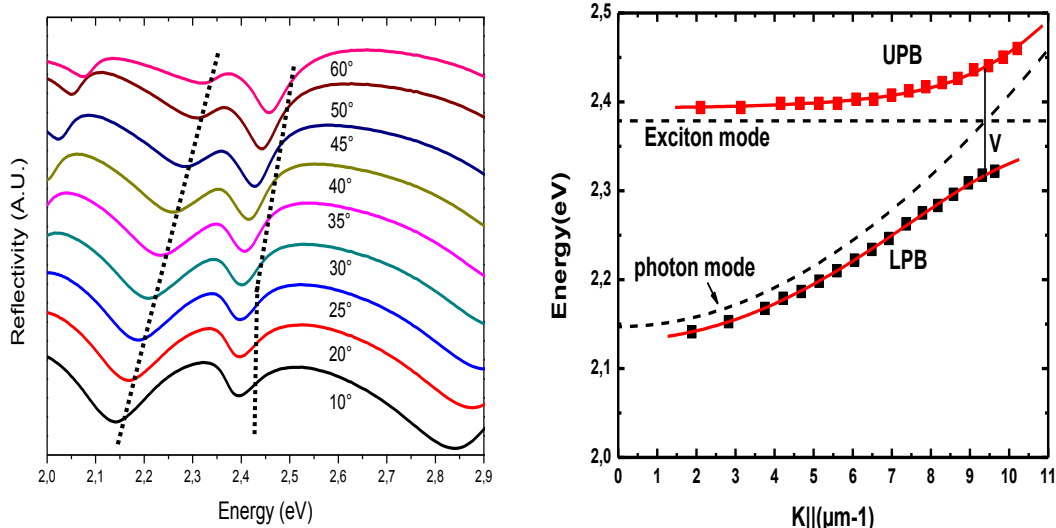
Figure 4.1 (a) Reflectivity spectra of the microcavity for several angles of incidence at room temperature. The dashed lines are guides to the eyes. **(b)** Dispersion of the upper polariton branch (UPB) and lower polariton branch (LPB). The squares are experimental data. The solid lines are fits from two level system. The dash lines represent the dispersion of uncoupled photon cavity mode and exciton mode.

4.1.2. Angle Resolved Photoluminescence measurements

To demonstrate the strong coupling unambiguously, photoluminescence experiments have to be performed in addition to the reflectivity experiments. In order to observe the emission of the mixed polaritonic states, angle-resolved photoluminescence experiments have been performed at room temperature by G. Lanty [13]. A 405 nm diode laser beam is focused on the microcavities through the metallic mirror, at normal incidence, and the photoluminescence spectra are recorded for various detection angles. The excitation density was chosen to be low enough to limit the degradation of the PEPI layer. **Figure 4.2** shows the photoluminescence spectra obtained for standard microcavity in linear scale (left) and logarithmic scale (right) for different angles of detection, ranging from 5°to 35°.The upper part of the graph shows the PL spectrum acquired before microcavity is completed by silver mirror.

For lower angles, the PL spectra of the microcavity are composed of two peaks: the emission peak corresponding to the lower energy polariton branch and a second peak at higher energy. The spectral position of this second peak is independent on detection angle and coincides with the emission peak of the non closed microcavity. This second peak, whose energy doesn't match with any dips in the reflectivity spectra, is regarded to be the photoluminescence of the non-coupled excitons of PEPI layer. It is also possible to distinguish on the logarithmic scale a very slight shoulder on the high energy side of uncoupled perovskite

peak, which doesn't appear in the emission spectra of half-microcavities without silver mirror. It seems coherent to attribute this shoulder to the emission of higher energy polariton branch. Gradually, as the angle of detection increases, the shoulder corresponding to UPB seems to disappear, while the emission of LPB strengthens to be as intense as the one of uncoupled perovskite peak. The variation of the low energy photoluminescence peak as a function of the detection angle coincides with the dispersion relation of the low energy polaritonic branch. This clearly indicates that this photoluminescence peak arises from the polaritonic emission and confirms the demonstration of the strong coupling regime in the microcavities containing perovskite thin layers.
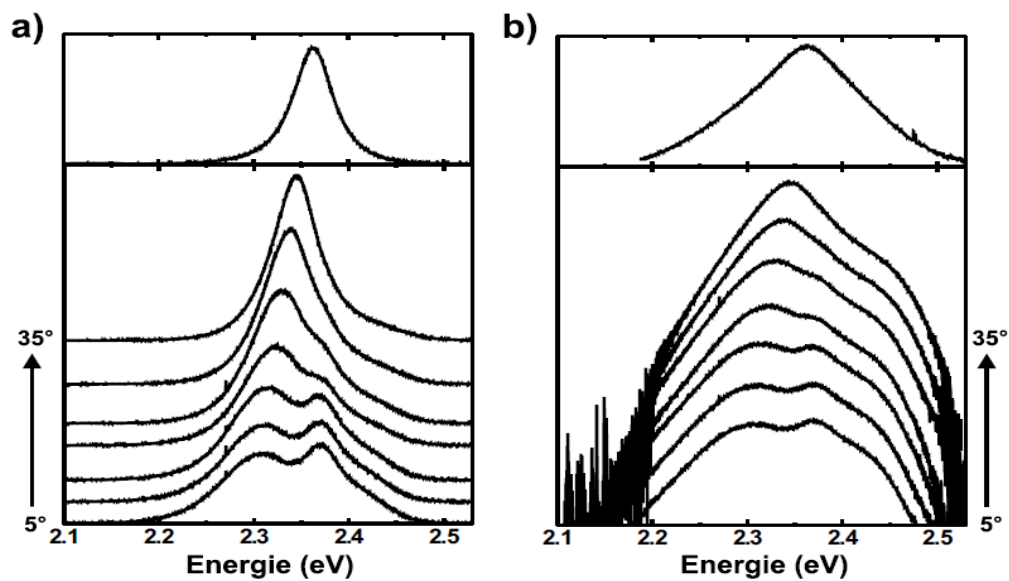
Figure 4.2 Photoluminescence spectrum of « standard » PEPI based-microcavity studied for different detection angles in a) linear scale and b) logarithmic scale. On the upper part of the two graphs, a photoluminescence spectrum acquired before the microcavity is completed by the silver mirror.

4.1.3. Quality factor of a microcavity

Quality factor is an important characteristic parameter that identifies the cavity quality. It is a dimensionless parameter that corresponds to the average number of reflections of a photon before it leaves the cavity. Generally the quality factor Q of the cavity is defined as:

$$Q = \frac{\lambda_c}{\Delta\lambda_c}, \tag{4.2}$$

Where λ_c is the wavelength of cavity photon mode and $\Delta\lambda_c$ is the spectral width of cavity photon mode. Q is related to photon lifetime τ_{ph}, the time during which the photon stays in the cavity. It can be expressed as:

$$\tau_{ph} = \frac{\hbar Q}{E_{ph}} \qquad (4.3)$$

The quality factor Q of the standard cavity can be roughly estimated from the characteristics of the LPB dip in reflectivity since the LPB is more photon-like at low angles: Q = 20 for the cavity of **Figure 4.1**. It has been shown by S. Faure that the quality factor of ZnO-based microcavities changed from 60 to 120 by changing the nature of the top mirror from metallic mirror (Al mirror) to dielectric mirror (5 pairs of Si_3N_4/SiO_2 while keeping the same nature of bottom mirror (AlN/AlGaN dielectric mirror) [106]. This is due to the fact that the reflectivity R_2 of the top mirror is 55% and 68% for Al mirror and Si_3N_4/SiO_2 dielectric mirror respectively. Moreover, the reflectivity coefficient R_2 of Si_3N_4/SiO_2 dielectric mirror reaches 95% by increasing the number of pairs in the dielectric mirror (11 pairs of Si_3N_4/SiO_2 instead of 5 pairs). Thus, an increase of the number of pairs in dielectric mirror results in higher mirrors reflectivity and thus in higher quality factor microcavities. In the following section, we present the technique used for the deposition of the dielectric mirror on the perovskite layer, in order to increase the quality factor of perovskite based microcavities.

4.2. High-Q planar perovskite based microcavity

In order to study the stimulated polaritonic effects, a larger quality factor (typically > 100) is required to increase the lifetime of polaritons. This can be achieved by using highly reflective dielectric Distributed Bragg Reflectors (DBRs) as top mirrors instead of semitransparent metallic mirrors. Unfortunately, the demonstration of such high-Q microcavities is complicated by the difficulties associated with fabricating highly reflective dielectric DBRs on top of a fragile molecular material, which is generally very sensitive to any temperature increase, mechanical stress or chemical reactions induced by standard dielectric deposition processes. As a consequence, new fabrication methods have to be developed. In the following, we will present a new assembly technique making use of top-dielectric-mirror migration in a liquid developed in our group by Z. Han in collaboration with S. Bouchoule at LPN [107].

4.2.1. Technique of Fabrication

The technique of top-dielectric mirror migration is schematically depicted in **Figure 4.3**. The perovskite layer having an approximate thickness of 60 nm is spin-coated on top of the bottom mirror. The bottom mirror consists of 11 pairs of SiN_x/SiO_2 layers deposited on a fused silica substrate by Plasma Enhanced Chemical Vapor Deposition. And then the $\lambda/2$ optically thick cavity is completed by a sputtered SiNx phase layer. This half-cavity structure is referred to as the destination sample in the following. On the other side, the top dielectric Bragg mirror is first deposited on a silicon host substrate preliminarily covered with a polymer sacrificial layer. This polymer is chosen to be stable under high temperature (up to 200°C) and robust against typical dielectric mirror deposition conditions (sputtering or vacuum evaporation). In this study, the top Bragg mirror is deposited onto the sacrificial layer by vacuum evaporation, and consists of eight pairs of quarter-wavelength YF_3/ZnS layers (well adapted to the visible spectral range). It is completed by a thin Ti/Ni bilayer acting as a stress compensator. The Ti/Ni layer thickness is adapted to compensate for the internal strain of the dielectric multilayer pile, therefore to avoid the rolling-up of the mirror after its release from the silicon substrate as shown in step 2 of **Figure 4.3a**. In order to proceed to the top mirror assembly, the host substrate is dipped in a solvent (EBR PG by Micro Chem) that dissolves the sacrificial layer, releasing the top mirror as shown in step 2 of **Figure 4.3a**. When the top mirror is completely released, floating in the solution, the solvent is expelled from the recipient, and the latter is gradually filled by a non destructive liquid to the active material (toluene solvent for the perovskite material). The released top mirror is positioned in the liquid above the immersed destination sample, and the liquid is gradually evacuated so that the top mirror lies flat onto the surface of the destination sample as shown in step 3 of **Figure 4.3a**. Moreover, these overall details of the release and migration steps of dielectric mirror in liquid are presented in **Figure 4.3b**. The whole cavity structure is lastly annealed on a heating plate at a temperature of about 90°C in order to evacuate the residual liquid and to firmly attach the two surfaces. The sample is then mounted up-side-down on a copper plate with the fused silica substrate side outwards.
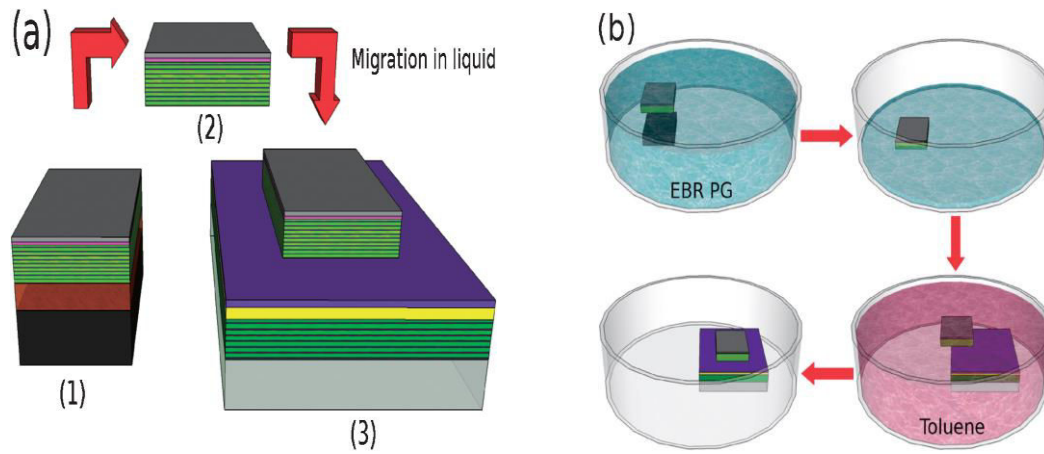
Figure 4.3 (a) Top-dielectric-mirror migration process: (1) deposition of the Bragg mirror (green) and the metallic bilayer (magenta and dark gray) on silicon host substrate (black) with sacrificial polymer layer (brown), (2) release of the mirror by dissolving the sacrificial layer, (3) evacuation of the solvent and positioning of the released mirror onto the surface of the destination sample with the active layer (yellow), phase layer (violet), and bottom dielectric Bragg mirror (green) on fused silica substrate (light gray).(b) Detailed release and migration steps of the dielectric mirror in the liquid.

4.2.2. Angle-resolved reflectivity measurement

I have performed angle-resolved reflectivity measurement on this perovskite-based microcavity with F. Boitier (ATER in the team). **Figure 4.4** presents the reflectivity spectrum measured at normal incidence. We can distinguish three distinct dips at 2.1, 2.2, and 2.4 eV, corresponding to three polariton branches (PBs): the low (LPB), the middle (MPB), and the high (HPB) energy polariton branches respectively. The three polariton branches arise from the coupling of the perovskite exciton to both the cavity mode and the Bragg mode just at the lower energy edge of the stop band of the bottom mirror. Such coupling to the Bragg mode is possible, despite the relatively wide stop-band of this mirror (the stop band of bottom mirror is 470 meV wide coming from a refractive index contrast of about 0.38), owing to the large exciton binding energy of perovskite. Such a kind of coupling has also been reported for ZnO-based microcavities [106].
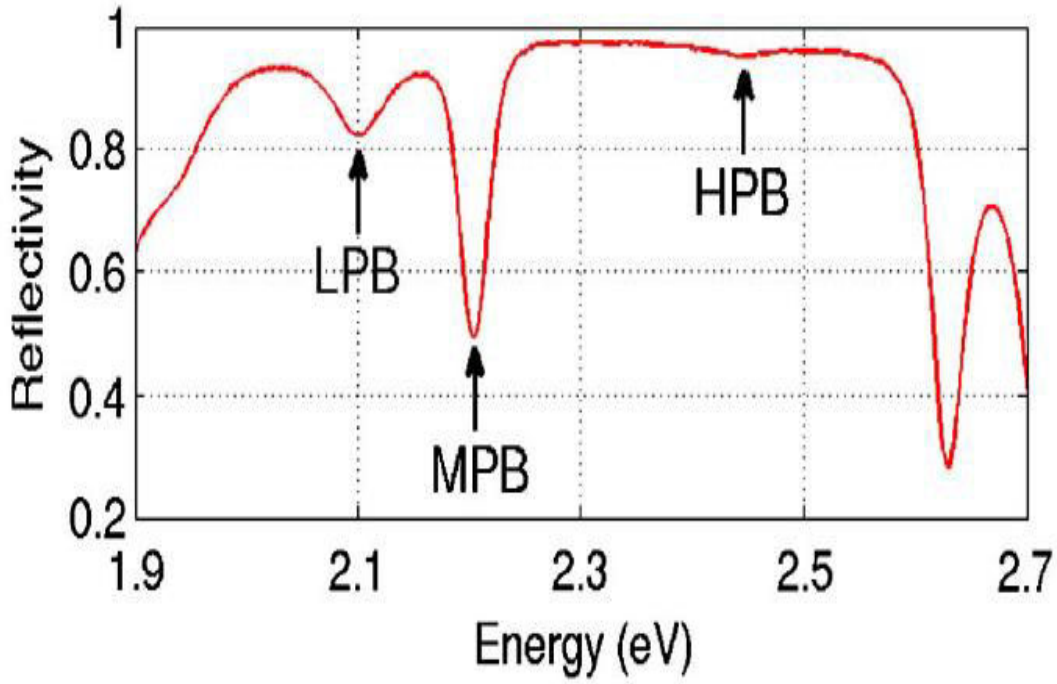
Figure 4.4 Measured reflectivity at normal incidence. The three dips correspond to the high (HPB), middle (MPB), and low (LPB) polariton branches, respectively.

The three coupled modes are further investigated by angle-resolved reflectivity measurements, as shown in the right part of **Figure 4.5**. The white, green, and red dashed curves corresponding to LPB, MPB, and UPB respectively, are fitted from a quasiparticle model with three different levels, describing the interactions between two photon modes (cavity and Bragg photon modes) with one exciton.

$$H = \begin{pmatrix} E_{cav} & 0 & V_{PE} \\ 0 & E_{Bragg} & V_{BE} \\ V_{PE} & V_{BE} & E_{ex} \end{pmatrix} \qquad \textbf{(4.4)}$$

E_{ex} is the energy of perovskite exciton, fixed at the value E_{ex}= 2.39 eV, E_{Bragg} is the energy of the Bragg photon mode and E_{cav} is the energy of the cavity photon mode. The two parameters, V_{PE} and V_{BE} are the interaction potentials between the exciton and the cavity and Bragg photon modes respectively. We also show in the left part of **Figure 4.5,** the results from a Transfer Matrix Model (TMM) simulation done by Z. Han and F. Boitier. The complex refractive index values used in the simulations are those estimated from spectroscopic ellipsometry measurements for the different materials. As can be observed from **Figure 4.5**, a very good agreement is found between the experiments and the simulations for a 65 nm thick perovskite layer.

An estimate of the quality factor can be derived from the Full Width at Half Maximum of the middle polariton branch at normal incidence, since it is dominated by the cavity photonic mode and may be considered to be the closest measured value of quality factor. The experimental results of **Figure 4.5** lead to an estimated quality factor of 76. It is close to the value of 88 deduced from the calculated spectra (left part of **Figure 4.5**) and is about three times higher than the quality factor estimated for the cavities where a semitransparent metallic mirror was used as the top mirror. However, it should be noted that, even though the MPB is dominated by cavity photonic mode at normal incidence, the broadening related to the exciton coupling cannot be neglected due to the strong exciton broadening at room temperature.
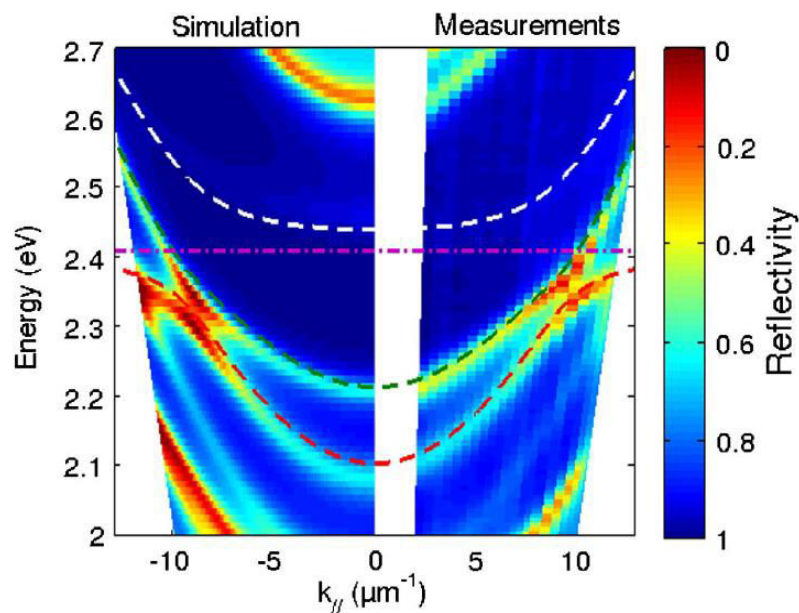
Figure 4.5 Angle-resolved reflectivity of the cavity (the jet colormap from red to blue represents the reflectivity value from 0 to 1). Left: Simulation. Right: Measurements. White, green, and red dashed curves: fitted HPB, MPB, and LPB, with a three-level model [16]. Magenta dash-dotted line: uncoupled exciton energy.

4.2.3. Validation of the Migration technique

In order to validate the migration technique, two passive cavities have been fabricated using the standard monolithic approach and the top-dielectric-mirror migration approach. Passive cavities are cavities with the fragile perovskite layer replaced by a dielectric HfO_2 layer of similar refractive index. The cavity structure consists of: bottom mirror (11 pairs of HfO_2/SiO_2 layers on fused silica substrate), half-wavelength cavity layer (HfO_2), and top mirror (8 pairs of YF_3/ZnS layers with a thin Ti/Ni bilayer). All layers are deposited using electron-beam vacuum evaporation. In the case of the monolithic cavity, the YF_3/ZnS top mirror is directly evaporated onto the destination sample composed of bottom mirror and cavity layer.

The cavity structure is designed to obtain a central resonance frequency at about 520 nm (close to the perovskite emission wavelength).
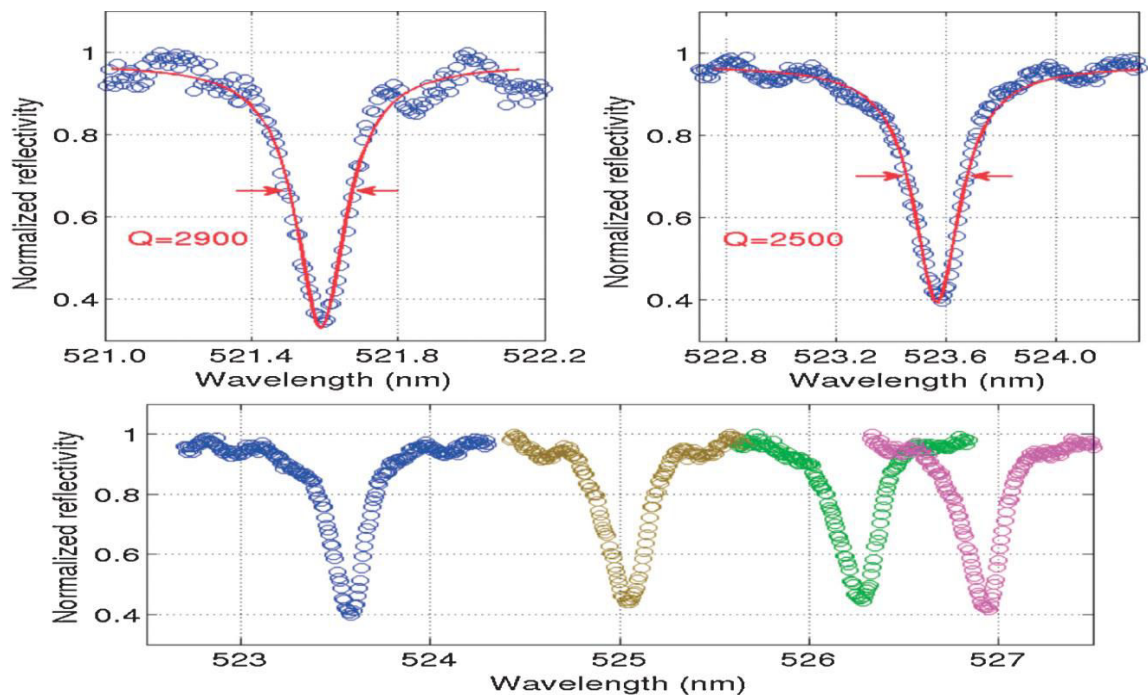
Figure 4.6 Measurements performed on the passive microcavities: (a) monolithic approach (Q =2900), (b) top-dielectric mirror migration approach (Q =2500). The blue open circles are the measured data, and the red plain curve is the Lorentzian fit. (c) The colorful open circle curves are the measurements performed on different positions of the microcavity assembled with top-mirror migration.

Figures 4.6(a) and (b) show the microreflectivity (spot diameter 2 μm) spectra measured at normal incidence for the two cavities. The measured linewidth of the resonant cavity mode corresponds to a Q-factor of 2500 (respectively 2900) for the cavity fabricated using the top-mirror migration approach (respectively the standard monolithic approach). Measurements have been performed at many different positions on the samples and confirm that both samples are fairly homogenous, as illustrated in **Figure 4.6(c)** for the sample assembled with top-mirror migration. The Q-factors obtained by both fabrication methods are very similar, which validate the top-mirror migration technique.

4.2.4. Microphotoluminescence measurements

4.2.4.1. *Microphotoluminescence measurements performed at LPN*

In this section we will show μPL measurements performed on this kind of cavity at room temperature. Experiments were performed by H. NGuyen at LPN (J. Bloch team) using a

confocal setup where the excitation laser beam (energy of 3.06 eV) is focused to a 2 µm diameter spot by a microscope objective. The emission is then collected by the same objective and detected by a CCD camera through a spectrometer as described in chapter 2. This measurement is performed on two cavities containing 60 nm PEPI active layer fabricated using the monolithic and mirror migration approaches. Both cavities have a similar structure. It consists of: bottom mirror (11 pairs of SiNx/SiO$_2$ layers on fused silica substrate), PEPI layer, half wavelength cavity layer (SiNx), and top mirror (8 pairs of YF$_3$/ZnS layers with a thin Ti/Ni bilayer). The cavities are expected to operate in the strong coupling regime owing to the large oscillator strength of the perovskite exciton. In the monolithic case (see **Figure 4.7(a)**), a strong emission line at about 2.36 eV is observed, which can be attributed to non-coupled perovskite excitons, and the anticrossing of the polariton branches is not observed. **Figure 4.7(b)** shows the photoluminescence emission spectrum of monolithic cavity at k‖ = 0. The Full Width at Half Maximum (FWHM) of the photonic mode (energy of 2.247 eV) is measured to be 45 meV. This corresponds to an equivalent Q-factor of 49.

On the other hand, strong photon–exciton coupling is clearly evidenced in microcavity using the top dielectric-mirror migration approach as shown in **Figure 4.8(a)**. The measured dispersion is in good agreement with the one deduced from angle resolved reflectivity of **Figure 4.5**. The luminescence intensity is dominated by the MPB and the signal is strongest at k‖ = 0, thus highlighting efficient relaxation of polaritons along the MPB. The HPB is not observed in luminescence because of fast polariton relaxation assisted by optical phonons toward lowest energy states. Although the relaxation in the LPB is extremely inefficient due to its negligible exciton weight, weak emission from the LPB can be resolved thanks to its very high photon component inherited from the Bragg mode. Importantly, in contrast with the photoluminescence obtained from our previous cavity design using semitransparent top metallic mirror, no signature of noncoupled perovskite exciton is observed.
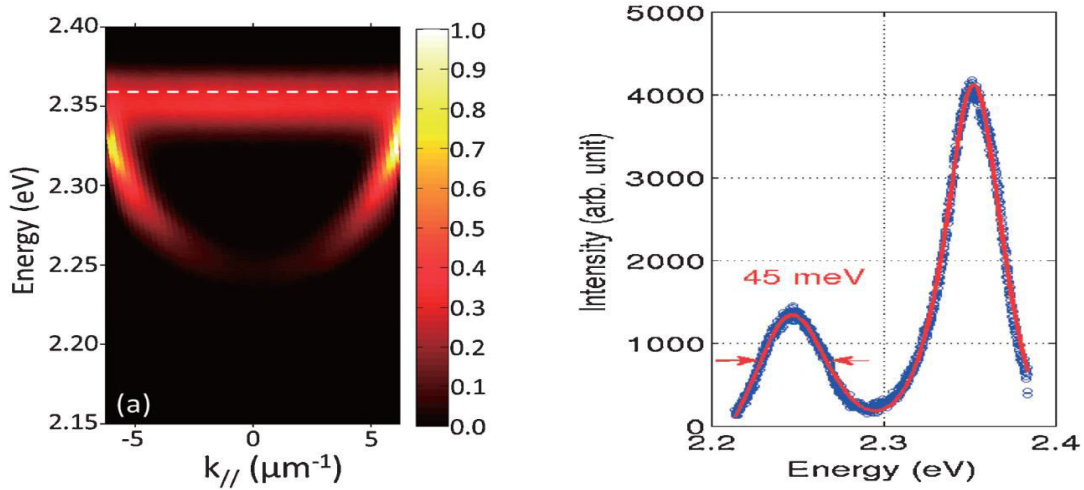
Figure 4.7 Monolithic approach **a)** μPL spectrum of the cavity in reciprocal space b) spectrum profile of cavity at k∥= 0 (Q= 49). The blue open circle curve is the measurement and the red plain curve is the Lorentzian fit of the measurement.

Figure 4.8 (b) shows the photoluminescence emission spectrum at k∥ = 0 for the microcavity assembled by the top mirror migration approach, the FWHM of the LPB at k∥ = 0 is measured to be 26 meV, corresponding to a Q-factor of 86. This value is 4.3 times larger than the one obtained from standard cavities operating in the strong coupling regime in **Figure 4.1.** The improvement is obviously attributed to the higher reflectivity of the dielectric Bragg mirror, compared with the semitransparent metallic top mirror used for the standard cavities.

Figure 4.8. Top-dielectric-mirror migration approach (a) μPL spectrum of the cavity in reciprocal space. The green and red dashed curves are the fitted dispersions of LPB and MPB obtained from the reflectivity measurements of Figure 4.5. b) Spectrum profile of cavity at k∥ = 0 (Q= 86). The blue open circle curve is the measurement and the red plain curve is the Lorentzian fit of the measurement.

4.2.4.2. Microphotoluminecence measurements performed at LAC-ENS Cachan:

The previous µPL results on PEPI based microcavity using migration technique in liquid were performed by the group at LPN just after the microcavity fabrication. The excitation laser used in these measurements was a cw 405 nm diode laser (3.06 eV). Lateron, the µPL setup has been mounted at ENS Cachan as described in details in section 2.4 of chapter 2 in order to be able to use the pulsed laser, which allows to reduce the heating (related to average power), and to reach high peak powers necessary to reach the non-linear regime. In the following, a set of µPL measurements using both continuous wave laser and femtosecond laser are presented. Note that these measurements are performed at the end of the thesis, which is after around two years of the fabrication of the studied microcavity. Moreover, due to technical reasons, the cavity was attached to silicon wafer from its top mirror side. So, measurements were performed in the case where the excitation laser is sent to the sample from its bottom mirror.

In a first step, we have performed µPL measurements using continuous wave (cw) laser in order to compare them with those performed at LPN as shown in **Figure 4.8**. **Figure 4.9** shows the emission spectrum of the microcavity assembled by the top mirror migration approach using 405 nm cw diode laser (3.06 eV) as excitation laser. The µPL emission measured in reciprocal space is displayed in **Figure 4.9a)**. Moreover, we can see from **Figure 4.9b)** a strong emission at 2.28 eV which can be attributed to the MPB. A mismatch between the energy of highest signal in real space and k-space is observed. This is due to both the size of the lenses and of the slit of spectrometer, which affect just the k-space measurements and so forbide to have all "$k_{\parallel}$". In **Figure 4.9a)**, we see that higher signal is at high $k_{\parallel}$, so if we would be able to measure higher k we should observe higher signal at higher energy. The FWHM of MPB at $k_{\parallel}=0$ is measured to be 91 meV. This value is 3.5 times larger than the value obtained previously under same conditions but just after fabrication.

We have also performed several measurements using cw laser but on different points on the sample. We present here four of them. **Figure 4.10a)** presents the µPL emission of the corresponding four points measured in reciprocal space. Moreover, **Figure 4.10b)** presents the spectrum profile of the cavity at $k_{\parallel}=0$ for the four different points on the sample. We can see clearly that the energy of emission peak varies between 2.18 eV and 2.34 eV. The FWHM at $k_{\parallel}=0$ is 123 meV for point 1, 167 meV for point 2, 90 meV for point 3 and 229 meV for point 4. The sample is around two years old and many measurements have been performed on it such as measurements as function of temperature and power. All these studies may have induced damages on the sample thus explaining the broadening of the polariton modes.

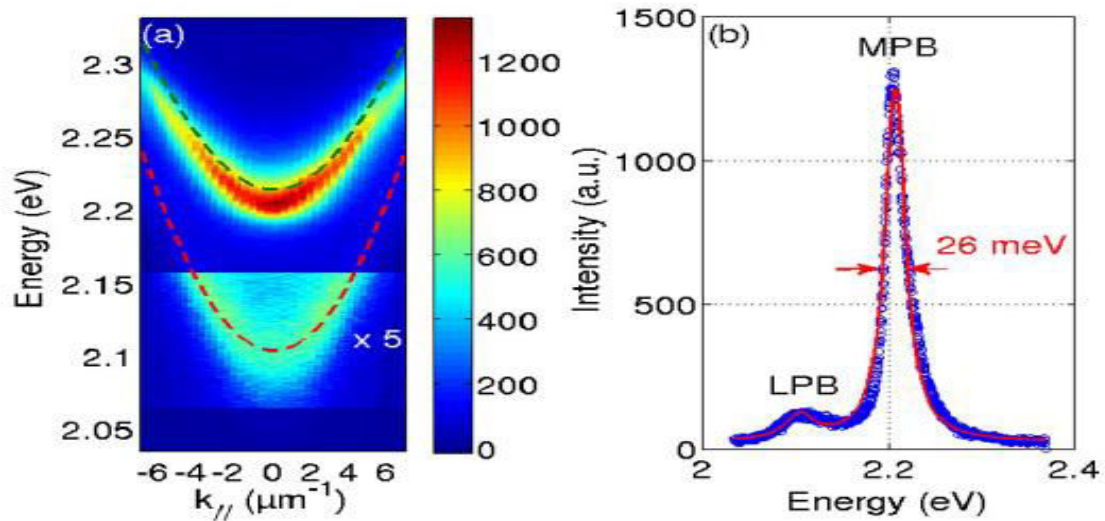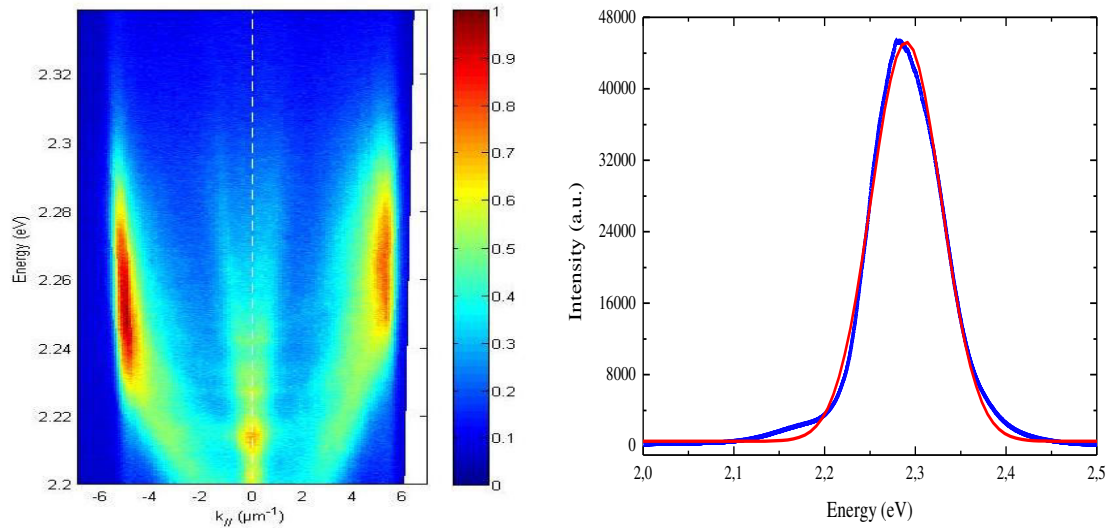**Figure 4.9: (a)** μPL spectrum of the cavity in reciprocal space. **(b)** Spectrum profile of the cavity at $k_{||}$=0. The blue line is the measurement and the red line is the Gaussian fit of the measurement.

point1

point2
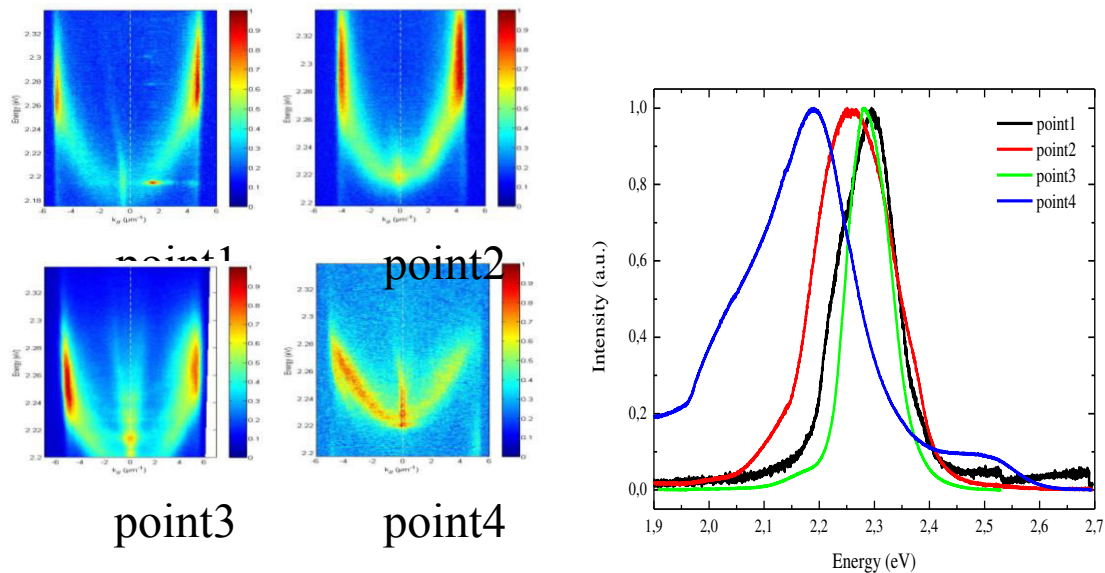
point3

point4

Figure 4.10: (a) μPL spectrum of the cavity in reciprocal space corresponding to four different points on the sample. **(b)** Spectrum profile of the cavity at $k_{||}$=0 for the four different points on the sample.

Similar results have been found using 355 nm picosecond laser. This laser is set to work at 1kHz repetition rate, providing pulses of duration 0.3 ns. This laser is focused to a 2μm spot diameter by microscope objective on the microcavity. The optical elements were placed in a way where we can change easily the excitation laser from continuous wave laser to the picosecond one as shown in section 2.4 of chapter 2. This study is performed on point 1 shown in **Figure 4.10**. **Figure 4.11a)** and **Figure 4.11b)** show the μPL emission measured in k-space and real space respectively. We can see an emission at around 2.258 eV, with FWHM at $k_{||}$=0

measured to be 112 meV which is comparable to the MPB emission observed in cw experiments (see **Figure 4.10b)**, black curve).
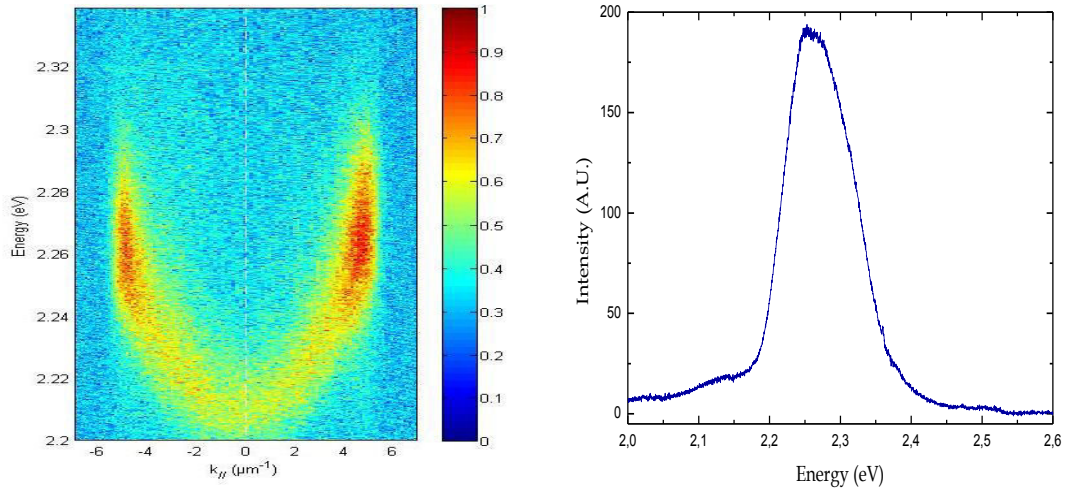
Figure 4.11: Point1 Using 355 nm picosecond laser: a) μPL spectrum of the cavity in reciprocal space, (b) Spectrum profile of the cavity at $k_{||}$=0.

Figure 4.12 a) presents the μPL spectra recorded as a function of power performed on point 1 using the 355 nm picosecond laser. Using this laser, only MPB mode is observed. An increase of the MPB signal as well as a redshift of its spectrum is observed while increasing the pump power. Moreover, the integrated intensity of the cavity mode increases superlinearly with the power (**Figure 4.12 b)**). This may be a first indication of the appearance of non-linear effects in these cavities. Unfortunately, we had a limited access to this laser, and no more experiments have been performed in this configuration.

Figure4.12: Point1 Using 355 nm picosecond laser: **(a)** Spectrum profile of the cavity at $k_{||}$=0 as function of power. (b) Integrated intensity of cavity mode as function of power.

On the other hand, we have performed µPL measurements using femtosecond laser of wavelengths 405 nm and 440 nm originated from a Ti-sapphire oscillator producing 100 fs pulses with 1kHz repetition rate and followed by an optical parametric amplifier. First, 405 nm femtosecond pulses are focused on a 2 µm spot diameter by microscope objective on the microcavity. This study is performed on point 2 shown in **Figures 4.10**. For point 2 and just after its emission measurement performed using cw laser, we changed the cw laser to the 405 nm femtosecond one; then real space and k-space measurements were performed. **Figures 4.13 a)** and **(b)** show the µPL emission measured in reciprocal space, while **Figure 4.13 c)** shows the spectrum profile of the cavity at $k_{||}=0$. We can distinguish two peaks, high peak at around 2.13 eV and a smaller one at around 2.313 eV which can be attributed to Bragg mode and cavity mode respectively. Moreover, we can see from **Figure 4.13 a)** and **b)** that the Bragg mode is localized whereas the cavity mode has a dispersion form.

(a)   **(b)**

(c)

Figure 4.13 Point 2 Using femtosecond laser: µPL spectrum of the cavity in reciprocal space; showing **(a)** Bragg mode(left side) and **(b)** cavity mode (right side). **(c)** Spectrum profile of the cavity at $k_{||}=0$.

Similar to points 1 and 2 and just after the emission measurement performed using cw laser on point 3 shown in **Figure 4.10**, we changed the laser to 440 nm femtosecond one working in same conditions as 405 nm femtosecond laser; then real space and k-space measurements were performed. **Figure 4.14 c)** shows the spectrum profile of the cavity at $k_{||}=0$. We can distinguish two peaks, high peak at around 2.13 eV and a smaller one at around 2.29 eV which can also be attributed to Bragg mode and cavity mode respectively. The μPL emission measured in reciprocal space is displaced in **Figure 4.14 a)** and **b)**. We can see that the Bragg mode is localized and that the cavity mode has a dispersion form similar to the results found using 405nm femtosecond laser.

(a)   (b)

(c)

Figure 4.14: Point 3 Using femtosecond laser: μPL spectrum of the cavity in reciprocal space; showing **(a)** Bragg mode (left side) and **(b)** cavity mode (right side). **(c)** Spectrum profile of the cavity at $k_{||}=0$.

On the other hand, **Figure 4.15 a)** shows the μPL spectra recorded as function of power performed on point 2 using 405nm femtosecond laser. **Figure 4.15 b)** presents the integrated

intensity of both Bragg and cavity modes as a function of power. We can see that the integrated intensity of the Bragg mode increases as power increases from 0.1µW to around 1.5µW and then decreases linearly with power whereas the integrated intensity of the cavity mode saturates as power increases.
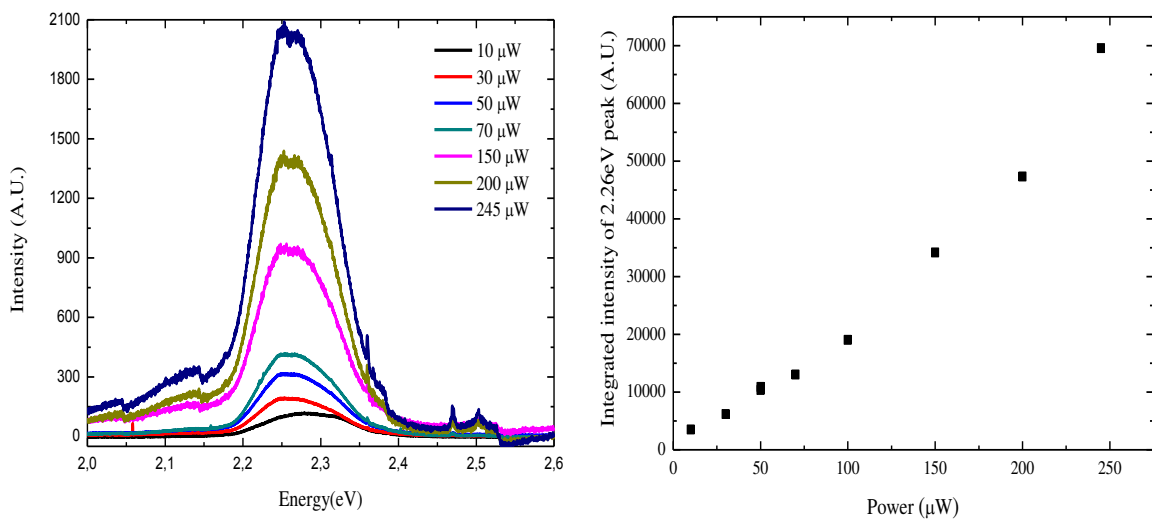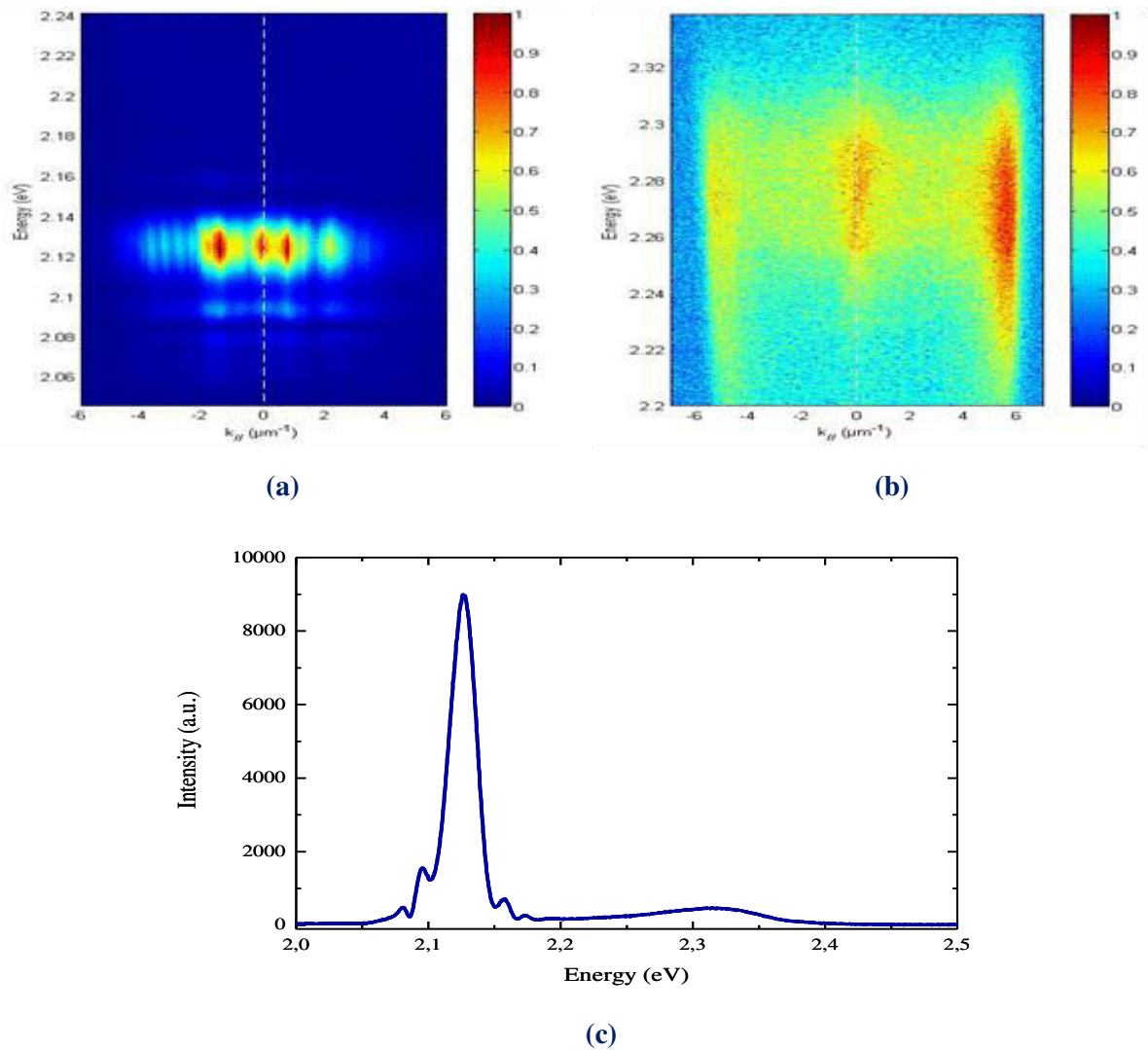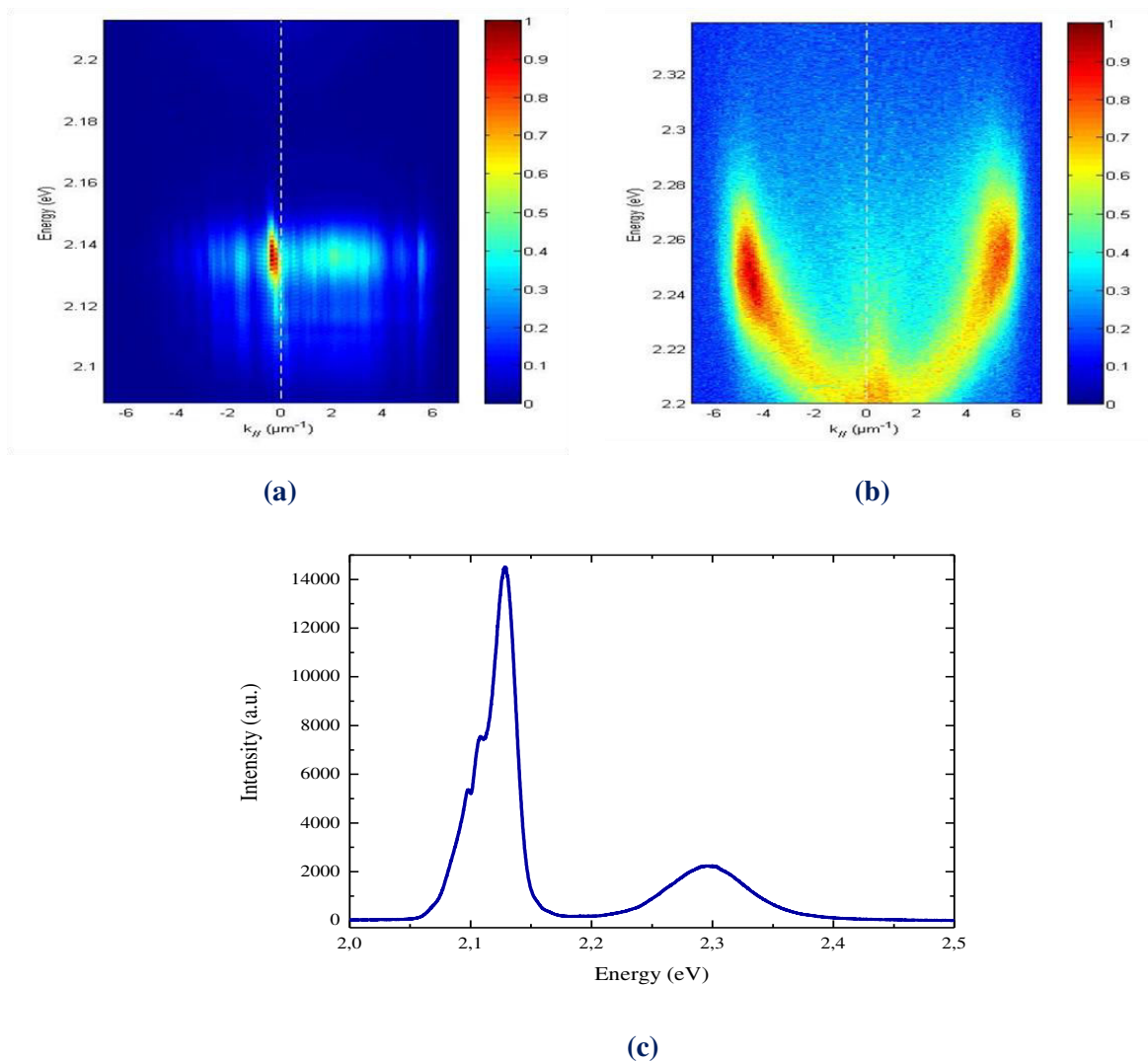

Figure 4.15: Point2: Using 405nm femtosecond laser: (a) Spectrum profile of the cavity at $k_{||}=0$ as function of power, (b) Integrated intensity of both Bragg and cavity mode as function of power.

However using the 440 nm femtosecond laser, µPL spectra performed on point 3 are recorded as a function of power **(Figure 4.16a)**. Note that we were able to go further in power with 440 nm femtosecond laser than with 405nm femtosecond laser. **Figure 4.16 b)** presents the integrated intensity of both Bragg mode and cavity mode as a function of power. We can see that the integrated intensity of the Bragg mode increases linearly with power whereas the integrated intensity of the cavity mode saturates as power increases.

First, we can conclude that the MPB saturation is reached in the femtosecond excitation configuration. This observation may come from the high number of injected carriers that should lead to Auger effects such as the ones observed in the pump/probe experiments (see chapter 3). Indeed, polariton-polariton interactions are mediated by their excitonic part. Therefore, exciton-exciton annihilation that occurs at such high excitation densities will lead to a saturation of the polaritons population. The consequence is the saturation of the MPB emission reported both in **figures 4.15** and **4.16**. Finally, the intense signal at low energy, localized in the k-space, is not well understood. The interference patterns observed in the k-space images suggest coherent effects. The linear dependence on power **(figure 4.16)**, and the fact that no narrowing of the line width is observed, seem to rule out the possibility of polariton lasing as origin of this signal.
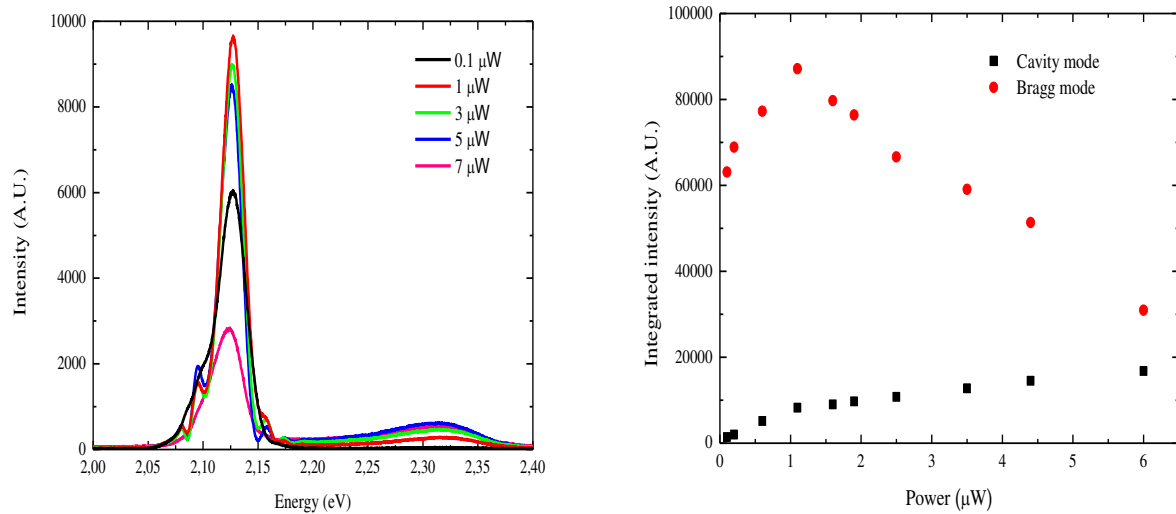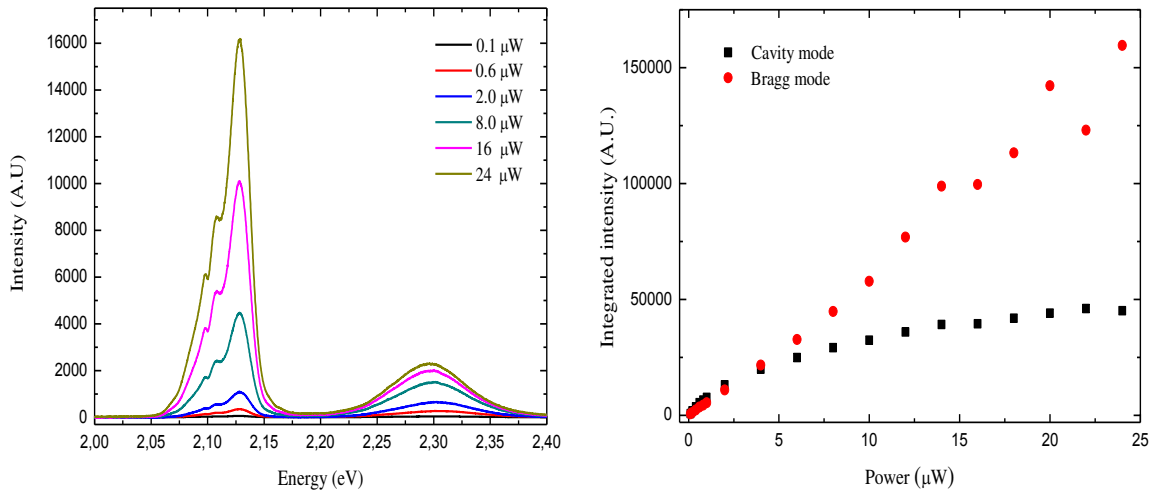
Figure 4.16: Point 3: Using 440 nm femtosecond laser: (a) Spectrum profile of the cavity at $k_{||}$=0 as function of power. (b) Integrated intensity of both Bragg and cavity mode as function of power.

4.3.   0D polariton:

In this section, we demonstrate the quantum confinement of zero-dimensional (0D) perovskite-based polaritons in sphere-like defects. This work was done with H. S. Nguyen at LPN, and detailed in the reference [62]. The sphere-like defects observed for high Q-perovskite microcavity are formed during the evaporation process performed at low temperature for the fabrication of top Bragg mirror. It is believed that a weak surface adhesion combined to the strain accumulated into the dielectric film may induce a local detachment of the film from the surface. It is also likely that the formation of spheres is assisted by a degassing process during the deposition of YF_3 layer, similar to the H_2 sphere like defects formed during PECVD deposition of Si with SiH_4 precursor. These defects have a symmetric half-sphere shape with diameter varying from a few hundred nanometers to a few micrometers measured by SEM (Scanning Electronic Microscopy). Their density is very low, around 10^{-2} μm^{-2} but always packages of several defects separated by less than 20 μm are frequently observed as shown in **Figure 4.17 a)**. **Figure 4.17 b)** depicts a SEM image of the surface of the initial top mirror before the release from its substrate, showing a sphere like defect of 900 nm diameter and of 300 nm height. Once the top mirror released and attached to the perovskite layer, the sphere-like defects are fully conserved on the final samples as shown in **Figure 4.17 c)**. Notice that similar defects have been reported for GaAs based cavities [108]. In this case, they were attributed to point-like defects formed during the molecular beam epitaxy of the top mirror.
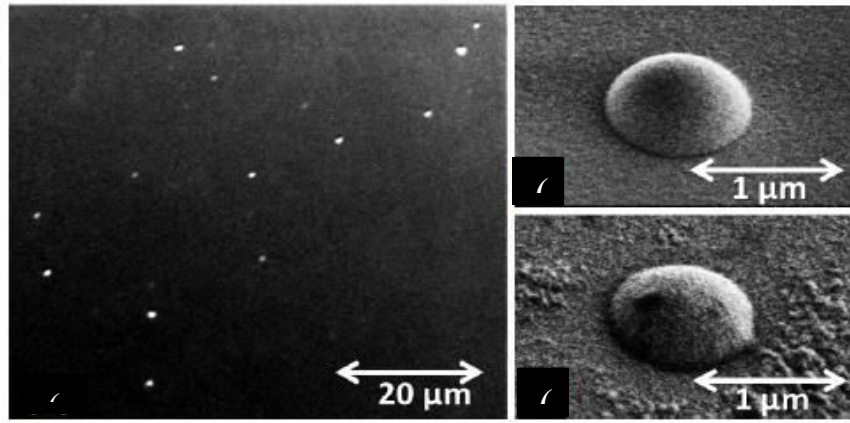
Figure 4.17 (a) Image taken by optical microscope of a package of sphere-like defects on the top Bragg mirror. (b) SEM image of a sphere-like defect of the top Bragg mirror before the release from its substrate. (c) SEM image of a sphere-like defect of the top Bragg mirror on the final sample.

Confocal photoluminescence on single sphere-like defects is performed at room temperature using 405 nm cw diode laser focused onto a 1.5 μm spot diameter by a microscope objective (NA=0.65). Polariton emission is imaged on a CCD camera coupled to a monochromator. **Figure 4.18** presents the PL intensity as function of energy (vertical axis) and position (horizontal axis) of polariton emission within D1 where D1 is a chosen sphere-like defect in our sample. Five discrete polariton modes are distinguished, which correspond to 0D polaritons within the defect due to confinement of photonic component. Interestingly, the confined states have a linewidth 4-8 times smaller than the one of the 2D photonic mode, corresponding to a quality factor $Q \geq 750$. This value is one order of magnitude higher than the Q-factor of the perovskite-based planar cavity measured on the same sample. More informations on these 0D polaritons are detailed in the reference [62].
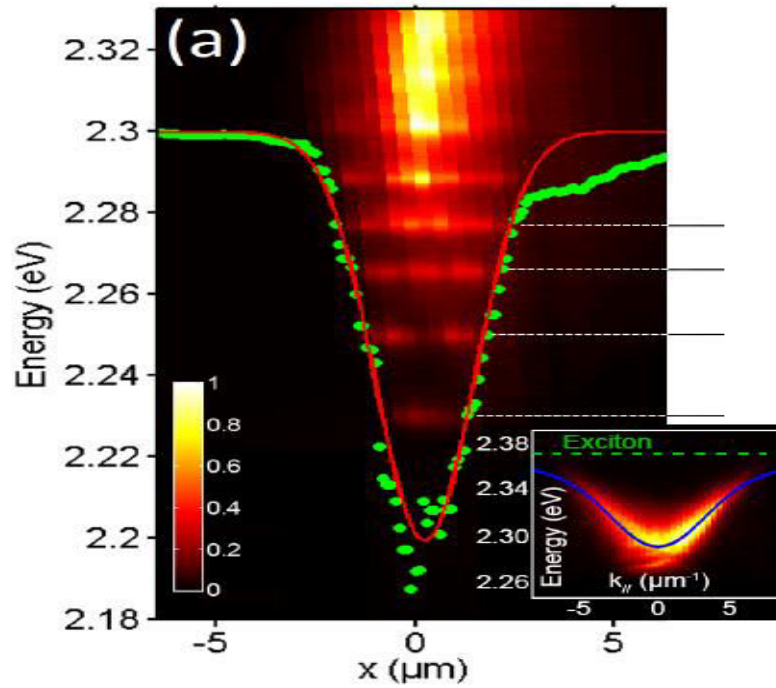
Figure 4.18 (a) Photoluminescence intensity I(x,E) of polariton emission within D1 as a function of position and energy. Green circles: polariton potential of confinement within D1. Red line: Gaussian fit of FWHM amounts to 2.6μm. Inset: Dispersion spectrum of 2D polaritons in the planar region outside D1. Blue line: fitting of dispersion using three level model.

4.4. Photostability of Perovskite

Besides the fabrication technique of top dielectric mirror, the realization of high quality optoelectronic devices based on 2D-layered organic-inorganic perovskites requires optimization of several properties of the hybrid molecules such as the surface roughness and the photostability. Improving the photostability is important in the framework of both long life-time optoelectronic devices and of fundamental studies, where a great reproducibility of the optical results is necessary and where the study of the non-linear effects requires high incident power.
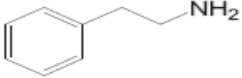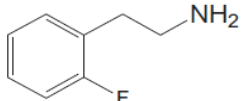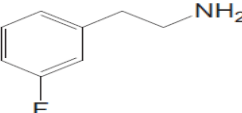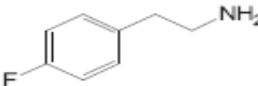
Due to the fact that perovskite layers protected with PMMA present a slightly improved photostability and that fluoroperovskites present improved photostability too, we introduce nanometer-sized fluoroperovskite crystals in a PMMA matrix. This approach has been used in Y. Wei's work [21] and remarkable improvements of thermal and photo-stability were achieved for instance with 4F-$(C_6H_5C_2H_4NH_3)_2PbI_4$ (named 4FPEPI) doped PMMA films. The nanocrystals of perovskites included in PMMA layer still keep stable crystalline and electronic

structures, leading to good optical properties. These advantages make the fluoroperovskite doped PMMA layers very promising for the fabrication of optical devices.

4.4.1. Structure characterization

Table 4.1 shows the chemical structures, the names and the abbreviations of the amines T-$(CH_2)_2NH_2$ used in this study. As previously mentioned, the bis(phenethylammonium) tetraiodoplumbate is noted as PEPI. When fluorine is present, the amine is simply designated by xFPE, where the number x labels the position of the fluorine atom on the phenyl ring: x=4 for para, x=3 for meta and x=2 for ortho. For clarity this has been summarized in **Table 4.1**. The ammonium salts have been prepared by simple way of the considered amines, and the properties of the corresponding perovskites are analyzed in comparison with the generic PEPI compounds containing no fluorine.

Table 4.1: Chemical structure, complete name and abbreviation of amine part of fluorinated perovskites

Chemical structure of amine	Name	Abbreviation
	2-Phenylethanamine	PE
	2-Fluorophenethylamine	2FPE
	3-Fluorophenethylamine	3FPE
	4-Fluorophenethylamine	4FPE

An important difference is observed according to the place of the fluorine substituent. **Figure 4.19** shows the normalized µPL measurement as function of time of PEPI perovskite and different fluorinated perovskites performed by Y.Wei [21]. We can see that the para substitution provides the most resistant character. The structure of the perovskite produced from para-fluorophenylamine is represented in **Figure 4.20**, based on the analogy with the generic

$(C_6H_5(CH_2)_2NH_3)_2PbI_4$ structure and considering that the steric hindrance of a fluorine atom is almost the same than the one of an hydrogen atom.
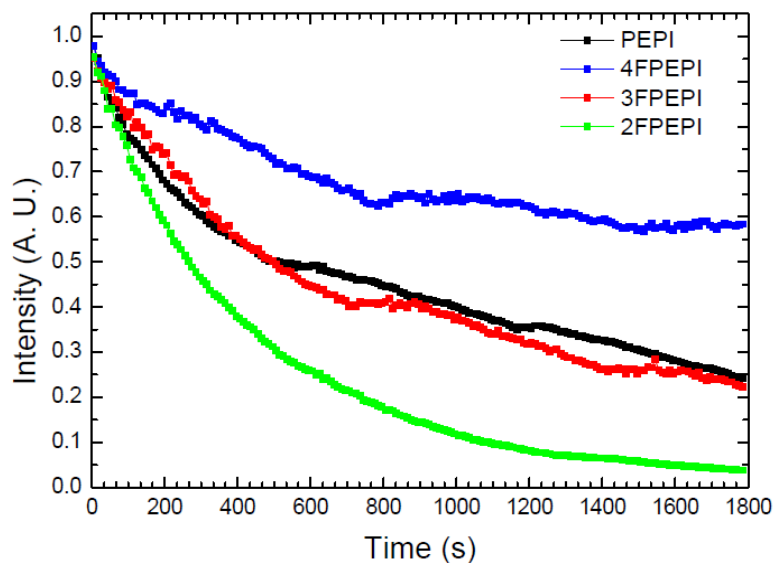
Figure 4.19 Photobleaching of iodide based perovskites layers deposited from 10wt% solutions. The measurement are carried on by Y. Wei, the laser power is 7mW at 325nm.
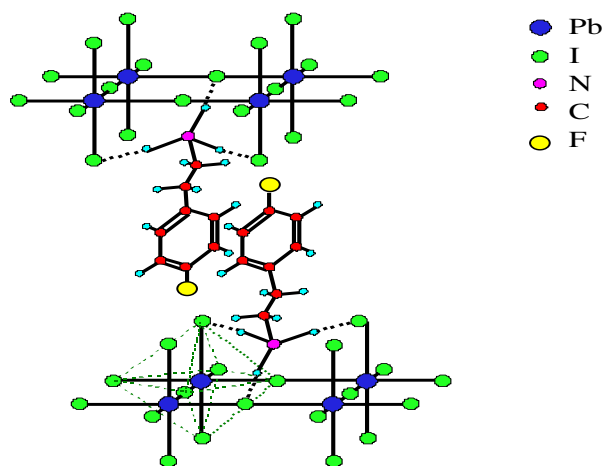
Figure 4.20 Sketch of the structure of the $(4\text{-}FC_6H_4(CH_2)_2NH_3)_2PbI_4$ (4FPEPI) perovskites.

4.4.2. Preparation of 4FPEPI doped PMMA

The 4FPEPI doped PMMA solution is deposited on a quartz substrate by conventional spin-coating method. To prepare the solution, a transparent polymer PMMA and a stoichiometric amount of the ammonium salt and PbI_2 are dissolved into DMF. In the following measurements, we varied the concentration of PMMA in DMF while the weight ratio of

perovskite/PMMA is fixed at 1:5. With these solutions, spin-coating is performed at 2000 rpms, 40 sec. The solution in concentrations 20wt%, 10wt%, and 5wt% respectively give layers of thickness of about 1μm, 375 nm and 162 nm respectively.

After spin-coating, these films need to be subsequently dried in a hot place. This step is especially important for perovskite doped PMMA layers because the PMMA component makes the solution quite viscous and thick, which suppresses the movement of perovskite molecules in solution environment. Therefore the temperature and the annealing time should be appropriately raised to 150°C and for 90min to promote the self-organization process.

4.4.3. Optical characterization

The perovskites based on fluorophenylamine are studied, both from the point of view of the absorbance and PL, but also the photoresistance of the films is estimated. The absorbance of four films of different concentrations is represented in **Figure 4.21**. A clear bathochromic effect of the concentration is noticeable on the spectra: $E_{4FPEPI\ doped\ PMMA\ 20\%}$ -$E_{PEPI10\%}$ = 4.6meV and $E_{4FPEPI\ doped\ PMMA\ 5\%}$ - $E_{PEPI10\%}$ = 6.9 meV. The two peaks of PEPI10% and 4FPEPI doped PMMA 10% are almost at same energy.
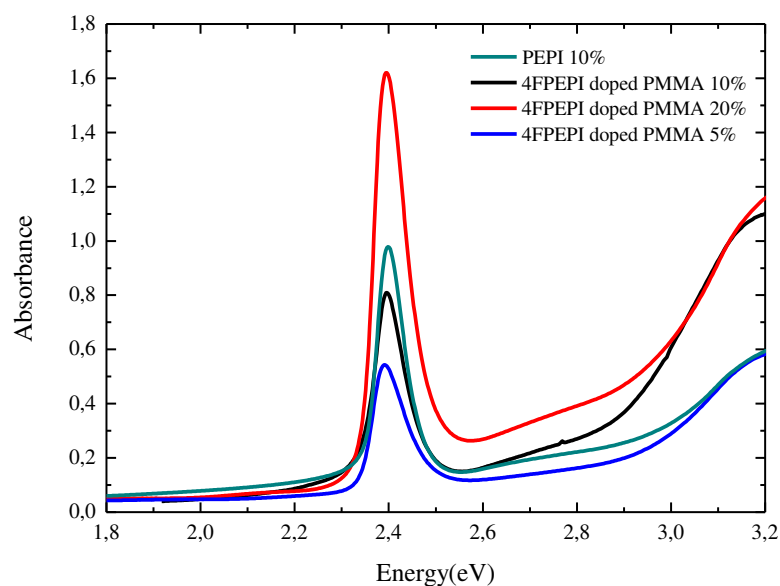
Figure 4.21 Absorbance of iodide based perovskites made from different PMMA solution concentration.

The luminescence of the iodide-based perovskites is represented in **Figure 4.22**. Apart from the correlated bathochromic shift of the emission of 4FPEPI doped PMMA10% (13 meV), it appears that it shines almost as strongly as PEPI, while the emission yield is higher for 4FPEPI doped PMMA 20% and lower for 4FPEPI doped PMMA 5%.

Figure 4.22. Photoluminescnece of iodide based perovskites made from different PMMA solution concentration. The excitation laser is the 405 nm cw diode laser.
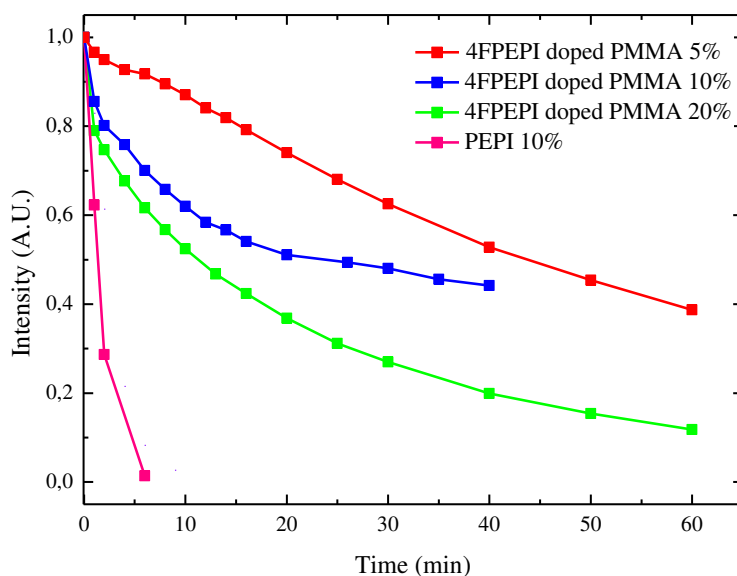
Figure 4.23 Normalized photobleaching rate of iodide based perovskite layers made from different PMMA solution concentrations. The excitation laser is the 405 nm cw diode laser.

To investigate photostability of these layers, photobleaching measurement is carried on using 405 nm cw diode laser focused to a 2μm diameter spot by a microscope objective. To be able to compare the luminescence from the corresponding four layers, we have injected the four layers with the same carriers density. **Figure 4.23** shows the normalized μPL measurement as a function of time of iodide based perovskite layers made from different PMMA solution

concentrations. We can see that the 4FPEPI doped PMMA layer is more stable than the PEPI thin film sample. The 4FPEPI doped PMMA layer degrades much less under illumination than PEPI layer. Being the robust layer with optimized optical properties, the 4FPEPI doped PMMA therefore becomes a good candidate to be introduced into a microcavity. Moreover 4FPEPI doped PMMA 5% seems to be more stable than 4FPEPI doped PMMA 20% and 4FPEPI doped PMMA 10% where the time decays are 90 min, 22 min and 7 min respectively.

The photostability process is a complex process influenced by many factors working together such as oxidation, temperature, spatial arrangements and many others. We thought energy of excitation may also affect the photostability and so µPL measurements as a function of time for the four different perovskites is performed using 473 nm cw diode laser as excitation laser. The hope was that using a higher wavelength of excitation (lower energy) will improve the photostability. Indeed, some photo-assisted oxidation processes are more efficient as the energy of photons is increased. **Figure 4.24** shows that the degradation behavior of perovskite under illumination is the same using an excitation wavelength of 473 nm or 405 nm.

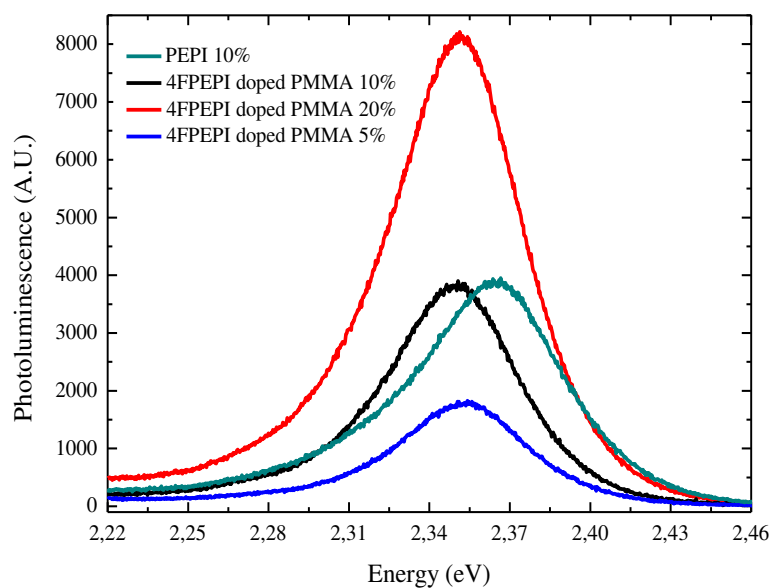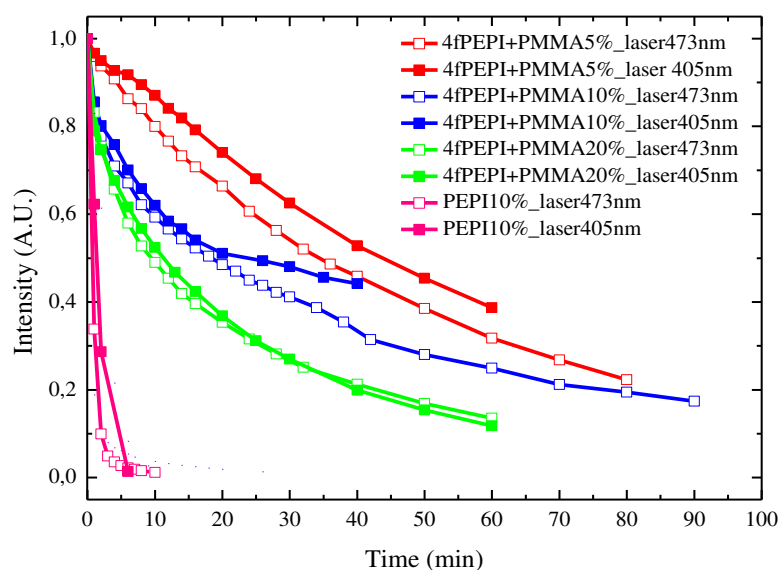**Figure 4.24** Normalized photobleaching rate of iodide based perovskite layers made from different PMMA solution concentrations. The excitation laser is the 405 nm or 473 nm cw diode laser.

Moreover, µPL measurements as a function of excitation power is performed in order to further investigate the photostability of these layers. **Figure 4.25** shows the normalized µPL measurements as a function of power in logarithmic scale. The excitation laser is the 405 nm cw diode laser in **Figure 4.25 a)** and the 473 nm cw diode laser in **Figure 4.25 b)**. Power was increased from 1µW to 1mW for the four layers. We can see in **Figure 4.25 a)** that intensity of

luminescence, excited at 405 nm, increases linearly with power for 4FPEPI doped PMMA 10%, however it increases sublinearly for the others. On the other hand, for excitation at 473 nm, we can see that intensity of luminescence increases sublinearly with power for PEPI, however it increases almost linearly for the others and especially the 4FPEPI doped PMMA 5%.

Comparisons of results displayed in **figures 4.23, 4.24 and 4.25** does not show any improvement in terms of photostability while changing the excitation wavelength from 405 nm to 473 nm. Therefore, future experiments that will be performed on cavities containing this new material will use a 405nm laser diode because its energy lies out of the stop band of dielectric mirror.

(a)   **(b)**
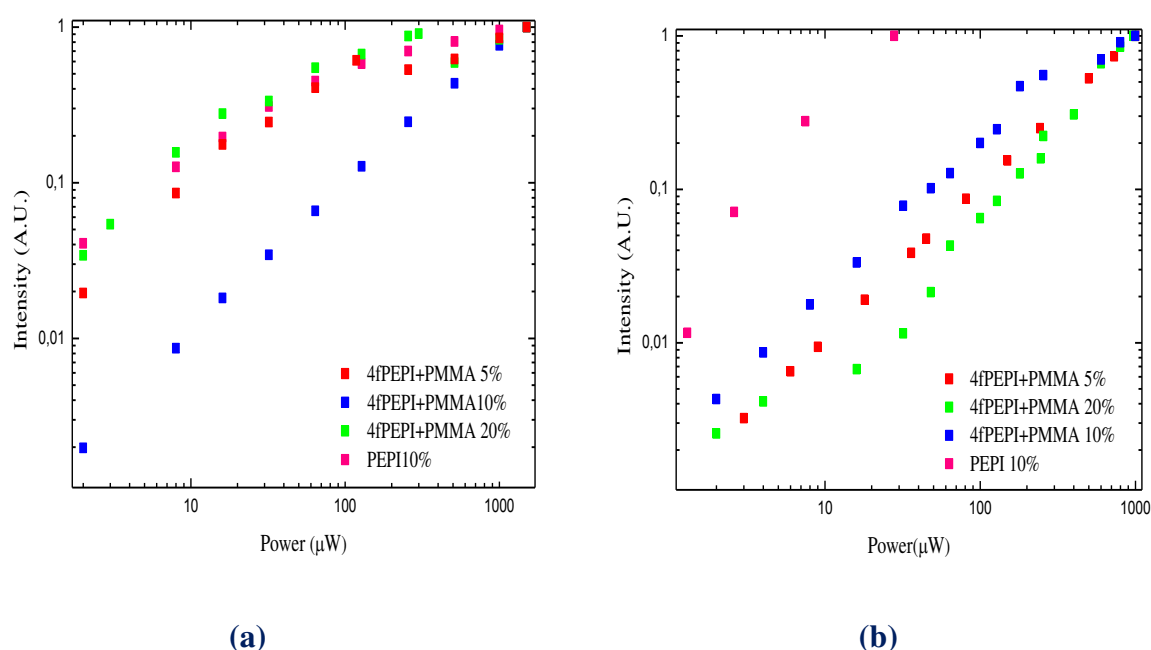
Figure 4.25 μPL measurements as function of power in logarithmic scale. The excitation laser is a) the 405nm cw laser diode and b) the 473nm cw laser diode.

4.5.   Conclusion

In this Chapter, we have presented a new technique for the fabrication of high-Q planar microcavities containing a fragile active material. The technique allows replacing semitransparent metallic top mirror by a highly reflective Bragg mirror without degrading the active material. It is based on the migration in liquid of the top dielectric mirror allowing a significant increase of the cavity mode quality factor. Reflectivity measurements on passive cavities demonstrate that the top-mirror migration approach allows to have higher quality factor in comparison with the monolithic approach. Perovskite-based microcavity operating in the

strong coupling regime fabricated using this approach shows superior performances compared with standard monolithic cavities. Using both angle resolved reflectivity and microphotoluminescence measurements, emission spectra having well-resolved polariton branches are shown without any significant emission from the uncoupled perovskite exciton, contrary to the case of microcavities using metallic top mirror and exhibiting a low quality factor. Moreover, efficient polariton relaxation toward the minimum of the middle polariton branch is obtained.

µPL measurements on PEPI based microcavity using migration technique in liquid has been also performed using different lasers. The 355 nm picosecond laser has shown similar results to the results obtained when using the 405 nm continuous laser. We can see one peak attributed to MPB (cavity mode). However when using the 405 nm and 440 nm femtosecond lasers, two peaks are present attributed to cavity and Bragg modes. Zero-dimensional cavity polaritons have been demonstrated at room temperature, making use of polariton confinement within micron-size sphere-like defects.

It is true that we were able to increase the quality factor of perovskite-based microcavities, however it was not sufficient to see Bose condensation. For that, we need to increase further the quality factor of our system. Another thing we have to do, is to improve the photo-resistance of the active material in order to be able to use stronger laser illumination to reach the threshold for non-linear effects. A new kind of perovskite material has been synthesized: 4FPEPI doped PMMA layers, presenting a high stability under laser illumination. Studying the emission of this material with different concentrations of PMMA as a function of power and time shows that 4FPEPI doped PMMA 5% is the best material. This opens the way to the realization of high quality factor cavities containing 4FPEPI doped PMMA 5% by closing the cavity with a dielectric mirror, and then to the study of non-linear effects using strong laser illumination.

General Conclusion

Organic-inorganic hybrid semiconductors based on metal halide units have attracted attention due to their potential applications in light-emitting optical devices and more recently in photovoltaic devices. They are easily grown from solution and deposited by spin-coating on a substrate. They present a self-organized structure whose crystalline nature can be demonstrated by X-ray diffraction. The structure of the 2D layered perovskites is bidimensional, consisting of an alternation of inorganic layers around 0.5 nm thick and of organic layers around 1 nm thick. The exciton binding energies and oscillator strengths are sufficiently large in these systems making the realization of microcavities in the strong coupling regime with high quality at room temperature possible. As a relatively new material, the perovskites still have many behaviors that are not well understood and a lot of research work is necessary. In this thesis, the main aim of this research work concerns the study of the optical properties of perovskites and their use as active material in microcavities working in the strong coupling regime.

During the three years of my thesis, our research was brought simultaneously on two different main axes. The first was to study the dynamics of excitons in the particular perovskite named as PEPI using pump-probe spectroscopy. The second axe was focused on the study of PEPI-based microcavities with both silver mirror and dielectric mirror as top mirrors. In order to characterize the properties of both perovskite thin films and microcavities containing them, we have used our home made techniques at room temperature: angle –resolved reflectivity, angle-resolved photoluminescence, μPL and pump-probe experimental setup.

We have presented in chapter 3 the dynamics of excitons in PEPI layers at room temperature under both low and high excitation regimes. For low excitation regime, time resolved measurements have been performed using pump-probe spectroscopy for both the pump energy in resonance with that of exciton (2.397 eV) and above the 2D continuum (2.818 eV). The amplitude of the transient bleaching of the exciton line normalized by the number of injected carriers is shown to be identical in both cases. A biexponential decay has been extracted from the measurements with decays of 170 ps and > 1ns attributed as first interpretation to free excitons and localized excitons respectively. To investigate this point, more experiments such as time resolved photoluminescence experiments and experiments in function of temperature will be performed in the coming months.

Moreover, an ultrafast intraband relaxation has been observed. Finally, it has been demonstrated that the renormalization of the exciton wavefunction plays an important role in the understanding of the carrier dynamics in 2D perovskites.

On the other hand we have presented in Chapter 4 the separate growth of the Bragg mirrors and the assembly technique based on the migration in liquid of the top dielectric mirror which allows a significant increase in the cavity mode quality factor. The quality factor could be further improved by simply increasing the number of Bragg pairs. Moreover, emission spectra exhibit well-resolved polariton branches without any significant emission from the uncoupled perovskite exciton contrary to standard perovskite-based microcavities presenting a low quality factor. Efficient polariton relaxation toward the minimum of the middle polariton branch is obtained.

Besides the fabrication technique of top dielectric mirror, a new kind of perovskite material: 4FPEPI doped PMMA layers, presenting a higher stability under laser illumination than PEPI is synthesized. It has been found that 4FPEPI doped PMMA 5% is the most stable material. This opens the way to the realization of high quality factor cavities containing 4FPEPI doped PMMA 5% by closing the cavity with a dielectric mirror, and then to the study of non-linear effects using strong laser illumination.

ANNEX A

Mono and bi-exponential Relaxation Model:

In a mono-exponential relaxation model, the impulse response R (t) of the material is of the form:

$$R(t) = A \exp\left(-\frac{t}{\tau}\right) H(t)$$

Where H(t) is a Heaviside step function, A and τ are the amplitude and the time characteristics respectively. The pump-probe time traces corresponding to mono-exponential relaxation are a result of the convolution product between the impulse Response R(t) and the cross correlation of the pump and probe CC(t).

$$s(t) = (CC * R)(t)$$

If the envelopes of the pump and probe pulses are assumed to be Gaussian, then the cross correlation CC (t) is itself a Gaussian function whose mathematical expression is given by:

$$CC(t) = \sqrt{\frac{2}{\pi}} \frac{1}{\omega} \exp\left(-2\frac{t^2}{\omega^2}\right)$$

The width at half maximum of the Gaussian function is related to ω by the relation $\sqrt{2\ln 2}\,\omega$.

The pump-probe time trace can be written using the mathematical equations of R(t) and C(t) as:

$$s(t) = \sqrt{\frac{2}{\pi}} \frac{A}{\omega} \int_{-\infty}^{+\infty} \exp\left(-\frac{x}{\tau}\right) H(x) \exp\left[-2\frac{(t-x)^2}{\omega^2}\right] dx \qquad H(x)=1 \text{ for } x>0$$

$$s(t) = \sqrt{\frac{2}{\pi}} \frac{A}{\omega} \int_{0}^{+\infty} \exp\left(-\frac{x}{\tau}\right) \exp\left[-2\frac{(t-x)^2}{\omega^2}\right] dx$$

$$s(t) = \sqrt{\frac{2}{\pi}} \frac{A}{\omega} \int_{0}^{+\infty} \exp\left(-\frac{x}{\tau}\right) \exp\left[-\frac{2}{\omega^2}\left(t^2 - 2xt + x^2\right)\right] dx$$

$$s(t) = \sqrt{\frac{2}{\pi}} \frac{A}{\omega} \int_0^{+\infty} \exp\left(-\frac{x}{\tau} - \frac{2t^2}{\omega^2} + \frac{4xt}{\omega^2} - \frac{2x^2}{\omega^2}\right) dx$$

$$s(t) = \sqrt{\frac{2}{\pi}} \frac{A}{\omega} \exp\left(-\frac{2t^2}{\omega^2}\right) \int_0^{+\infty} \exp\left(-\frac{2}{\omega^2}\left(x^2 + x\left(\frac{\omega^2}{2\tau} - 2t\right)\right)\right) dx$$

$$s(t) = \sqrt{\frac{2}{\pi}} \frac{A}{\omega} \exp\left(-\frac{2t^2}{\omega^2}\right) \int_0^{+\infty} \exp\left(-\frac{2}{\omega^2}\left(x^2 + cx\right)\right) dx$$

let : $\left(x^2 + cx\right) = \left(x + \frac{c}{2}\right)^2 - \frac{c^2}{4}$ and $c = \frac{\omega^2}{2\tau} - 2t$

$$s(t) = \sqrt{\frac{2}{\pi}} \frac{A}{\omega} \exp\left(-\frac{2t^2}{\omega^2}\right) \int_0^{+\infty} \exp\left(-\frac{2}{\omega^2}\left(\left(x + \frac{c}{2}\right)^2 - \frac{c^2}{4}\right)\right) dx$$

$$s(t) = \sqrt{\frac{2}{\pi}} \frac{A}{\omega} \exp\left(-\frac{2t^2}{\omega^2}\right) \exp\left(\frac{c^2}{2\omega^2}\right) \int_0^{+\infty} \exp\left(-\frac{2}{\omega^2}\left(x + \frac{c}{2}\right)^2\right) dx$$

Let : $\frac{X^2}{2} = \frac{2}{\omega^2}\left(x + \frac{c}{2}\right)^2$

$$s(t) = \sqrt{\frac{2}{\pi}} \frac{A}{\omega} \exp\left(-\frac{2t^2}{\omega^2}\right) \exp\left(\frac{c^2}{2\omega^2}\right) \int_{\frac{\omega}{2\tau} - \frac{2t}{\omega}}^{+\infty} \frac{\omega}{2} \exp\left(-\frac{X^2}{2}\right) dX$$

$$s(t) = \sqrt{\frac{2}{\pi}} \frac{A}{\omega} \frac{\omega}{2} \exp\left(-\frac{2t^2}{\omega^2}\right) \exp\left(\frac{c^2}{2\omega^2}\right) \int_{\frac{\omega}{2\tau} - \frac{2t}{\omega}}^{+\infty} \exp\left(-\frac{X^2}{2}\right) dX$$

$$s(t) = K1 \int_{\frac{\omega}{2\tau} - \frac{2t}{\omega}}^{+\infty} \exp\left(-\frac{X^2}{2}\right) dX$$

With $K1 = \sqrt{\frac{2}{\pi}} \frac{A}{2} \exp\left(-\frac{2t^2}{\omega^2}\right) \exp\left(\frac{c^2}{2\omega^2}\right) = \sqrt{\frac{2}{\pi}} \frac{A}{2} \exp\left(-\frac{2t^2}{\omega^2}\right) \exp\left(\frac{1}{2\omega^2}\left(\frac{\omega^2}{2\tau} - 2t\right)^2\right)$

$K1 = \sqrt{\frac{2}{\pi}} \frac{A}{2} \exp\left(\frac{\omega^2}{8\tau^2}\right) \exp\left(-\frac{t}{\tau}\right) = K2 \exp\left(-\frac{t}{\tau}\right)$ where $K2 = \sqrt{\frac{2}{\pi}} \frac{A}{2} \exp\left(\frac{\omega^2}{8\tau^2}\right)$

$$s(t) = K2 \exp\left(-\frac{t}{\tau}\right) \int_{\frac{\omega}{2\tau} - \frac{2t}{\omega}}^{+\infty} \exp\left(-\frac{X^2}{2}\right) dX$$

Finally taking advantage of the error function erf(x) defined as:

$$\text{erf}(x) = 2 \times \frac{1}{\sqrt{2\pi}} \int_{-\infty}^{x\sqrt{2}} \exp\left(-\frac{t^2}{2}\right) dt - 1$$

We obtain:

$$s(t) = \frac{\sqrt{2\pi}}{2} K1\left[\text{erf}\left(\frac{\sqrt{2}t}{\omega} - \frac{\omega}{2\sqrt{2}\tau}\right) + 1\right] = K \exp\left(-\frac{t}{\tau}\right)\left[\text{erf}\left(\frac{\sqrt{2}t}{\omega} - \frac{\omega}{2\sqrt{2}\tau}\right) + 1\right]$$

With $K = \dfrac{A}{2}\exp\left(\dfrac{\omega^2}{8\tau^2}\right)$

This result can be generalized, and the pump-probe traces corresponding to biexponential decay model can then be written as:

$$s(t) = \frac{A_{short}}{2}\exp\left(\frac{\omega^2}{8\tau_{short}^2}\right)\exp\left(\frac{-t}{\tau_{short}}\right)\left(1 - \text{erf}\left(\frac{\omega}{2\sqrt{2}\tau_{short}} - \frac{\sqrt{2}t}{\omega}\right)\right) +$$

$$\frac{A_{long}}{2}\exp\left(\frac{\omega^2}{8\tau_{long}^2}\right)\exp\left(\frac{-t}{\tau_{long}}\right)\left(1 - \text{erf}\left(\frac{\omega}{2\sqrt{2}\tau_{long}} - \frac{\sqrt{2}t}{\omega}\right)\right)$$

A_{short} and τ_{short} (A_{long} and τ_{long} respectively) corresponds to the amplitude and the time characteristic of rapid relaxation (respectively slow relaxation) phenomenon.

References

1. Weisbuch, C., H. Benisty, and R. Houdré, *Overview of fundamentals and applications of electrons, excitons and photons in confined structures.* Journal of Luminescence, 2000. **85**(4): p. 271-293.
2. Moskalenko, S.A. and F. Tverd, Tela 4, 1962: p. 276.
3. Blatt, J.M., K.W. Boer, and W. Brandt, *Bose-Einstein condensation of excitons.* Physical Review, 1962. **126**(5): p. 1691.
4. Lozovik, Y.E. and I.V. Ovchinnikov, *Many-photon coherence of Bose-condensed excitons: Luminescence and related nonlinear optical phenomena.* Physical Review B, 2002. **66**(7): p. 075124.
5. Lagoudakis, P.G., et al., *Electron-polariton scattering in semiconductor microcavities.* Physical review letters, 2003. **90**(20): p. 206401.
6. Reithmaier, J.P., et al., *Strong coupling in a single quantum dot-semiconductor microcavity system.* Nature, 2004. **432**(7014): p. 197-200.
7. Christmann, G., et al., *Room temperature polariton lasing in a GaN/AlGaN multiple quantum well microcavity.* Applied Physics Letters, 2008. **93**(5): p. 051102.
8. Christopoulos, S., et al., *Room-temperature polariton lasing in semiconductor microcavities.* Physical review letters, 2007. **98**(12): p. 126405.
9. Li, F., et al., *From Excitonic to Photonic Polariton Condensate in a ZnO-Based Microcavity.* Physical review letters. **110**(19): p. 196406.
10. Lidzey, D.G., et al., *Strong exciton-photon coupling in an organic semiconductor microcavity.* Nature, 1998. **395**(6697): p. 53-55.
11. Plumhof, J.D., et al., *Room-temperature Bose-Einstein condensation of cavity exciton-polaritons in a polymer.* Nature materials, 2013.
12. Audebert, P., et al., *Synthesis of New Perovskite Luminescent Nanoparticles in the Visible Range.* Chemistry of Materials, 2009. **21**(2): p. 210-214.
13. Lanty, G., *Réalisation et caractérisation optique de microcavités en régime de couplage fort mettant à profit la structure en multi-puits quantiques auto-organisés des pérovskites en couches minces.* Thèse de Doctorat 2011, Ecole normale supérieure de Cachan-ENS Cachan.
14. Lanty, G., et al., *Strong exciton-photon coupling at room temperature in microcavities containing two-dimensional layered perovskite compounds.* New Journal of Physics, 2008. **10**(6): p. 065007.
15. Lanty, G., et al., *Strong-coupling regime at room temperature in one-dimensional microcavities containing ultraviolet-emitting perovskites.* Superlattices and Microstructures, 2010. **47**(1): p. 10-15.
16. Lanty, G., et al., *Hybrid cavity polaritons in a ZnO-perovskite microcavity.* Physical Review B, 2011. **84**(19): p. 195449.
17. Lanty, G.t., et al., *UV polaritonic emission from a perovskite-based microcavity.* Applied Physics Letters, 2008. **93**(8): p. 081101.
18. Zhang, S., et al., *Preparations and characterizations of luminescent two dimensional organic-inorganic perovskite semiconductors.* Materials, 2010. **3**(5): p. 3385-3406.
19. Zhang, S., et al., *Synthesis and optical properties of novel organic-inorganic hybrid UV (R-NH$_3$)$_2$PbCl$_4$ semiconductors.* Journal of Materials Chemistry, 2011. **21**(2): p. 466-474.

20. Bréhier, A., *Puits quantiques hybrides organique-inorganique de pérovskites pour le couplage fort à température ambiante.* Thèse de doctorat 2007, École Normale Supérieure de Cachan.

21. Wei, Y., *Synthesis and optical properties of self-assembled 2D layered organic-inorganic perovskites for optoelectronics.* Thèse de Doctorat 2012, Ecole Normale Supérieure de Cachan.

22. Wei, Y., et al., *Strong exciton-photon coupling in microcavities containing new fluorophenethylamine based perovskite compounds.* Optics express, 2012. **20**(9): p. 10399-10405.

23. Prakash, G.V., et al., *Structural and optical studies of local disorder sensitivity in natural organic-inorganic self-assembled semiconductors.* Journal of Physics D: Applied Physics, 2009. **42**(18): p. 185405.

24. Gauthron, K., et al., *Optical spectroscopy of two-dimensional layered ($C_6H_5C_2H_4$-NH_3)$_2PbI_4$ perovskite.* Optics Express, 2010. **18**(6): p. 5912-5919.

25. Kagan, C.R., D.B. Mitzi, and C.D. Dimitrakopoulos, *Organic-inorganic hybrid materials as semiconducting channels in thin-film field-effect transistors.* Science, 1999. **286**(5441): p. 945-947.

26. Kojima, A., et al., *Organometal halide perovskites as visible-light sensitizers for photovoltaic cells.* Journal of the American Chemical Society, 2009. **131**(17): p. 6050-6051.

27. Lee, M.M., et al., *Efficient hybrid solar cells based on meso-superstructured organometal halide perovskites.* Science, 2012. **338**(6107): p. 643-647.

28. Burschka, J., et al., *Sequential deposition as a route to high-performance perovskite-sensitized solar cells.* Nature. **499**(7458): p. 316-319.

29. Mitzi, D.B., *Synthesis, Structure, and Properties of Organic-Inorganic Perovskites and Related Materials.* Progress in Inorganic Chemistry, Volume 48, 2007: p. 1-121.

30. Hattori, T., et al., *Highly efficient electroluminescence from a heterostructure device combined with emissive layered-perovskite and an electron-transporting organic compound.* Chemical physics letters, 1996. **254**(1): p. 103-108.

31. Mitzi, D.B., M.T. Prikas, and K. Chondroudis, *Thin film deposition of organic-inorganic hybrid materials using a single source thermal ablation technique.* Chemistry of materials, 1999. **11**(3): p. 542-544.

32. Brehier, A., et al., *Strong exciton-photon coupling in a microcavity containing layered perovskite semiconductors.* Applied physics letters, 2006. **89**(17): p. 171110-171110-3.

33. Bastard, G., *Wave Mechanics Applied to Semiconductor Heterostructures.* 1991: Wiley-Interscience ISBN 978-0-470-21708-5.

34. Even, J., et al., *Electronic model for self-assembled hybrid organic/perovskite semiconductors: Reverse band edge electronic states ordering and spin-orbit coupling.* Physical Review B, 2012. **86**(20): p. 205301.

35. Pedesseau, L., et al., *Electronic properties of 2D and 3D hybrid organic/inorganic perovskites for optoelectronic and photovoltaic applications.* Optical and Quantum Electronics: p. 1-8.

36. Lee, J., E.S. Koteles, and M.O. Vassell, *Luminescence linewidths of excitons in GaAs quantum wells below 150 K.* Physical Review B, 1986. **33**(8): p. 5512.

37. Kitazawa, N., *Optical absorption and photoluminescence properties of Pb (I, Br)-based two-dimensional layered perovskite.* Japanese journal of applied physics, 1997. **36**(4R): p. 2272.

38. Parashkov, R., et al., *Preparation and characterization of perovskite type semiconducting thin films*, in *Progress in Advanced Materials Research*, N.H. Voler, Editor. 2008, Nova Science Publishers.

39.   Kitazawa, N., *Excitons in two-dimensional layered perovskite compounds:(C₆H₅C₂H₄NH₃)₂Pb(Br, I)₄ and (C₆H₅C₂H₄NH₃)₂Pb(Cl, Br)₄.* Materials science & engineering. B, Solid-state materials for advanced technology, 1997. **49**(3): p. 233-238.

40.   Mitzi, D.B., *Synthesis, crystal structure, and optical and thermal properties of (C₄H₉NH₃)₂MI₄ (M= Ge, Sn, Pb).* Chemistry of materials, 1996. **8**(3): p. 791-800.

41.   Ishihara, T., *Optical properties of PbI-based perovskite structures.* Journal of luminescence, 1994. **60**: p. 269-274.

42.   Lin, C.-Y., et al., *Photoactive p-type PbS as a counter electrode for quantum dot-sensitized solar cells.* Journal of Materials Chemistry A, 2013. **1**(4): p. 1155-1162.

43.   Yang, Y., et al., *Composite Counter Electrode Based on Nanoparticulate PbS and Carbon Black: Towards Quantum Dot-Sensitized Solar Cells with Both High Efficiency and Stability.* ACS applied materials & interfaces, 2012. **4**(11): p. 6162-6168.

44.   Wang, J., et al., *Core/shell colloidal quantum dot exciplex States for the development of highly efficient quantum-dot-sensitized solar cells.* Journal of the American Chemical Society, 2013. **135**(42): p. 15913-15922.

45.   Ip, A.H., et al., *Hybrid passivated colloidal quantum dot solids.* Nature nanotechnology, 2012. **7**(9): p. 577-582.

46.   Lee, H., et al., *PbS and CdS Quantum Dot-Sensitized Solid-State Solar Cells:"Old Concepts, New Results".* Advanced Functional Materials, 2009. **19**(17): p. 2735-2742.

47.   Im, J.-H., et al., *6.5% efficient perovskite quantum-dot-sensitized solar cell.* Nanoscale, 2011. **3**(10): p. 4088-4093.

48.   Kim, H.-S., et al., *Lead iodide perovskite sensitized all-solid-state submicron thin film mesoscopic solar cell with efficiency exceeding 9%.* Scientific reports. **2**.

49.   Burschka, J., et al., *Sequential deposition as a route to high-performance perovskite-sensitized solar cells.* Nature, 2013. **499**(7458): p. 316-319.

50.   Lidzey, D.G., et al., *Photon-mediated hybridization of Frenkel excitons in organic semiconductor microcavities.* Science, 2000. **288**(5471): p. 1620-1623.

51.   C.Cohen-Tannoudji, B.DIU, and F.LALOE, *Quantum Mechanics II*, ed. HERMANN. 1973. 384–412.

52.   Weisbuch, C., et al., *Observation of the coupled exciton-photon mode splitting in a semiconductor quantum microcavity.* Physical Review Letters, 1992. **69**(23): p. 3314.

53.   Kelkar, P., et al., *Excitons in a II-VI semiconductor microcavity in the strong-coupling regime.* Physical Review B, 1995. **52**(8): p. R5491.

54.   Semond, F., et al., *Strong light-matter coupling at room temperature in simple geometry GaN microcavities grown on silicon.* Applied Physics Letters, 2005. **87**(2): p. 021102.

55.   Lidzey, D.G., et al., *Room temperature polariton emission from strongly coupled organic semiconductor microcavities.* Physical review letters, 1999. **82**(16): p. 3316.

56.   Takada, N., T. Kamata, and D.D.C. Bradley, *Polariton emission from polysilane-based organic microcavities.* Applied physics letters, 2003. **82**(12): p. 1812-1814.

57.   Kéna-Cohen, S., M. Davanço, and S.R. Forrest, *Strong exciton-photon coupling in an organic single crystal microcavity.* Physical review letters, 2008. **101**(11): p. 116401.

58.   Kéna-Cohen, S. and S.R. Forrest, *Room-temperature polariton lasing in an organic single-crystal microcavity.* Nature Photonics, 2010. **4**(6): p. 371-375.

59.   Mitzi, D.B., *Progress in inorganic chemistry.* In: Karlin KD ed. 1999: New York: John Wiley.

60.   Ishihara, T., *Optical properties of low dimensional materials.* In: Ogawa T, Kanemitsu Y, ed. Vol. 2. Singapore: World Scientific. 1998.

61.   Houdré, R., et al., *Room-temperature cavity polaritons in a semiconductor microcavity.* Physical Review B, 1994. **49**(23): p. 16761.

62.   Nguyen, H.S., et al., *Quantum confinement of zero-dimensional hybrid organic-inorganic polaritons at room temperature.* Applied Physics Letters, 2014. **104**(8): p. 081103.

63.   Loffler, A., et al., *Semiconductor quantum dot microcavity pillars with high-quality factors and enlarged dot dimensions.* Applied Physics Letters, 2005. **86**(11): p. 111105-111105-3.

64.   Shank, C.V., *Measurement of ultrafast phenomena in the femtosecond time domain.* Science, 1983. **219**(4588): p. 1027-1031.

65.   Shank, C.V., et al., *Dynamics of photoexcited GaAs band-edge absorption with subpicosecond resolution.* Physical Review Letters, 1979. **42**: p. 112-115.

66.   Lorenc, M., et al., *Artifacts in femtosecond transient absorption spectroscopy.* Applied Physics B, 2002. **74**(1): p. 19-27.

67.   Kittel, C., *Solid state physics.* chapter 11. 1998: Dunod (Paris). 292–295.

68.   Kovalenko, S.A., et al., *Femtosecond spectroscopy of condensed phases with chirped supercontinuum probing.* Physical review A, 1999. **59**(3): p. 2369.

69.   Alfano, R.R., *The supercontinuum laser source.* Springer, 1989.

70.   Agrawal, G.P., P.L. Baldeck, and R.R. Alfano, *Modulation instability induced by cross-phase modulation in optical fibers.* Physical Review A, 1989. **39**(7): p. 3406.

71.   Ekvall, K., et al., *Cross phase modulation artifact in liquid phase transient absorption spectroscopy.* Journal of applied physics, 2000. **87**(5): p. 2340-2352.

72.   Xing, G., et al., *Long-range balanced electron-and hole-transport lengths in organic-inorganic $CH_3NH_3PbI_3$.* Science, 2013. **342**(6156): p. 344-347.

73.   Fujita, T., et al., *Ultrafast photoluminescence from $(C_6H_5C_2H_4NH_3)_2PbI_4$.* Journal of Luminescence, 2000. **87**: p. 847-849.

74.   Ema, K., et al., *Huge exchange energy and fine structure of excitons in an organic-inorganic quantum well material.* Physical Review B, 2006. **73**(24): p. 241310.

75.   Kitazawa, N., M. Aono, and Y. Watanabe, *Excitons in organic–inorganic hybrid compounds (C n H 2n+ 1 NH 3) 2 PbBr 4 (n= 4, 5, 7 and 12).* Thin Solid Films, 2010. **518**(12): p. 3199-3203.

76.   Shimizu, M., et al., *Coulomb correction to the dressed exciton in an inorganic-organic layered semiconductor: Detuning dependence of the Stark shift.* Physical Review B, 2004. **69**(15): p. 155201.

77.   Shimizu, M., J.-I. Fujisawa, and J. Ishi-Hayase, *Influence of dielectric confinement on excitonic nonlinearity in inorganic-organic layered semiconductors.* Physical Review B, 2005. **71**(20): p. 205306.

78.   Ishihara, T., et al., *Dielectric confinement effect for exciton and biexciton states in PbI_4 based two-dimensional semiconductor structures.* Surface science, 1992. **267**(1): p. 323-326.

79.   Tanaka, K., et al., *Image charge effect on two-dimensional excitons in an inorganic-organic quantum-well crystal.* Physical Review B, 2005. **71**(4): p. 045312.

80.   Hong, X., T. Ishihara, and A.V. Nurmikko, *Dielectric confinement effect on excitons in PbI_4-based layered semiconductors.* Physical Review B, 1992. **45**(12): p. 6961.

81.   Shimizu, M. and T. Ishihara, *Subpicosecond pump-probe spectroscopy on excitons in an inorganic-organic layered nanostructure,$(C_6H_5C_2H_4NH_3)_2PbI_4$.* RIKEN REVIEW, 2001: p. 40-43.

82.   Kondo, T., et al., *Biexciton lasing in the layered perovskite-type material $(C_6H_{13}NH_3)_2PbI_4$.* Solid state communications, 1998. **105**(4): p. 253-255.

83.   Kondo, T., et al., *Resonant third-order optical nonlinearity in the layered perovskite-type material $(C_6H_{13}NH_3)_2PbI_4$.* Solid state communications, 1998. **105**(8): p. 503-506.

84. Xu, C.-q., et al., *Optical third-harmonic generation in layered perovskite-type material (C$_{10}$H$_{21}$NH$_3$)$_2$PbI$_4$.* Solid state communications, 1991. **79**(3): p. 245-248.

85. Ishi, J., et al., *Influence of exciton-exciton interactions on frequency-mixing signals in a stable exciton-biexciton system.* Physical Review B, 2001. **63**(7): p. 073303.

86. Shimizu, M., *Exciton-excitonic molecule Rabi splitting in an inorganic-organic layered semiconductor: Inapplicability of the giant oscillator strength model.* Physical Review B, 2005. **71**(3): p. 033316.

87. Chen, X., B. Henderson, and K.P. O'Donnell, *Luminescence decay in disordered low-dimensional semiconductors.* Applied physics letters, 1992. **60**(21): p. 2672-2674.

88. Huang, J.S., et al., *Localized exciton dynamics in AlInGaN alloy.* Solid state communications, 2003. **126**(8): p. 473-477.

89. Kakalios, J., R.A. Street, and W.B. Jackson, *Stretched-exponential relaxation arising from dispersive diffusion of hydrogen in amorphous silicon.* Physical review letters, 1987. **59**(9): p. 1037.

90. Liu, M., M.B. Johnston, and H.J. Snaith, *Efficient planar heterojunction perovskite solar cells by vapour deposition.* Nature. **501**(7467): p. 395-398.

91. Cronenberger, S., et al., *Relaxation of electron-hole pairs by coherent emission of LO-phonons in the quantum kinetic regime measured in CdZnTe quantum wells.* Physical Review B, 2008. **77**(19): p. 195311.

92. Gilliot, P., et al. *LO-phonon cascade emission in CdZnTe quantum wells: coherent control and quantum kinetics.* in *Journal of Physics: Conference Series.* 2007: IOP Publishing.

93. Klimov, V.I., et al., *Optical gain and stimulated emission in nanocrystal quantum dots.* Science, 2000. **290**(5490): p. 314-317.

94. Kambhampati, P., *Hot exciton relaxation dynamics in semiconductor quantum dots: radiationless transitions on the nanoscale.* The Journal of Physical Chemistry C. **115**(45): p. 22089-22109.

95. Jailaubekov, A.E., et al., *Hot charge-transfer excitons set the time limit for charge separation at donor/acceptor interfaces in organic photovoltaics.* Nature materials. **12**(1): p. 66-73.

96. Grancini, G., et al., *Hot exciton dissociation in polymer solar cells.* Nature materials. **12**(1): p. 29-33.

97. Silva, C., *Organic photovoltaics: Some like it hot.* Nature materials. **12**(1): p. 5-6.

98. Litvinenko, K.L., et al., *Dynamics of excitonic states in GaAs/AlGaAs quantum wells.* Journal of Experimental and Theoretical Physics Letters, 1997. **66**(3): p. 144-150.

99. Schmitt-Rink, S., D.S. Chemla, and D.A.B. Miller, *Theory of transient excitonic optical nonlinearities in semiconductor quantum-well structures.* Physical Review B, 1985. **32**(10): p. 6601.

100. Miller, D.A.B., et al., *Large room-temperature optical nonlinearity in GaAs/Ga$_{1-x}$Al$_x$As multiple quantum well structures.* Applied Physics Letters, 1982. **41**(8): p. 679-681.

101. Knox, W.H., et al., *Femtosecond dynamics of resonantly excited excitons in room-temperature GaAs quantum wells.* Physical review letters, 1985. **54**(12): p. 1306.

102. Nozieres, P. and C. Comte, *Exciton Bose condensation: the ground state of an electron-hole gas-II. Spin states, screening and band structure effects.* Journal de Physique, 1982. **43**(7): p. 1083-1098.

103. Ruckenstein, A.E., S. Schmitt-Rink, and R.C. Miller, *Infrared and polarization anomalies in the optical spectra of modulation-doped semiconductor quantum-well structures.* Physical review letters, 1986. **56**(5): p. 504.

104.   Spann, B.T. and X. Xu, *Ultrafast Spectroscopy of CdSe Nanocrystals: Morphological and Environmental Effects on Nonradiative and Nonadiabatic Relaxation.* The Journal of Physical Chemistry C. **118**(5): p. 2844-2850.

105.   Kunneman, L.T., et al., *Bimolecular Auger Recombination of Electron-Hole Pairs in Two-Dimensional CdSe and CdSe/CdZnS Core/Shell Nanoplatelets.* The Journal of Physical Chemistry Letters. **4**(21): p. 3574.

106.   Faure, S., *Interaction lumière-matière dans les microcavités massives à base de ZnO: du couplage fort à température ambiante vers le laser à polariton.* Thèse de Doctorat 2009, Université Montpellier II-Sciences et Techniques du Languedoc.

107.   Han, Z., et al., *Top-Mirror Migration for the Fabrication of High-Q Planar Microcavities Containing Fragile Active Materials.* Applied Physics Express, 2013. **6**(10): p. 106701.

108.   Zajac, J.M., et al., *Polariton states bound to defects in GaAs/AlAs planar microcavities.* Physical Review B, 2012. **85**(16): p. 165309

109.   J. Even, L. Pedresseau ans C. Katan, *Analysis of Multivalley and Multibandgap Absorption and Enhancement of Free Carriers Related to Exciton Screening in Hybrid Perovskites*, J. Phys. Chem C 118, pp 11566 (2014).

110.   T. Jacqmin, I. Carusotto, I. Sagnes, M. Abbarchi, D. Solnyshkov, G. Malpuech, E. Galopin, A. Lemaître, J. Bloch, A. Amo, *Direct Observation of Dirac Cones and a Flatband in a Honeycomb Lattice for Polaritons*, Phys. Rev. Lett. 112, 116402 (2014)